Optical Skyrmions and Polarizations of Highly Focused Structured Light

Zhujun Ye

A thesis submitted in fulfilment of the requirements for the degree of
Doctor of Philosophy

School of Physics and Astronomy
College of Science and Engineering
University of Glasgow
Jan 2025

Abstract

Structured light refers to the controlled tailoring of light fields, encompassing customized attributes such as intensity, phase, and polarization. The study of structured light is motivated by its broad applications, including optical tweezers for trapping and manipulating microscopic particles, multiplexed optical communication, advanced imaging techniques like super-resolution microscopy, and quantum information processing. Additionally, structured light offers unique properties such as orbital angular momentum (OAM), which allows information encoding in the twisted phase of light, and spatially varying polarization patterns, which facilitate precise control over light-matter interactions.

In this thesis, we investigate various topics related to structured light, including the Faraday effect in strongly focused fields, optical skyrmions, and a two-sphere method for analyzing 3D polarization fields generated by strong focusing. We demonstrate that, for structured light, magneto-optical interactions, specifically the well-known Faraday effect, exhibit a more intricate pattern, which we term the *secondary Faraday effect.* This effect, arising from the same mechanism as the linear Faraday effect, becomes significant in a strong focusing system, where it reaches a magnitude comparable to the linear effect.

We also introduce *skyrmionic beams*, a class of structured light that has attracted significant research attention. Building on existing methods for calculating skyrmion numbers, we propose a novel approach that explicitly links these numbers to their topological definitions. Furthermore, we identify that skyrmions and bimerons—configurations involving two distinct regions of opposite topological charge—are topologically equivalent by generalizing the definition of their parameters. Emphasis is placed on the geometrical interpretations, which lead to an extended definition of singularities.

Throughout the thesis, we are particularly interested in highly focused systems, where additional spatial dimensions play a crucial role compared to paraxial optics. To investigate this, we introduce a two-sphere method to comprehensively describe general 3D polarization fields and apply it to a focused, hence non-paraxial skyrmion beam, as an example.

Contents

Acknowledgements

I would like to first thank my supervisors Prof. Jörg B Götte and Prof. Sonja Franke-Arnold, for their long support throughout my entire PhD period. Jörg is a very patient supervisor who tolerated a lot of naive questions I raised, helped me massively with my programming. Sonja has always been strict but considerate, giving countless useful advises on all aspects of academia and life. They are both kind and helpful, and fully supported me throughout the COVID-19 pandemic time with massive understanding. They are like my academic parents who watched me grow up and learn slowly throughout my four and a half years in Glasgow. I can never express enough gratitude to them.

I would also want to express my gratitude to Prof. Stephen Barnett, who has been very encouraging, inspiring and helpful. Steve is very wise and knowledgeable, and is always willing to have discussions on all kinds of questions with genius advice. I would also like to thank Dr. Claire M Cisowski and Dr. Amy McWilliam, for their discussions with me on the experimental side of skyrmions, which inspired me to develop the bases change theory of skyrmions. And Sphinx Svensson, for all the interesting discussions we had on strong focusing and other than that. They are also very good friends in my life, I will always remember all the interesting conversations we had.

I want to thank all the group members in the Quantum Theory group, Tom, Ben and Romek who were my friendly office members are always willing to have interesting discussions on everything. Maddie and Hector are always humorous and clever, I will be missing all the pub quizzes we had. Thank Dr. Dominic Rouse and Lizzie for sharing their facilities with me, and Dr. Neel Mackinnon for sharing the experience of thesis writing. Thanks Prof. Sarah Croke and Dr. Fiona Speirits for their discussions in physics and concerns in daily life. Thanks Dr. Niclas Westerberg, Dr. Robert Bennett and Dr. Felipe Isaule Rodríguez for all the inspiring discussions in office.

Collectively, the Quantum Theory group is like a very warm family, every individual is kind, friendly and supportive, this soft atmosphere is a must for my uneasy personalities. Thanks Scarlett (Dr. Sijia Gao) for introducing me to this group where I started my adventure in physics research.

I would like to sincerely thank my two examiners, Dr. Alison Yao and Dr. Robert Bennett, whose invaluable feedback greatly helped me in rewriting and organizing the thesis. Without their guidance, the thesis would not have reached its current quality.

Thanks to all the good people I met in Glasgow. You are all amazing and special. Thanks to my friend Zinuo Li for always accompany me to all sorts of funny places and making me exquisite handcrafts. Thanks Tsai-yu Lee who is always enthusiastic and cheerful, and helped me in every aspect of life. Thanks Dr. Russell Drummond who has been my medical doctor throughout my time in Glasgow, for giving all the helpful consultations and advises on diabetes, and I am grateful for all the encouragement all the way throughout years and the touching special goodbye letter and the best wishes.

Finally, I would like to thank all my family and friends. A special thanks to Jing Qu who has been friend with me for over 10 years, who knows everything about me and has always been helpful and willing to discuss everything, supporting me and giving advices on all matters. Thanks to Zhanqiu Wang whom I know from master time in Glasgow, who has been kind, considerate and understanding, giving me faith when I am down. And Yichen Liu for always been relaxing and humorous, always bringing interesting discussions and laughter. Thanks to my roommate and friend Sin I Ng for tolerating my bad temper and all the funny moments we shared togather. Thanks to my friend and pen pal Tsai-yi Peng, for always praising and appreciating my Chinese writings, and for sharing all the different ideas. Thank my parents for all the support financially and emotionally, and all my other relatives for always caring about me. You are all amazing individuals who are special and important in my life.

Author's Declaration

I certify that the thesis presented here for examination for a PhD degree of the University of Glasgow is solely my own work other than where I have clearly indicated that it is the work of others (in which case the extent of any work carried out jointly by me and any other person is clearly identified in it) and that the thesis has not been edited by a third party beyond what is permitted by the University's PGR Code of Practice.

The copyright of this thesis rests with the author. No quotation from it is permitted without full acknowledgement.

I declare that the thesis does not include work forming part of a thesis presented successfully for another degree.

I declare that this thesis has been produced in accordance with the University of Glasgow's Code of Good Practice in Research.

I acknowledge that if any issues are raised regarding good research practice based on review of the thesis, the examination may be postponed pending the outcome of any investigation of the issues.

Publications

Below is a list of publications I have co-authored during my PhD, which have either been published, or are currently under preparation. Conference papers are not included.

1. Z. Ye, S. M. Barnett, S. Franke-Arnold, J. B. Götte, A. McWilliam, F. C. Speirits, and C. M. Cisowski, "Theory of paraxial optical skyrmions," Proceedings of the Royal Society A: Mathematical, Physical and Engineering Sciences, vol. 480, no. 2297, p. 20240109, 2024.

2. Z. Ye, J. B. Götte, and C. M. Cisowski, "An atlas of optical skyrmions: charting topologically equivalent field configurations," Journal of Optics, vol. 27, p. 042502, 2025.

3. A. McWilliam, C. M. Cisowski, Z. Ye, F. C. Speirits, J. B. Götte, S. M. Barnett, and S. Franke-Arnold, "Topological Approach of Characterizing Optical Skyrmions and Multi-skyrmions," Laser & Photonics Reviews, vol. 17, p. 2200155, 2023.

4. Faraday Effect for Strongly Focused Vector Vortex Beams (In progress)

The contents of the **first publication** are included in chapter 4. I contributed to the initial draft, developed part of the theoretical framework—particularly the topological method for calculating skyrmion numbers—and generated several of the figures.

The **second publication** corresponds to chapter 5, where I was responsible for the entire theoretical development and took the lead in writing the first draft.

The **third publication**, also included in chapter 5, involved my contributions to part of the theory, as well as participation in experiment design and data analysis.

The **fourth work** is currently under preparation, and its contents are presented in chapter 3. I am responsible for the entire theoretical component of this work.

List of Figures

Chapter 1

Introduction

Optics has a long history: In the 10th century, Ibn al-Haytham (Alhazen) used a pinhole camera to demonstrate that light travels in straight lines, laying the groundwork for geometrical optics [1]. In the 17th century, Isaac Newton employed a prism to disperse white light into its constituent colors, revealing the spectral composition of light [2]. This was followed by Thomas Young's groundbreaking double-slit experiment, which provided critical evidence of the wave nature of light and laid the foundation for interferometry [3, 4]. Around the same period, Étienne-Louis Malus discovered the polarization property of light [5], which was further developed into a comprehensive theory by Augustin-Jean Fresnel [6]. These foundational studies collectively paved the way for modern concepts of structured light.

While classical optics focused on fundamental properties like intensity and wavelength, structured light expands these principles by enabling precise control over intensity, phase, and polarization [4]. While the term "structured light" is relatively modern, its conceptual foundation can be traced back to earlier scientific explorations of light, where it originally referred to intensity patterns in a particular plane [7]. With major technical advancements in holographic techniques, including spatial light modulators (SLMs) and digital micromirror devices (DMDs), high-speed dynamic control of structured light fields has become possible [8, 9].

In recent years, the theory of structured light has developed rapidly, evolving from the study of specific transverse modes of light [10] to the creation of tailored spatial-temporal light fields [11]. Its applications are broad, including but not limited to optical communications [12], quantum information processing [13], and super-resolution imaging [14].

In this thesis, we investigate spatially varying polarization patterns, including vector vortex beams—beams with helical phase structures—and optical skyrmions, which are topologically protected light structures characterized by intricate, twisting polarization patterns embedded within the polarization fields of vector light beams. We are particularly interested in the behaviour of such optical fields under phenomena that affect polarization, such as the Faraday effect, which rotates polarization, and strong focusing, which alters the transverse polarization and induces a longitudinal component. Strong focusing has numerous applications, such as particle acceleration [15], second-harmonic generation [16], and fluorescent imaging [17].

In 1845, the pioneering experimental physicist Michael Faraday observed the rotation of the polarization plane when he passed a polarized beam through a transparent material placed in a magnetic field [18, 19]. This phenomenon was later named the Faraday effect, a remarkable discovery demonstrating the interaction between light and magnetic field, confirming that light is an electromagnetic phenomenon.

The Faraday effect has been extensively studied. While it is well-understood in linearly polarized light, its interaction with structured light, particularly vector vortex beams, remains unexplored, forming one key focus of this thesis. We investigate how a vector vortex beam interacts with a Faraday medium (or equivalently, a dielectric medium under a magnetic field). We identify a secondary effect, distinct from the linear Faraday effect. This secondary effect, arising from the complex structure of vector vortex beams and exhibiting as inhomogeneous rotation and changes in polarization ellipticity, is relatively small in the paraxial regime, where the beam remains nearly collimated. However, when a strongly focused radially polarized beam is used, this secondary effect is magnified, reaching a level comparable to the linear Faraday effect. This results in a subtle inhomogeneous rotation of the polarization structure, with the ellipticity of the polarization ellipses increasing as the beam approaches the focal plane.

Skyrmions were first introduced in the field of particle theory [20], later extended to magnetic materials [21], and more recently to optics [22, 23]. Tony Skyrme first proposed the concept of skyrmions in nuclear physics, a pioneering idea that has since had wide-reaching implications [24, 20]. In 1961, he introduced a topological model to describe baryons, representing them as solitons (localized, stable waves that do not dissipate) in a field theory. This model of solitons later became known as skyrmions, in honor of Skyrme's work. Since then, these quasi-particles have been predicted and observed in diverse contexts, including string theory [25], Bose condensates and atoms [26, 27], spintronics [28], magnetic media [29, 30, 31], and more recently in plasmonics and optics [32, 23, 33, 22, 34]. While the more familiar magnetic skyrmions are associated with magnetic spin textures, optical skyrmions are embedded in the polarization structure of complex vector light fields.

Optical skyrmions are quasiparticles with non-trivial topological structures, characterized by a topological invariant known as the skyrmion number (Figure. 1.1). This topology, crucial for describing the quantized model, remains preserved under deformations unless the skyrmion is destroyed. For instance, the field lines of a skyrmion cannot be separated without topologically destroying the structure. The skyrmion model has applications in various fields, including condensed matter physics and optics [35, 21, 36]. In magnetic skyrmions, the configuration of spin textures is topologically stable. Similarly, in optical skyrmions, the polarization distributions are constructed in a manner analogous to their magnetic counterparts [22].

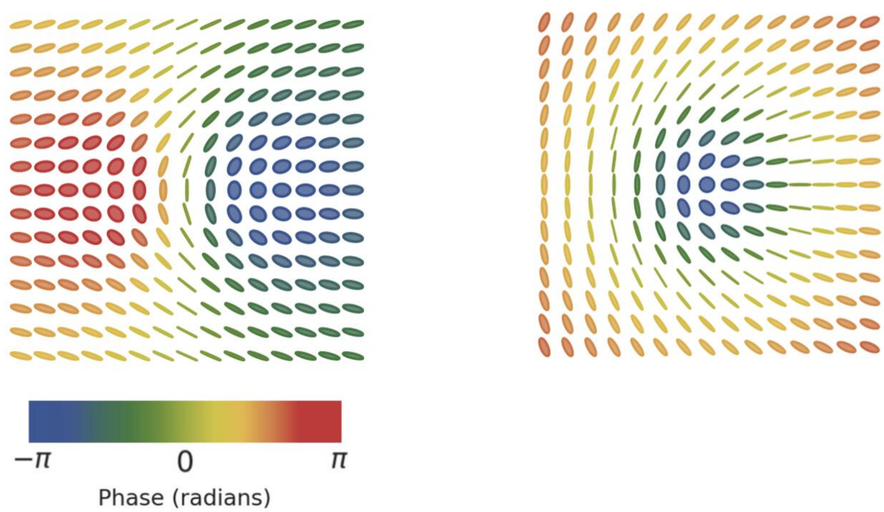

Figure 1.1: An illustrative example of an $n = 1$ bimeron (left) and skyrmion (right). A bimeron is a configuration involving two distinct regions of opposite topological charge, while a skyrmion configuration has opposite circular polarizations at the beam centre and periphery, which theoretically extends to infinity.

The skyrmion number, which characterizes the singularities of the field, can be understood as a measure of the flux of the skyrmion field in a transverse cross-section. It can be calculated using a vector potential defined in terms of the skyrmion field [22, 37]. However, this method lacks satisfactory precision, as measuring the skyrmion field, and consequently the vector potential, becomes challenging in low-intensity regions, an issue that warrants further exploration. We propose an alternative topological definition using the Stokes phase, which measures the skyrmion number by the variation of the Stokes phase along an integral path. This approach is closely linked to the winding number, which counts the number of turns made by the Stokes vector on the Poincaré sphere. The Stokes phase, which can be determined from experimentally accessible Stokes parameters, provides a reliable measurement of the skyrmion number in what we call a consistent basis measurement, meaning that the basis used to construct the skyrmion beam and the basis used to measure it are consistent. This method offers higher experimental precision. Furthermore, we demonstrate that a mixed-up bases measurement is possible, where the basis used to construct the skyrmion beam and the basis used to measure it are chosen independently. This generalized measurement not only extends the definition of singularities but also provides even higher measurement precision in the lab. In this generalized measurement framework, we identify the topological equivalence between a skyrmion and a bimeron, a configuration involving two distinct regions of opposite topological charge (Figure. 1.1). These configurations, including countless intermediate states, are topological transitions of one another, meaning they are topologically equivalent.

Well-established models exist for describing 2D polarization, such as Stokes parameters, the polarization ellipse, and the Poincaré sphere [6, 38]. In recent years, there has been increasing interest in research fields such as nano-optics [39] and microscopy [40] in examining the polarization of light in scenarios where all three components of the polarization vector are non-negligible. Earlier theoretical models primarily explored the propagating and focusing aspects of the field through the angular spectrum method, as demonstrated in the strong focusing system model of Richards and Wolf [41, 39]. However, simulations are typically limited to a 2D polarization description.

In 2D polarization, the polarization vectors lie in a plane perpendicular to the propagation direction, meaning that a $\mathbb{CP}^1$ space (complex projective plane), which is homeomorphic to $\mathbb{S}^2$ (surface of a sphere), is sufficient to capture all their features. For 3D polarizations, traditional Stokes parameters and Poincaré sphere representations fail to capture their full complexity. In this thesis, we propose a two-sphere method to fully describe the features of 3D polarization distributions by separately characterizing ellipticity and spin orientation, enabling a complete description of 3D fields.

In summary, this thesis consists primarily of three parts:

The first part includes chapter 2, which introduces the background of structured light and the strong focusing system originally proposed by Richards and Wolf [41] and further developed by Novotny and Hecht [39]. It also includes chapter 3, which presents one application of the concepts introduced in chapter 2. In chapter 3, we examine how the polarization structure of a radially polarized beam changes after undergoing strong focusing.

The second part of this thesis includes chapter 4 and chapter 5. In chapter 4, we introduce the concept of optical skyrmions, a recently developed theory describing a specific type of structured light beam. In chapter 5, we generalize the concept of paraxial skyrmions and demonstrate that bimerons are one topological transition of skyrmions. Furthermore, we extend the theoretical framework of skyrmions to include all their topological equivalents. Additionally, we present experimental results which demonstrate how this generalization improves the practical measurement of skyrmion numbers.

The third part is presented in chapter 6, where we develop a two-sphere method to describe 3D polarization fields. As a specific example, we apply the strong focusing system to focus an $n = 2$ paraxial skyrmion. This focusing process results in a 3D polarized field, and we demonstrate how our newly developed theory can be used to analyze it.

Finally, the conclusion chapter (chapter 7) summarizes the work presented in this thesis.

Chapter 2

Introduction to Structured Light and Strong Focusing System

2.1 Introduction

In this chapter, we present the background theory relevant to the research themes discussed in the upcoming chapters. We begin by introducing the basics of structured light (section 2.2), which is distinct from classical optical models, where the polarization of the beam is either ignored or treated as homogeneous.

Next, we introduce the paraxial optical model (section 2.3), which is one class of solutions to the Helmholtz equation, a fundamental wave equation that describes the spatial variation of monochromatic waves, under the paraxial approximation. Unless stated otherwise (e.g., in the case of strong focusing), we primarily work within the paraxial regime throughout this thesis. One approach to solving the Helmholtz equation employs the angular spectrum representation (subsection 2.3.1), a mathematical technique derived using Fourier transformations. Another widely used class of solutions consists of Gaussian beams and their higher-order forms (subsection 2.3.2). Here, we introduce Hermite-Gaussian (HG) and Laguerre-Gaussian (LG) beams, two important families of higher-order Gaussian beams that play an important role in structured light research. These beams, along with Fourier analysis, will be used in subsequent chapters.

We then introduce the Gouy phase in section 2.4, which describes an additional phase shift experienced by a beam as it propagates through a focus. This effect is essentially a result of the transverse momentum of the beam, and is particularly important when analyzing beam transitions, such as mode conversions and focusing systems. The concept of polarization is introduced in section 2.5, along with two important tools for its geometric representation: the polarization ellipse (subsection 2.5.1) and the Poincaré sphere (subsection 2.5.2). These two geometric representations are closely related through appropriate mathematical mappings.

Finally, in section 2.6, we introduce the aplanatic system, a strong focusing model based on the Richards and Wolf framework. This system has significant applications in later chapters.

2.2 Structured Light

Optical science has a long history that can be traced back to ancient Egypt, beginning with the invention of lenses and the subsequent development of theories in geometrical optics [42]. For a long time, optical science was grounded in classical and relatively simple models, such as plane waves and spherical waves, with geometrical optics serving as a useful framework for these models [6]. This traditional approach was transformed by the advent of structured light, which was driven by rapid advancements in optical technologies. These developments in theory, in turn, stimulated further progress in the design and functionality of optical instruments.

Structured light refers to light beams with strong spatial inhomogeneity in beam parameters, such as amplitude, phase, and polarization [43, 7]. The study of structured light emphasizes characterizing vortices and singularities [43]. It introduces seemingly abstract concepts, including phase singularities, polarizations, chiralities, and helicities. Structured light has numerous applications, including optical manipulation [44], optical metrology [45], nano-probing [46], and data processing.

2.3 Paraxial Optical Fields

In this section, we will introduce the paraxial beam model, which is a useful model for many optical systems where light beams propagate along a fixed direction with a small spread in the transverse direction [39]. We begin with the mathematical descriptions of the paraxial system.

A wave equation can be derived from the well-known Maxwell equations, which we quote here [3]:

$$\begin{aligned}
\nabla \cdot \mathbf{E} &= 0, \\
\nabla \times \mathbf{E} &= -\frac{\partial \mathbf{B}}{\partial t}, \\
\nabla \cdot \mathbf{B} &= 0, \\
\nabla \times \mathbf{B} &= \mu_0 \varepsilon_0 \frac{\partial \mathbf{E}}{\partial t}.
\end{aligned} \tag{2.1}$$

These equations assume free space with the absence of free charge or current, where $\mathbf{E}$ refers to the electric field, and $\mathbf{B}$ refers to the magnetic field, and μ_0 and ε_0 represent the permeability and permittivity in the vacuum. If we take the curl of the second equation and eliminate $\mathbf{B}$ by substituting the last equation, we obtain the wave equation:

$$\nabla^2\mathbf{E} - \frac{1}{c^2}\frac{\partial^2\mathbf{E}}{\partial^2 t} = 0. \tag{2.2}$$

This vector form of the wave equation can be simplified to a scalar form, where transversality links the components in space [47]

$$\nabla^2 u\left(\mathbf{r}, t\right) = \frac{1}{c^2}\frac{\partial^2 u\left(\mathbf{r}, t\right)}{\partial t^2}, \tag{2.3}$$

where $u\left(\mathbf{r}, t\right)$ denotes the magnitude of $\mathbf{E}$ as a function of space $\mathbf{r} = (x, y, z)$ and time t, and c represents the speed of light. In Cartesian coordinates, $u_x(\mathbf{r}, t)$ and $u_y(\mathbf{r}, t)$ are the transverse components, while $u_z(\mathbf{r}, t)$ is the longitudinal component. In this context, we are particularly interested in a transverse electromagnetic (TEM) wave, which is a solution to the wave equation.

We limit our discussions to monochromatic beams and apply the usual assumptions: assuming a monochromatic wave that originates at $z = 0$ and propagates in the $+z$ direction. This form of solution separates the time dependence of the wave function, allowing us to express the temporal part as $\mathrm{e}^{-i\omega t}$, where ω is the frequency of the light. Substituting the solution $u\left(x, y, z, t\right) = U_0\left(x, y, z\right)\mathrm{e}^{-i\omega t}$ into Eq. (2.3), we obtain a time-independent wave equation, also known as the Helmholtz equation, a fundamental wave equation that describes the spatial variation of monochromatic waves, as

$$\nabla^2 U_0(x, y, z) + k^2 U_0(x, y, z) = 0, \tag{2.4}$$

where $k = \omega/c$ is the wave number.

Finally, the paraxial approximation is considered. Such approximation allow us to write a relation $U_0\left(x, y, z\right) = E\left(x, y, z\right)\mathrm{e}^{ikz}$, where the propagation term e^{ikz} is separated. The conditions for the paraxial approximation require that [48]

$$\left|\frac{\partial^2 E}{\partial z^2}\right| \ll \left|2k\frac{\partial E}{\partial z}\right|, \quad \left|\frac{\partial^2 E}{\partial z^2}\right| \ll \left|\frac{\partial^2 E}{\partial x^2} + \frac{\partial^2 E}{\partial y^2}\right|, \tag{2.5}$$

these inequalities require that the second derivative with respect to z is small compared to other terms and can therefore be ignored. if we substitute the relation $u\left(x, y, z, t\right) = E\left(x, y, z\right)\mathrm{e}^{ikz}\mathrm{e}^{-i\omega t}$ into Eq. (2.3) and drop the second derivative with respect to z term, we will eventually arrive at the paraxial wave equation:

$$\nabla_\perp^2 E + 2ik\frac{\partial E}{\partial z} = 0, \tag{2.6}$$

where $\nabla_\perp^2$ represents the transverse Laplacian. The most prevalent solution to the paraxial wave equation is perhaps the famous Gaussian beam, which we will discuss in later subsection.

Another way of solving the wave equation is to go back to Eq. (2.4) and make approximations to its solutions. For a detailed treatment, we refer the reader to Chapter 16 of *Lasers* by Siegman [49]. Here, we briefly recap the solution process.

It was Huygens' original idea that each point on a wavefront can be considered a source of a secondary spherical wave [50]. The total field distribution is then obtained by integrating these spherical contributions, accounting for the geometry of the wavefront. With Fresnel approximation, the field can be written as

$$U_0(x,y,z) = \frac{e^{ikz}}{i\lambda z} \iint_{-\infty}^{\infty} U_0(x',y',0) \exp\left[\frac{ik}{2z}\left((x-x')^2 + (y-y')^2\right)\right] dx'dy', \tag{2.7}$$

where λ is the wavelength, and the source plane is assumed to be at $z = 0$. Thus, $(x', y', 0)$ refers to a point on the source plane, and (x, y, z) refers to a field point. Here we used $\rho = \sqrt{(x-x')^2 + (y-y')^2 + z^2} \approx z + \frac{(x-x')^2+(y-y')^2}{2z}$, which is the Fresnel approximation.

Both the Gaussian beam solution and the Huygens-Fresnel integral method give equivalent results [51]. These solutions bring important concepts that are widely used in optics, which we will explain in the following subsections. First, we introduce the angular spectrum method, which provides a general solution to the scalar wave equation by expressing the field as a superposition of plane waves. Under the paraxial approximation, this method leads to the Fresnel diffraction integral, where the quadratic phase approximation of the propagation term is applied [49, 52]. Then, we introduce the Gaussian beam solution, which is a direct solution to the paraxial wave equation.

2.3.1 Angular Spectrum Representation of Optical Fields

Optical fields can be described as a superposition of plane waves and evanescent waves, both of which are physical solutions to the Maxwell equations [39, 52]. In the paraxial regime, this decomposition naturally leads to the representation of the angular spectrum, which falls within the framework of Fourier optics.

Assuming a fixed plane $z = 0$ transverse to the propagation direction, the field can be written in terms of its two-dimensional Fourier transform and vice versa [39]:

$$\begin{aligned} \hat{\mathbf{E}}(k_x, k_y; 0) &= \frac{1}{4\pi^2} \iint_{-\infty}^{\infty} \mathbf{E}(x,y,0) \mathrm{e}^{-i[k_x x + k_y y]} \mathrm{d}x \mathrm{d}y, \\ \mathbf{E}(x,y,0) &= \iint_{-\infty}^{\infty} \hat{\mathbf{E}}(k_x, k_y; 0) \mathrm{e}^{i[k_x x + k_y y]} \mathrm{d}k_x \mathrm{d}k_y, \end{aligned} \tag{2.8}$$

where $\hat{\mathbf{E}}(k_x, k_y)$ is the angular spectrum, i.e., the spatial Fourier transform of the field at the plane $z = 0$.

If the field propagates to a distance z, we have

$$\mathbf{E}(x, y, z) = \iint_{-\infty}^{\infty} \hat{\mathbf{E}}\left(k_x, k_y; 0\right) \mathrm{e}^{i[k_x x + k_y y + k_z z]} \mathrm{d}k_x \mathrm{d}k_y, \tag{2.9}$$

where $k_z = \sqrt{k^2 - k_x^2 - k_y^2}$. This is the angular spectrum representation, a rigorous solution to the Helmholtz equation.

For a scalar field U_0 at $z = 0$, we have

$$\begin{aligned} U_0(x, y, 0) &= \iint_{-\infty}^{\infty} A\left(k_x, k_y; 0\right) \mathrm{e}^{i[k_x x + k_y y]} \mathrm{d}k_x \mathrm{d}k_y, \\ A\left(k_x, k_y; 0\right) &= \frac{1}{4\pi^2} \iint_{-\infty}^{\infty} U_0(x, y, 0) \mathrm{e}^{-i[k_x x + k_y y]} \mathrm{d}x \mathrm{d}y, \end{aligned} \tag{2.10}$$

where $A\left(k_x, k_y; 0\right)$ is the angular spectrum of $U_0(x, y, 0)$.

Under the paraxial approximation, where $k_x, k_y \ll k$, we can expand k_z as

$$k_z \approx k - \frac{k_x^2 + k_y^2}{2k}, \tag{2.11}$$

substituting into the scalar form of Eq. (2.9), we derive

$$\begin{aligned} U_0(x, y, z) &= \iint_{-\infty}^{\infty} A\left(k_x, k_y; 0\right) e^{i\left[k_x x + k_y y + \left(k - \frac{k_x^2 + k_y^2}{2k}\right) z\right]} \mathrm{d}k_x \mathrm{d}k_y \\ &= \frac{e^{ikz}}{4\pi^2} \iint_{-\infty}^{\infty} \left(\iint_{-\infty}^{\infty} \mathrm{e}^{i(k_x(x - x') + k_y(y - y'))} e^{i\frac{z}{2k}\left(k_x^2 + k_y^2\right)} \mathrm{d}k_x \mathrm{d}k_y \right) U_0(x', y', 0) \mathrm{d}x' \mathrm{d}y' \\ &= \frac{e^{ikz}}{4\pi^2} \iint_{-\infty}^{\infty} \frac{2\pi k}{iz} \exp\left(\frac{ik}{2z}\left((x - x')^2 + (y - y')^2\right)\right) U_0(x', y', 0) \mathrm{d}x' \mathrm{d}y' \\ &= \frac{e^{ikz}}{iz\lambda} \iint_{-\infty}^{\infty} U_0(x', y', 0) \exp\left(\frac{ik}{2z}\left((x - x')^2 + (y - y')^2\right)\right) \mathrm{d}x' \mathrm{d}y', \end{aligned} \tag{2.12}$$

where we used $\lambda = 2\pi/k$, and the Gaussian integral $\int_{-\infty}^{\infty} \exp\left(-a x_i^2 + b x_i\right) dx_i = \sqrt{\frac{\pi}{a}} \exp\left(\frac{b^2}{4a}\right)$, with $a = i\frac{z}{2k}$, $b = i(x_i - x_i')$ and $x_i = x, y$. This is the Fresnel diffraction integral (Eq. (2.7)) we obtained before. Therefore, we showed that the angular spectrum method can lead to the Fresnel diffraction integral under the paraxial approximation.

In summary, the angular spectrum method provides a rigorous and general framework for modeling wave propagation by decomposing the field into plane waves via Fourier transform. Under the paraxial approximation, the accumulated phase of these components simplifies, and the inverse Fourier transform yields the Fresnel diffraction integral. This derivation reveals how paraxial diffraction naturally emerges from the exact wave description in the Fourier space.

2.3.2 Gaussian Beam and Higher Order Beams

To solve the paraxial wave equation $\nabla_{\perp}^2 E + 2ik\frac{\partial E}{\partial z} = 0$, we take 2D spatial Fourier transform in the transverse coordinates. Thus, $\nabla_{\perp}^2 E$ is transformed to $-(k_x^2 + k_y^2)\hat{E}$ and $\frac{\partial E}{\partial z}$ is transformed to $\frac{\partial \hat{E}}{\partial z}$. The relation between E and $\hat{E}$ is

$$\hat{E}\left(k_x, k_y; z\right) = \frac{1}{4\pi^2} \iint E\left(x, y, z\right) e^{-i\left(k_x x + k_y y\right)} \mathrm{d}x\mathrm{d}y, \tag{2.13}$$

and the paraxial wave equation becomes

$$-\left(k_x^2 + k_y^2\right)\hat{E} + 2ik\frac{\partial \hat{E}}{\partial z} = 0. \tag{2.14}$$

The solution to this ordinary differential equation is not difficult to obtain, which reads

$$\hat{E}\left(k_x, k_y; z\right) = \hat{E}\left(k_x, k_y; 0\right) \cdot \exp\left(i\frac{k_x^2 + k_y^2}{2k}z\right). \tag{2.15}$$

We assume a Gaussian distribution at the beam waist ($z = 0$) [6, 39], as

$$E\left(x, y, 0\right) = E_0 e^{-\frac{x^2 + y^2}{w_0^2}}, \tag{2.16}$$

where w_0 represents the beam waist radius, and E_0 is a constant. The Fourier transform can be performed to obtain its angular spectrum

$$\begin{aligned} \hat{E}\left(k_x, k_y; 0\right) &= \frac{1}{4\pi^2} \iint_{-\infty}^{\infty} E_0 e^{-\frac{x^2+y^2}{w_0^2}} e^{-i\left[k_x x + k_y y\right]} \mathrm{d}x\mathrm{d}y \\ &= E_0 \frac{w_0^2}{4\pi} \mathrm{e}^{-\left(k_x^2 + k_y^2\right)\frac{w_0^2}{4}}, \end{aligned} \tag{2.17}$$

where the Gaussian integral (see previous subsection for details) is used. Substituting Eq. (2.17) into Eq. (2.15) and then into Eq. (2.13), perform the inverse Fourier transform, and apply the Gaussian integral, we obtain

$$E(x, y, z) = \frac{E_0 \mathrm{e}^{ikz}}{1 + 2iz/\left(kw_0^2\right)} \mathrm{e}^{-\frac{\left(x^2+y^2\right)}{w_0^2}\frac{1}{1+2iz/\left(kw_0^2\right)}}. \tag{2.18}$$

If we assume cylindrical symmetry around z-axis, and let $\rho^2 = x^2 + y^2$, we obtain

$$E(\rho, z) = E_0 \frac{w_0}{w(z)} \mathrm{e}^{-\frac{\rho^2}{w^2(z)}} \mathrm{e}^{i\left[kz - \varphi_g + k\rho^2/(2R(z))\right]}, \tag{2.19}$$

where some new parameters are defined here for a better physical meaning: $z_R = \frac{kw_0^2}{2}$ is the Rayleigh range, $w(z) = w_0\sqrt{1+\frac{z^2}{z_R^2}}$ is the beam radius, $R(z) = z\left(1+\frac{z_R^2}{z^2}\right)$ is the wavefront radius and $\varphi_g = \arctan\left(\frac{z}{z_R}\right)$ is the Gouy phase [39]. The relevant parameters are shown in Figure. 2.1.

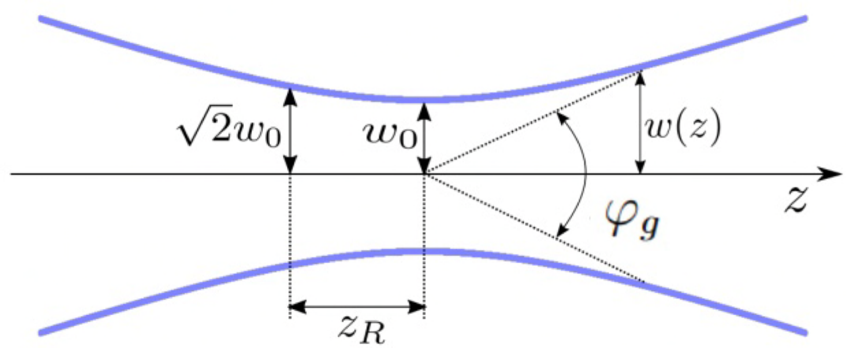

Figure 2.1: A fundamental Gaussian beam with relevant parameters, where w_0 is the beam waist, $w(z)$ is the beam waist as a function of z. z_R is the Rayleigh range, corresponds to the distance from beam waist to $\sqrt{2}w_0$. And φ_g which is the angle between the asymptotic lines, is the Gouy phase.

There are different ways to derive Gaussian beams, Siegman [49] pointed out that a Gaussian beam can be constructed from a spherical wave by shifting the source point to the complex plane. This approach constructs a complex wave quantity whose real and imaginary parts are related to the radius of curvature $R(z)$ and the spot size of the beam $w(z)$. This resolves the infinite energy problem of the spherical wave, which is of course, unphysical. The derivation of the Gaussian beam is the core result of this subsection, the paraxial form of the Gaussian beam. We will introduce next how it is linked with higher order Hermite-Gaussian (HG) beams and Laguerre-Gaussian (LG) beams which are frequently used in later context.

As higher order Gaussian beams, HG beams and LG beams are also solutions to the paraxial Helmholtz equation, and each forms a complete basis set of solutions. HG beams are solutions under rectangular coordinate system, while LG beams are solutions under cylindrical coordinates. The fundamental Gaussian beam serves as the lowest-order mode of both beams [49, 53].

The generating functions for higher order HG and LG beams were proposed by Zauderer [39, 54], as follows:

$$\begin{aligned}\mathbf{E}^{\mathrm{HG}}_{nm}(x,y,z) &= w_0^{n+m}\frac{\partial^n}{\partial x^n}\frac{\partial^m}{\partial y^m}\mathbf{E}(x,y,z),\\ \mathbf{E}^{\mathrm{LG}}_{pl}(x,y,z) &= k^p w_0^{2p+l}\mathrm{e}^{ikz}\frac{\partial^p}{\partial z^p}\left(\frac{\partial}{\partial x}+i\frac{\partial}{\partial y}\right)^l\left\{\mathbf{E}(x,y,z)\mathrm{e}^{-ikz}\right\}\\ &= k^p w_0^{2p+l}\mathrm{e}^{ikz}\frac{\partial^p}{\partial z^p}\left(\frac{\partial}{\partial\bar{\rho}}\right)^l\left\{\mathbf{E}(\rho,z)\mathrm{e}^{-ikz}\right\},\end{aligned} \tag{2.20}$$

where $\bar{\rho}=x-iy$ denotes the complex conjugate of ρ. Zauderer showed that HG and LG modes with complex arguments (in polynomials) are paraxial limits of multipole solutions of the Helmholtz equation. These are still physical modes in real space but generated via complex-analytic methods. This framework provides a compact representation and facilitates mode conversion between HG and LG beams, and will be utilized in later chapters.

The relations between these modes can be compared with relations between orthonormal states on the Poincaré sphere, and by analogy we can construct higher order mode spheres [55]. There are also other forms of the generating function, people constructed generating function using ladder operators [56]. Higher-order solutions can also be obtained via suitable trial solutions, as pointed out in [49].

The commonly used indices for LG beams are l and p, which are related to the Cartesian indices m and n via the following expressions [57]

$$\begin{aligned}p &= \min(m,n),\\ l &= m-n,\\ 2p+|l| &= m+n.\end{aligned} \tag{2.21}$$

For LG beams $p=0,1,2,...$ represents the radial number, and $l=0,\pm1,\pm2,...$ the azimuthal number, which corresponds to the beam's orbital angular momentum (OAM).

If we write Eq. (2.6) in cylindrical coordinates, we obtain

$$\left(\frac{1}{\rho}\frac{\partial}{\partial\rho}\left(\rho\frac{\partial}{\partial\rho}\right)+\frac{1}{\rho^2}\frac{\partial^2}{\partial\phi^2}+2ik\frac{\partial}{\partial z}\right)\mathrm{LG}^l_p=0, \tag{2.22}$$

where $\rho=\sqrt{x^2+y^2}$ is the radial coordinate, and ϕ is the azimuthal angle. Solving this yields the Laguerre–Gaussian (LG) beams. A general expression for the LG beams is given in [53]:

$$
\begin{aligned}
\mathrm{LG}_p^l\left(\rho,\phi,z\right) = \sqrt{\frac{2p!}{\pi\left(p+|l|!\right)}}\ \frac{1}{w\left(z\right)}\ \left(\frac{\sqrt{2}\rho}{w\left(z\right)}\right)^{|l|}\cdot \\
L_p^{|l|}\left(\frac{2\rho^2}{w\left(z\right)^2}\right)\ \mathrm{e}^{-\frac{\rho^2}{w(z)^2}}\ \mathrm{e}^{i\left(l\phi+\frac{k\rho^2}{2R(z)}-(2p+|l|+1)\varphi_g\right)},
\end{aligned}
\tag{2.23}
$$

where $L_p^{|l|}$ is the associated Laguerre polynomial, and all other parameters are defined as before. LG beams are therefore determined by three parameters: p, l and w_0. A figure of various LG modes is given in Figure. 2.2 to illustrate the meaning of these indices. These beams have cylindrical symmetry, where the intensity is the same on each ring. The index l is also called the topological charge of the beam [10], a concept that naturally leads to vortex beams, which are beams with a spiral phase distribution [10, 58]. The wavefront of a vortex beam spirals along the optical axis and has zero energy in its centre [59]. The topological charge can be calculated by doing a path integral around the phase singularity, where the jump of the phase happens [60]. This topological property of the vortex beams means it is very robust and is linked to our studies discussed later.

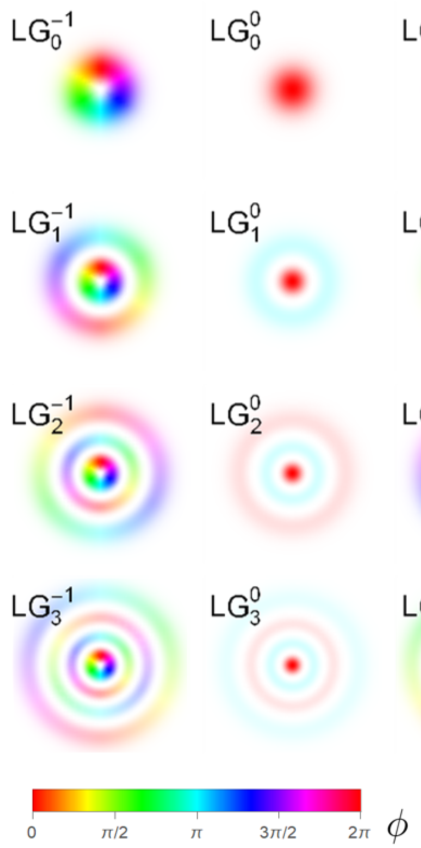

Figure 2.2: A figure illustrating various LG modes, showing both intensity and phase, where deeper colors indicate higher intensity [61].

2.4 Gouy Phase

In the previous section we have introduced the concept of Gouy phase as one of the beam parameters. We will now give some further introduction about this important and interesting phenomenon whose importance will become clear in later chapters.

Gouy performed an experiment back in 1891, where he reflected the beam from the same light source with both a flat mirror and a curved one. The focused beam is then interfered with the non-focused one. Gouy observed a phase shift from the center of the diffraction pattern, which was later named after him as the Gouy phase [62].

Gouy phase was once considered a phase anomaly [63]. There are many explanations about this phase change, which occurs when the beam passes through its focus. Boyd [63] provides an intuitive explanation, interpreting the Gouy phase as a phase difference between a Gaussian beam and an infinite plane wave. The Gouy phase can thus be understood as the optical path difference between the geometrical optics model and the optical path resulting from diffraction, as explained in Figure. 2.3.

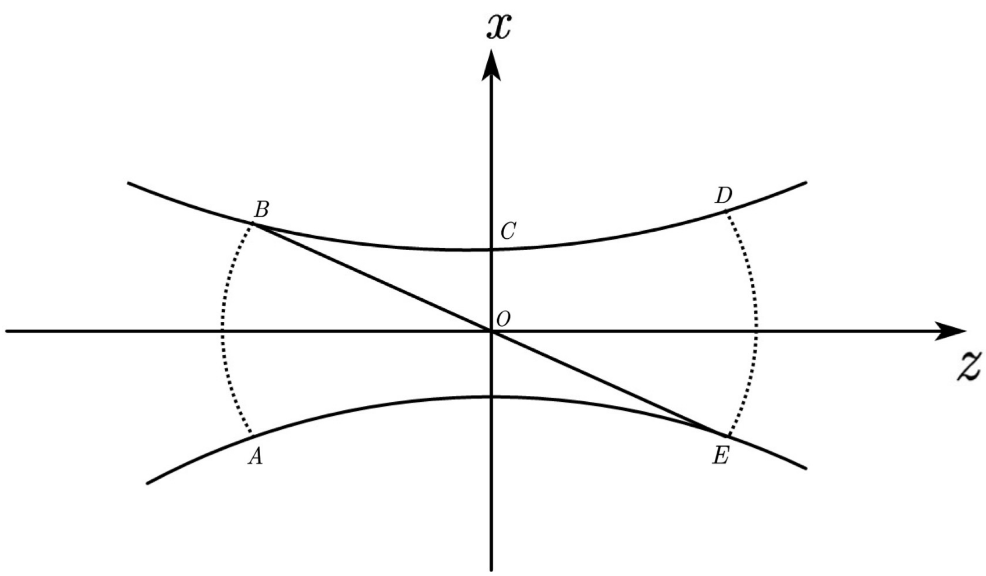

Figure 2.3: The optical path lengths of the wavefronts AB and DE are compared. The geometrical path length is the straight line BE, while the path length caused by diffraction is BCD. The difference between these two paths results in the phase anomaly [63].

But a deeper understanding can be gained by examining the quantum behavior of the light, as pointed out by Feng in [64], which also provides a compatible explanation for the previous claim that the Gouy phase is a phase difference between a Gaussian beam and an infinite plane wave. We will now give a brief recap of Feng's paper about the derivation and explanation of the Gouy phase.

A beam with finite transverse spread can be written in terms of angular spectrum of plane waves through Fourier transform, as pointed out in subsection 2.3.1. Suppose the beam propagates along z direction, its wave number can be written as

$$k^2 = k_x^2 + k_y^2 + k_z^2. \tag{2.24}$$

It is appropriate to write any averages in terms of this finite beam as

$$\langle \xi \rangle \equiv \frac{\int_{-\infty}^{+\infty} \xi |f(\xi)|^2 \mathrm{d}\xi}{\int_{-\infty}^{+\infty} |f(\xi)|^2 \mathrm{d}\xi}, \tag{2.25}$$

where $f(\xi)$ is the wave distribution, and ξ represents any relevant variables of the function f. For a typical Gaussian beam, the transverse beam profile can be written as

$$\mathrm{E}(\rho, z) = \sqrt{\frac{2}{\pi}} \frac{1}{w(z)} \mathrm{e}^{-\frac{\rho^2}{w^2(z)}}, \tag{2.26}$$

where $\sqrt{\frac{2}{\pi}} \frac{1}{w(z)}$ is a normalization factor, and $w(z)$ is the beam radius as defined in subsection 2.3.2. From Eq. (2.8) we know its Fourier transform can be written as

$$\begin{aligned} \hat{\mathrm{E}}\left(k_x, k_y; z\right) &= \frac{1}{2\pi} \iint_{-\infty}^{\infty} \mathrm{E}(x, y, z) \mathrm{e}^{-i[k_x x + k_y y]} \mathrm{d}x \mathrm{d}y \\ &= \frac{w(z)}{\sqrt{2\pi}} \mathrm{e}^{-\frac{w^2(z)}{4}\left(k_x^2 + k_y^2\right)}. \end{aligned} \tag{2.27}$$

Both Eq. (2.26) and Eq. (2.27) are normalized Gaussian beams. So we can integrate out the expectation values of the beam vector components from Eq. (2.25) as

$$\begin{aligned} \langle k_x^2 \rangle &= \iint_{-\infty}^{\infty} k_x^2 \left| \hat{\mathrm{E}}\left(k_x, k_y; z\right) \right|^2 \mathrm{d}k_x \mathrm{d}k_y \\ &= \frac{1}{w^2(z)} = \langle k_y^2 \rangle. \end{aligned} \tag{2.28}$$

The Gouy phase of a Gaussian beam can then be calculated as

$$\varphi_g = -\frac{1}{k} \int_z \langle k_x^2 \rangle + \langle k_y^2 \rangle \; dz = -\arctan\left(\frac{z}{z_R}\right). \tag{2.29}$$

We see from the above calculation that the Gouy phase is due to the transverse momentum. For an infinite beam, the wave vector is along $\mathbf{z}$, which means the beam has no transverse momentum. This is compatible with the Heisenberg uncertainty principle. When the beam has a finite spread, its has an uncertainty in the momentum, therefore the transverse component in wavevector $\mathbf{k}$, which causes the Gouy phase shift.

In summary, the Gouy phase is an additional π phase shift compared to an ideal plane wave, with most of this shift occuring within one Rayleigh range [49]. We will make use of this fact in later chapters.

2.5 Polarization

Polarization is another important aspect of structured light. It is a property of transverse waves that describes the geometrical orientation of their oscillations [65, 66]. Beams with different polarizations can behave differently in optically active media, thereby influencing the propagation of the beam [67]. By convention, the polarization direction refers to the direction of the electric field vector $\mathbf{E}$, which is perpendicular to the direction of propagation.

Polarization can be categorized as linear, circular, or elliptical, depending on the shape traced by the transverse oscillation of the electric field. Linear and circular polarizations are special cases of the more general elliptical polarization. Elliptical polarization arises when two plane waves with different amplitudes, phases, and polarization directions are superposed. In this context, we assume all light beams are monochromatic, meaning they have a constant phase difference, which results in a steady elliptical trajectory. When the phase difference is $\pi/2$ and the amplitudes are equal, the polarization becomes circular. If only one plane wave is present, the resulting polarization is linear [6].

From Maxwell's equations, we can derive plane wave solutions that describe different types of polarization. Suppose we have a monochromatic plane wave with wavelength λ and frequency f, propagating in the z-direction. Without loss of generality, the electric field of such a wave can be written as [3]:

$$\mathbf{E}\left(t\right) = \mathbf{E}_0 \cos\left(kz - \omega t\right), \tag{2.30}$$

where $k = 2\pi/\lambda$ is the wave number, and $\omega = 2\pi f$ is the angular frequency. This can also be written in the exponential form as $\mathbf{E}(t) = \mathrm{Re}\left\{\mathbf{E}_0 e^{i(kz-\omega t)}\right\}$, where $\mathbf{E}_0$ is a real-valued vector specifying the amplitude and direction of the electric field, and the real part of $\mathbf{E}(t)$ represents the physical field. From the exponential form we recognize the time dependence for the monochromatic wave and the propagation term we introduced earlier.

We have assumed that the beam propagates along the z-axis, such that the electric field $\mathbf{E}$ and magnetic field $\mathbf{B}$ lie in the transverse x-y plane. In this case, the electric field can be expressed as [68]:

$$\mathbf{E}(t) = \begin{pmatrix} E_{0x}\cos(\omega t + \varphi_1) \\ E_{0y}\cos(\omega t + \varphi_2) \end{pmatrix}, \tag{2.31}$$

where E_{0x} and E_{0y} are the amplitudes of the electric field components along the x- and y- axes, respectively, and φ_1 and φ_2 are their respective phase offsets. These phase differences arise from the relative phase delay between the x- and y-components of the wave, and they play a crucial role in determining the polarization state of the beam. Depending on the values of φ_1, φ_2, and the amplitudes, the resulting polarization can be linear, circular, or elliptical.

Eliminating t we can get a relation between the x and y components of $\mathbf{E}(t)$, as

$$E_y^2 E_{0x}^2 - 2E_x E_y E_{0x} E_{0y}\cos\varphi + E_x^2 E_{0y}^2 = E_{0x}^2 E_{0y}^2 \sin^2\varphi, \tag{2.32}$$

where $\varphi = \varphi_1 - \varphi_2$ is the phase difference between E_x and E_y, and E_{0x} and E_{0y} are the constant amplitudes of the x- and y-components. The geometrical relations are shown in Figure. 2.4. The details of the calculations can be found in [69]. It is not difficult to recognize that this function has the form of an ellipse, which is known as the polarization ellipse whose properties are described by Stokes parameters [68].

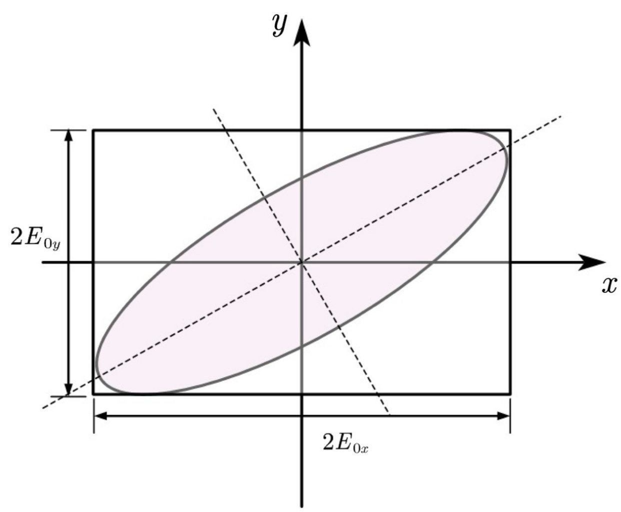

Figure 2.4: A reference rectangle is given, whose side lengths are related to constant amplitudes E_{0x} and E_{0y}. The polarization is circular when $E_{0x} = E_{0y}$, and $\varphi = \pm\pi/2$. The polarization is linear when $E_{0x} = 0$ or $E_{0y} = 0$, or when $E_{0x} = E_{0y}$, and $\varphi = 0$ or $\varphi = \pi$.

2.5.1 Polarization Ellipse and Stokes Parameters

George Gabriel Stokes was a brilliant mathematician and physicist of the 19th century. In his early career, he conducted research in hydrodynamics and acoustics, and later shifted his focus to optics. In the field of optics, he studied the aether, which was then believed to be the medium through which light waves propagate—a widely accepted assumption at the time. He also investigated diffraction phenomena, which refer to the behavior of waves when they encounter obstacles. Later, he focused on ellipsometry [70].

Stokes parameters were introduced before the electromagnetic nature of light was fully understood and served as a useful tool for characterizing experimental measurements [71].

There are four Stokes parameters, typically denoted as $[S_0, S_1, S_2, S_3]$, or alternatively as $[I, Q, U, V]$ by convention. In this thesis, we will adopt the former notation. Their relationships to the parameters of the $\mathbf{E}$ field and the polarization ellipse are as follows: [72]:

$$\begin{aligned} S_0 &= |E_{0x}|^2 + |E_{0y}|^2, \\ S_1 &= |E_{0x}|^2 - |E_{0y}|^2 \ = S_0 \cos 2\chi \cos 2\psi, \\ S_2 &= 2E_{0x}E_{0y}\cos\varphi = S_0 \cos 2\chi \sin 2\psi, \\ S_3 &= 2E_{0x}E_{0y}\sin\varphi = S_0 \sin 2\chi, \end{aligned} \tag{2.33}$$

where we provide two expressions for the Stokes parameters: the expression after the first equal sign is directly related to the parameters introduced in Eq. (2.32), namely the field amplitudes and their relevant phase. The second expression, which follows the second equal sign, introduces new parameters χ and ψ, which have geometrical meanings that we will discuss in the following.

For the purpose of this thesis, we only consider fully polarized light, which, in terms of Stokes parameters, is defined by the condition $S_0^2 = S_1^2 + S_2^2 + S_3^2$ [47]. From Eq. (2.33) we know that S_0 represents the intensity of the beam. The other three parameters measure the degree of polarization in their relevant directions, which will become more obvious in the expression we introduce later (Eq. (2.36)). The geometrical meaning of χ is clear as $\tan\chi$ corresponds to the ratio between the major and minor axes of the polarization ellipse, thus characterizing the ellipticity, and ψ is the angle between the major axis and x-axis, which describes the orientation of the ellipse, as shown in Figure 2.5.

The Stokes parameters can be related to the Jones calculus [73]. Jones calculus represents polarized lights by 2-vectors, as

$$\mathbf{E} = \begin{bmatrix} E_1 e^{i\varphi_1} \\ E_2 e^{i\varphi_2} \end{bmatrix}, \tag{2.34}$$

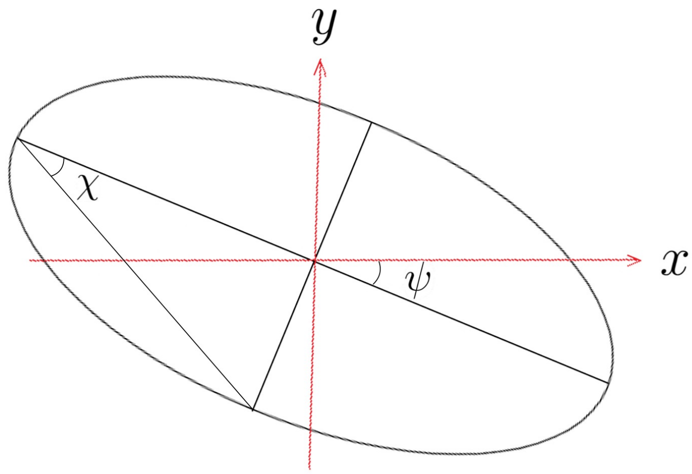

Figure 2.5: A figure of the polarization ellipse, where χ is the angle of ellipticity, and ψ is the angle of orientation.

each entry of the 2-vector is a complex-valued, time-independent component of the electric field E, where physical $\mathbf{E}$ field is just the real part of the complex vector.

We now write explicitly the six commonly used polarization states

$$\begin{aligned}
&\hat{\mathbf{h}} = \hat{\mathbf{x}} = \begin{bmatrix} 1 \\ 0 \end{bmatrix}, && \hat{\mathbf{v}} = \hat{\mathbf{y}} = \begin{bmatrix} 0 \\ 1 \end{bmatrix}, \\
&\hat{\mathbf{d}} = \frac{1}{\sqrt{2}}(\hat{\mathbf{h}} + \hat{\mathbf{v}}) = \frac{1}{\sqrt{2}} \begin{bmatrix} 1 \\ 1 \end{bmatrix}, && \hat{\mathbf{a}} = \frac{1}{\sqrt{2}}(\hat{\mathbf{h}} - \hat{\mathbf{v}}) = \frac{1}{\sqrt{2}} \begin{bmatrix} 1 \\ -1 \end{bmatrix}, \\
&\hat{\mathbf{l}} = \frac{1}{\sqrt{2}}(\hat{\mathbf{h}} + i\hat{\mathbf{v}}) = \frac{1}{\sqrt{2}} \begin{bmatrix} 1 \\ i \end{bmatrix}, && \hat{\mathbf{r}} = \frac{1}{\sqrt{2}}(\hat{\mathbf{h}} - i\hat{\mathbf{v}}) = \frac{1}{\sqrt{2}} \begin{bmatrix} 1 \\ -i \end{bmatrix},
\end{aligned} \tag{2.35}$$

We have explained the meanings of the variables χ and ψ, but this is not the only way to express these parameters, there are other interesting representations of them. In fact, another explicit way is to express these three parameters as [72, 69]

$$\begin{aligned}
S_1 &= |E_x|^2 - |E_y|^2, \\
S_2 &= |E_d|^2 - |E_a|^2, \\
S_3 &= |E_r|^2 - |E_l|^2,
\end{aligned} \tag{2.36}$$

In this notation, the subscripts indicate the components of the field in relevant polarization bases: the horizontal and vertical Cartesian basis, denoted by subscripts x and y; the diagonal and anti-diagonal basis (i.e., $\hat{\mathbf{x}}$ and $\hat{\mathbf{y}}$ rotated by

45°), denoted by d and a; and the left- and right-handed circular polarization basis, denoted by r and l. This representation clarifies the physical meaning of measuring the degree of polarization along each polarization direction. Since this representation requires only intensity measurements, the Stokes parameters are readily accessible through experimental observations.

Sometimes it is useful to write the Stokes parameters in the same basis, which brings us to another representation that can be obtained through a basis transformation of Eq. (2.36). We derive the representation in the horizontal and vertical Cartesian basis as an example.

In Eq. (2.36), S_1 is already expressed in horizontal and vertical Cartesian components. To derive the expression for S_2, we use the relations between the two Cartesian bases as

$$\begin{aligned}\hat{\mathbf{d}} &= \frac{1}{\sqrt{2}}\left(\hat{\mathbf{x}}+\hat{\mathbf{y}}\right),\\ \hat{\mathbf{a}} &= \frac{1}{\sqrt{2}}\left(\hat{\mathbf{x}}-\hat{\mathbf{y}}\right).\end{aligned} \tag{2.37}$$

where the hat indicates unit vectors. By expressing the $\mathbf{E}$ field in different bases, and substituting in the basis vector relations we can calculate

$$\begin{aligned}\mathbf{E} = E_x\hat{\mathbf{x}} + E_y\hat{\mathbf{y}} &= E_a\hat{\mathbf{a}} + E_d\hat{\mathbf{d}}\\ &= \frac{\sqrt{2}}{2}\left[E_a\left(\hat{\mathbf{x}}-\hat{\mathbf{y}}\right) + E_d\left(\hat{\mathbf{x}}+\hat{\mathbf{y}}\right)\right]\\ &= \frac{\sqrt{2}}{2}\left[\left(E_a+E_d\right)\hat{\mathbf{x}} + \left(-E_a+E_d\right)\hat{\mathbf{y}}\right].\end{aligned} \tag{2.38}$$

From the above calculation, we obtain:

$$E_d = \frac{\sqrt{2}}{2}\left(E_x+E_y\right),\ E_a = \frac{\sqrt{2}}{2}\left(E_x-E_y\right). \tag{2.39}$$

From which we can calculate S_2 as

$$\begin{aligned}S_2 &= \left|E_d\right|^2 - \left|E_a\right|^2\\ &= \frac{1}{2}\left(E_x+E_y\right)\cdot\left(E_x+E_y\right)^* - \frac{1}{2}\left(E_x-E_y\right)\left(E_x-E_y\right)^*\\ &= 2\mathrm{Re}\left(E_xE_y^*\right).\end{aligned} \tag{2.40}$$

Similarly, we can derive S_3 using the relations between $\hat{\mathbf{x}}, \hat{\mathbf{y}}$ and $\hat{\mathbf{r}}, \hat{\mathbf{l}}$, which are

$$\begin{aligned}\hat{\mathbf{r}} &= \frac{\sqrt{2}}{2}\left(\hat{\mathbf{x}}-i\hat{\mathbf{y}}\right),\\ \hat{\mathbf{l}} &= \frac{\sqrt{2}}{2}\left(\hat{\mathbf{x}}+i\hat{\mathbf{y}}\right).\end{aligned} \tag{2.41}$$

From which we obtain $S_3 = -2\mathrm{Im}\left(E_x E_y^*\right)$. This way, we express the four Stokes parameters all in the horizontal and vertical Cartesian basis as follows:

$$\begin{aligned} S_0 &= |E_x|^2 + |E_y|^2\,, \\ S_1 &= |E_x|^2 - |E_y|^2\,, \\ S_2 &= 2\mathrm{Re}\left(E_x E_y^*\right), \\ S_3 &= -2\mathrm{Im}\left(E_x E_y^*\right). \end{aligned} \tag{2.42}$$

We can apply the same reasoning to calculate the Stokes parameters for other bases. Starting from Eq. (2.36), if we express S_1 and S_3 in $\hat{\mathbf{d}}, \hat{\mathbf{a}}$ basis, and leave S_2 unchanged as it is already in $\hat{\mathbf{d}}, \hat{\mathbf{a}}$ basis, we obtain

$$\begin{aligned} S_0 &= |E_d|^2 + |E_a|^2\,, \\ S_1 &= -2\mathrm{Re}\left(E_d^* E_a\right), \\ S_2 &= |E_d|^2 - |E_a|^2\,, \\ S_3 &= 2\mathrm{Im}\left(E_d^* E_a\right). \end{aligned} \tag{2.43}$$

If we express S_1 and S_2 in $\hat{\mathbf{r}}, \hat{\mathbf{l}}$ basis, and leave S_3 unchanged as it is already in $\hat{\mathbf{r}}, \hat{\mathbf{l}}$ basis, we obtain

$$\begin{aligned} S_0 &= |E_l|^2 + |E_r|^2\,, \\ S_1 &= 2\mathrm{Re}\left(E_l^* E_r\right), \\ S_2 &= -2\mathrm{Im}\left(E_l^* E_r\right), \\ S_3 &= |E_r|^2 - |E_l|^2\,. \end{aligned} \tag{2.44}$$

Each group is a representation of Stokes parameters in a certain basis, as indicated by their subscripts.

Although it may not be immediately obvious, in the above representations, an eigenvalue expression is associated with one of the Stokes parameters in each group. In each basis, the Stokes parameters can be interpreted as expectation values of the Pauli matrices [74], which form a complete set of observables for the polarization state of light. These matrices act on the polarization state represented by a Jones vector. Specifically, the normalized Stokes vector $\mathbf{S} = (S_1, S_2, S_3)$ can be written as the expectation values of the Pauli matrices:

$$S_i = \langle\psi|\sigma_i|\psi\rangle, \quad i = 1, 2, 3 \tag{2.45}$$

where $|\psi\rangle$ is the normalized Jones vector of the light field, and σ_i are the Pauli matrices. This expression resembles an eigenvalue equation, in the sense that if the polarization state is an eigenvector of a Pauli matrix (e.g., horizontal, diagonal, circular), then the corresponding Stokes parameter reaches its maximum or minimum value of ± 1.

Thus, each basis corresponds to an eigenbasis of one of the Pauli matrices. The shift in the form of the Stokes parameters across different bases reflects this underlying eigenvalue structure: the beam is being *measured* in different polarization observables depending on the chosen basis.

The connection between the Stokes parameters and the Pauli matrices allows us to adopt representations from quantum mechanics, such as bra-ket notation and operators. These applications will be discussed in more detail in chapter 4, chapter 5, and chapter 6.

2.5.2 The Poincaré Sphere

Aside from polarization ellipse, another model that links closely to the geometry of Stokes parameters is the Poincaré sphere. Poincaré's work is a continuation of Stokes construction. In 1892, he proposed a spherical representation for polarized light, later became known as the Poincaré sphere [75]. We remark here that it is again intrinsically the same thing as Bloch sphere, which has been proposed later to deal with pure states in quantum systems [76]. The repeated déjà vu feeling is due to the analogies between optical systems and two-dimensional quantum systems; both are 2-level systems, and one can also link full and partial polarizations with pure and mixed states.

The expression of Stokes parameters in terms of angles χ and ψ in Eq. (2.33) already exhibited this geometry, as one can immediately recognize the expression has the form of spherical coordinates, and think of $[S_1, S_2, S_3]$ as the representation of a vector on the surface of a sphere with radius S_0. If we normalize all the components to $\left[\hat{S}_1, \hat{S}_2, \hat{S}_3\right]$, where $\hat{S}_1 = S_1/S_0$, and similarly for $\hat{S}_2$ and $\hat{S}_3$, we get a nomalized Stokes vector, which we call $\mathbf{S}$. The Poincaré sphere is a unit sphere where $\mathbf{S}$ lives.

In our context we are always using the normalized Stokes parameters, for convenience we will drop the hat on components in later context.

The Poincaré sphere represents polarizations in the following way: polarization ellipses with same shape, or same ellipticity, all dwell in the same latitude, while along a latitudinal line their orientation changes. On the equator of the Poincaré sphere, the polarizations are linear, evolving from horizontal linear polarization (along positive direction of S_1) to anti-diagonal, vertical, and eventually back to horizontal linear polarization. Along the longitudinal line, the polarization starts as a right-handed circular polarization on the North pole, evolves to a linear polarization on the equator line, and with the inverse process back to circular polarization on the southern hemisphere, but with an opposite handedness, ended as a left-handed polarization on the South pole. Antipodal points on the Poincaré sphere represents orthogonal polarizations. These properties are shown in Figure. 2.6.

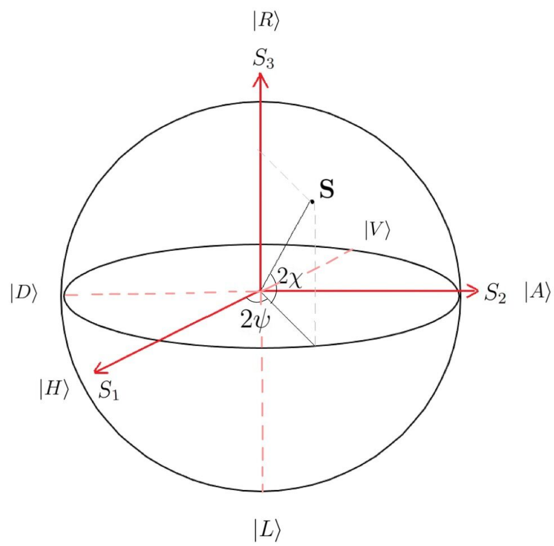

Figure 2.6: Figure of a Poincaré Sphere, with the spherical angles (χ, ψ) describe ellipticity and orientation, respectively. Orthogonal polarization states are represented by antipodal points on the Poincaré Sphere. The vector $\mathbf{S}$ is a unit vector whose tip lies on the surface of the Poincaré sphere, representing a fully polarized beam.

2.6 Strong Focusing System

In modern optics, many of the most important problems use optical techniques that involve highly focused higher order laser modes to access the longitudinal components of the fields [77, 78]. Recall in the paraxial treatment (introduced in section 2.3), we have omitted the transverse component of the field, which therefore becomes insufficient in these occasions [79]. By the term strong focusing, we are referring to systems with high numerical aperture (NA>1), the definition of which will be given later in this section.

In this section, we will introduce Richards and Wolf's method [41] of dealing with strong focusing optical system. We will mostly follow chapter 3 of *Principle of Nano Optics* [39], with some derived details which are not included in the book, as well as corrections and some re-construction.

2.6.1 Far Field Approximation

We have introduced the angular spectrum representation in subsection 2.3.1, which is where we start from. Recall Eq. (2.9), which describes the relation between a propagating $\mathbf{E}$ field and the spectrum in the object plane, as

$$\mathbf{E}(x, y, z) = \iint_{-\infty}^{\infty} \hat{\mathbf{E}}\left(k_x, k_y; 0\right) \mathrm{e}^{i[k_x x + k_y y + k_z z]} \mathrm{d}k_x \mathrm{d}k_y. \tag{2.46}$$

This is the result of the Fourier transform, where we have written a general Fourier spectrum in terms of the spectrum at the object plane ($z = 0$) and a propagator ($\mathrm{e}^{\pm i k_z z}$). Here we always assume the propagation direction to be $+z$, so that the exponential form of the propagator always takes the $+$ sign. So, we can calculate the spectrum at any arbitrary image plane ($z = constant$) in terms of the spectrum at the object plane.

Consider here a far-field approximation, where the field we want to evaluate is at an infinite distance from the object plane [80]. This way, the evanescent waves, which are waves that decay exponentially with distances, do not contribute. By the stationary phase method, which provides an asymptotic approximation to integrals for large values of an appropriate parameter [81], we understand that the far-fields are entirely defined by the spectrum field at the object plane $\hat{\mathbf{E}}\left(k_x, k_y; 0\right)$. This indicates that, in the direction $\mathbf{s} = \left(\frac{x}{r}, \frac{y}{r}, \frac{z}{r}\right)$, the far field can be expressed as

$$\mathbf{E}_{\infty}\left(s_x, s_y\right) = -2\pi i k s_z \hat{\mathbf{E}}\left(k s_x, k s_y; 0\right) \frac{\mathrm{e}^{ikr}}{r}, \tag{2.47}$$

or, in terms of (k_x, k_y, k_z),

$$\mathbf{E}_{\infty}\left(\frac{k_x}{k}, \frac{k_y}{k}\right) = -2\pi i k_z \hat{\mathbf{E}}\left(k_x, k_y\ ; 0\right) \frac{\mathrm{e}^{ikr}}{r}, \tag{2.48}$$

where $r = (x^2 + y^2 + z^2)^{1/2}$.

This tells us that the only plane wave that contributes to the far field at direction $\mathbf{s} = \left(\frac{k_x}{k}, \frac{k_y}{k}, \frac{k_z}{k}\right)$ is the plane wave with wavevector $\mathbf{k} = (k_x, k_y, k_z)$. Contributions from all other plane waves all cancel out due to destructive interference.

By inverting the relation in Eq. (2.48), and substitute into Eq. (2.46), we get a relation between field $\mathbf{E}$ and its far field

$$\mathbf{E}(x, y, z) = \frac{ir\mathrm{e}^{-ikr}}{2\pi} \iint_{\left(k_x^2+k_y^2 \leq k^2\right)} \frac{1}{k_z} \mathbf{E}_\infty \left(\frac{k_x}{k}, \frac{k_y}{k}\right) \mathrm{e}^{i[k_x x + k_y y + k_z z]} \mathrm{d}k_x \mathrm{d}k_y, \quad (2.49)$$

where we have indicated the integration range because the evanescent waves do not contribute [80, 39]. We now obtain a relation between the two fields, where we find that at $z = 0$ and $k_z \approx k$, we have field $\mathbf{E}$ and its far field from essentially a Fourier pair, which is the limit of Fourier Optics [39, 52].

2.6.2 Aplanatic System

We now introduce the strong focusing system, which plays a key roll in confocal microscopy systems and data storage [82], also optical tweezers, the single-beam gradiant trap, which have vital applications in measuring the mechanical property of cells [83]. Consider an aplantic system which focus the paraxial beams, as shown in Figure. 2.7. We define the focal length to be f, which is the distance between the optical lens and the focal plane. θ is the angle between the refracted beam and the incident beam, and h is the distance between the parallel incident beam and the optical axis.

We want to characterize a polarized incident beam after passing through the system. Here, two approximations will be applied, namely, the sine condition and the intensity law [39]. The sine condition applies geometrical optics theory to the incident light beam and the refracted light beam, and the intensity condition states that a ray will always carry the same amount of energy before and after the refraction.

In an ideal model, where no aberrations occur, rays from a point object traveling through the aplanatic system will traverse the same optical path length and converge perfectly at the Gaussian image point. The optical path length of a ray is defined as the refractive index n multiplied by the geometrical path length [84]. Geometrical optics tells us that the refracted rays will bend on a reference sphere with radius f, intersecting with their conjugate rays. This sphere is known as the Gaussian (reference) sphere, with its center located at the Gaussian image point. The geometrical relations are illustrated in Figure 2.7.

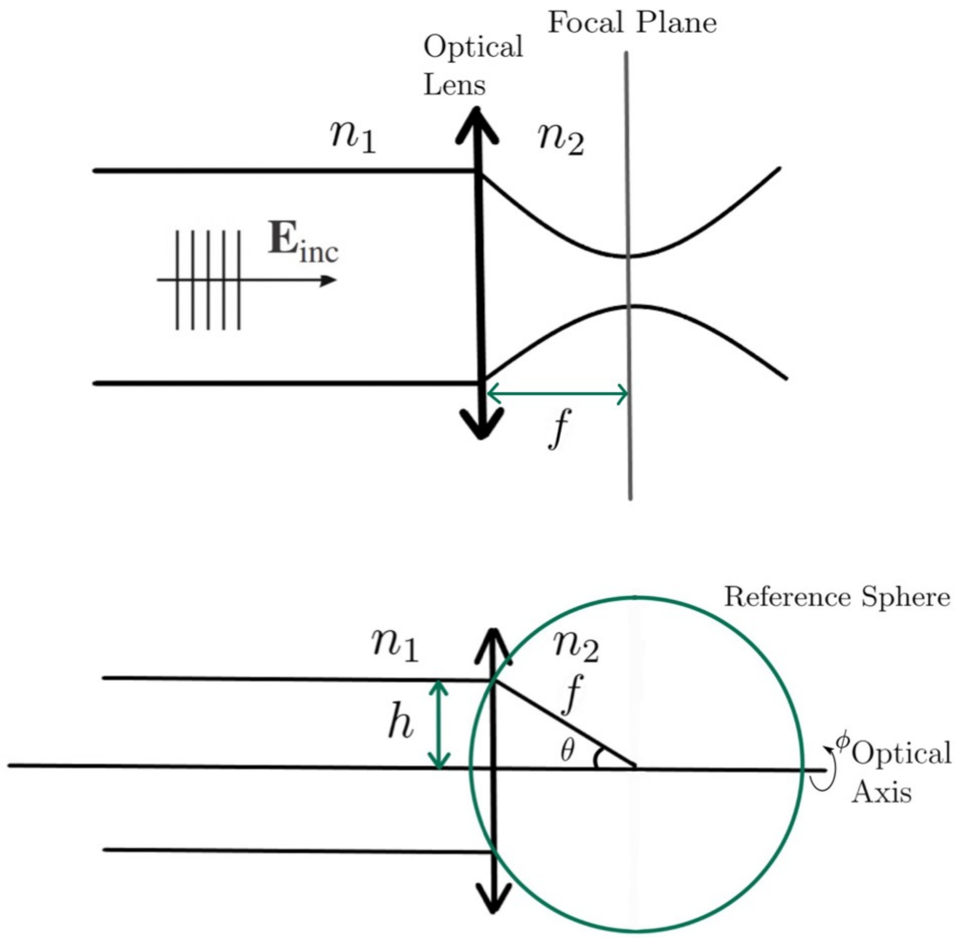

Figure 2.7: Figure of an aplanatic system, with different dielectric media on each side of the lens. Other relevant parameters are defined in the figure. The lower part of the figure shows a reference sphere of radius f, which is equal to the focal length. An incident ray which is parallel to the optical axis will intersect the refracted ray on the reference sphere.

A point (x, y, z) on the reference sphere can be represented by the spherical coordinates as

$$\begin{aligned} x &= f \sin\theta \cos\phi, \\ y &= f \sin\theta \sin\phi, \end{aligned} \tag{2.50}$$

where θ and ϕ are the polar and azimuthal angles, respectively, as shown in Figure. 2.7.

With the above analyses of the two approximations, we have the two mathematical relations

$$\begin{aligned} h =& f \sin\theta, \\ |\mathbf{E}_{\text{ref}}| = |\mathbf{E}_{\text{inc}}| & \sqrt{\frac{n_1}{n_2}}\sqrt{\frac{\mu_2}{\mu_1}} (\cos\theta)^{\frac{1}{2}}, \end{aligned} \tag{2.51}$$

where $\mathbf{E}_{\text{ref}}$ refers to the refracted field and $\mathbf{E}_{\text{inc}}$ refers to the incident field, the term $(\cos\theta)^{\frac{1}{2}}$ arises from the geometrical relation of the basis transformation. μ_1 and μ_2 are magnetic permeabilities of the respective media, which typically take the value of 1 at optical frequencies, as the magnetization of natural materials is unable to follow the variation of the magnetic field of light [85]. So, the term $\frac{\mu_2}{\mu_1}$ will be discarded in the following context. Another thing to notice is that the above approximations of the aplanatic system are only suitable for paraxial beams [39, 84, 3], the beam after focusing of course, is no longer paraxial.

Another thing to notice is that any polarized plane wave can be written as a superposition of two orthogonal polarizations, namely s-polarization and p-polarization, where s-polarization is parallel to the interface and p-polarization is perpendicular to $\mathbf{E}$ and $\mathbf{k}$, as shown in Figure 2.8. Their reflections and transmissions are governed by Fresnel coefficients, which we denote by r^s, r^p, t^{s}, t^{p} [3, 39]. This means that, by separating $\mathbf{E}_{\text{inc}}$ to s- and p- polarized parts and treat them separately according to their own refractive law, we have the relation in cylindrical coordinates as

$$\begin{aligned} \mathbf{E}_{\text{inc}} &= \mathbf{E}_{\text{inc}}^{\text{s}} + \mathbf{E}_{\text{inc}}^{\text{p}} \\ &= [\mathbf{E}_{\text{inc}} \cdot \mathbf{n}_\phi]\, \mathbf{n}_\phi + [\mathbf{E}_{\text{inc}} \cdot \mathbf{n}_\rho]\, \mathbf{n}_\rho. \end{aligned} \tag{2.52}$$

The geometrical structure of the aplanatic system indicates that we transit from a cylindrical coordinate system to a spherical one before and after focusing. We see that the vector in polar direction $(\mathbf{n}_\phi)$ in the two systems remains unchanged, while the vector in the radial direction $\mathbf{n}_\rho$ is mapped to the azimuthal direction $\mathbf{n}_\theta$, as shown in Figure. 2.9.

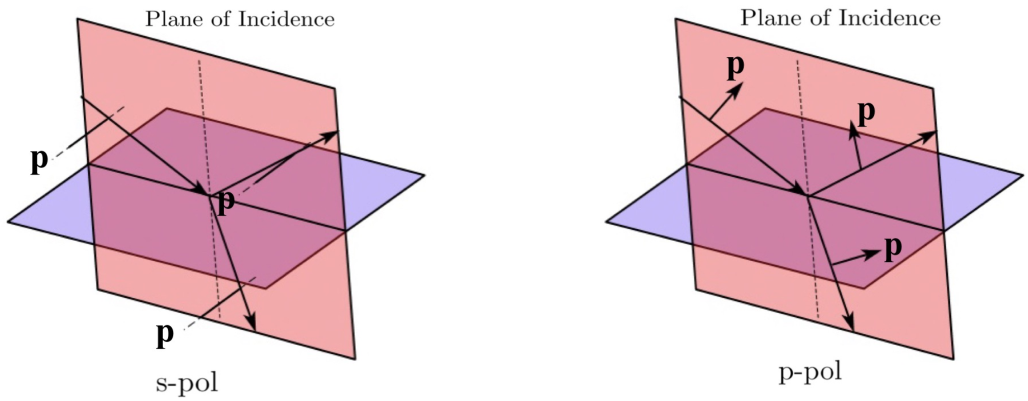

Figure 2.8: Figure showing the s- and p-polarizations, where **p** represents the polarization direction, red plane is the plane of incidence, and blue plane is the interface where the refractive happens.

Therefore, the total refracted field can be written as

$$\begin{aligned}\mathbf{E}_{\text{ref}} &= \mathbf{E}_{\text{ref}}^{\text{s}} + \mathbf{E}_{\text{ref}}^{\text{p}} \\ &= t^{\text{s}}\mathbf{E}_{\text{inc}}^{\text{s}}\sqrt{\frac{n_1}{n_2}}\,(\cos\theta)^{\frac{1}{2}} + t^{\text{p}}\mathbf{E}_{\text{inc}}^{\text{p}}\sqrt{\frac{n_1}{n_2}}(\cos\theta)^{1/2} \\ &= \left[t^{\text{s}}\left(\mathbf{E}_{\text{inc}}\cdot\mathbf{n}_\phi\right)\mathbf{n}_\phi + t^{\text{p}}\left(\mathbf{E}_{\text{inc}}\cdot\mathbf{n}_\rho\right)\mathbf{n}_\theta\right]\sqrt{\frac{n_1}{n_2}}(\cos\theta)^{1/2},\end{aligned} \tag{2.53}$$

in the second line, we have substituted the relation between the incident beam and the refracted beam (Eq. (2.51)), and in the third line, we refract the s- and p- polarized components differently (Eq. (2.52)).

The refracted field is the field on the reference sphere, and can be treated as a far field and denoted as $\mathbf{E}_\infty$. This is because to use the assumption of a far field, we must satisfy two conditions: 1. $kr \to \infty$ and 2. evanescent waves must be dicarded. This means in order to use the far field formula Eq. (2.49) we do not need an actual far field, but any field that satisfies the above conditions. So, as long as we have large k, we do not need r to reach out to infinity. By large k, we mean that the finiteness of the optical wavelength can be neglected, or that the wavelength is small compared to the focal length, which is usually the case for visible light.

We can express all the unit vectors in the refracted field as column vectors,

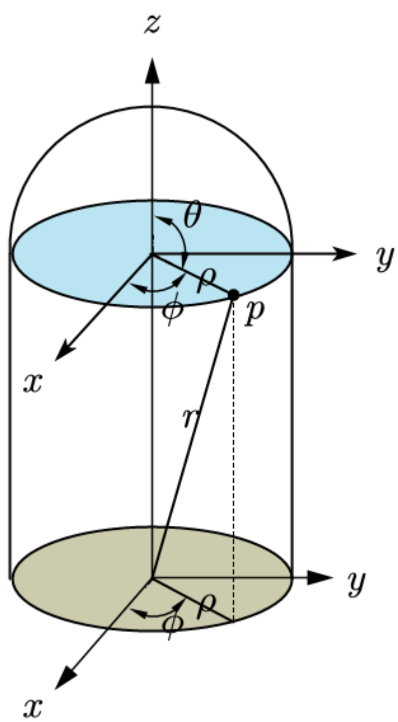

Figure 2.9: The relations between coordinates of ρ in cylindrical and spherical systems.

and express the far field of the refracted field as

$$\begin{aligned}\mathbf{E}_{\infty}(\theta,\phi) = &\left[\mathbf{E}_{\text{inc}}(\theta,\phi)\cdot\begin{pmatrix}-\sin\phi\\ \cos\phi\\ 0\end{pmatrix}\right]\begin{pmatrix}-\sin\phi\\ \cos\phi\\ 0\end{pmatrix}\sqrt{\frac{n_1}{n_2}}(\cos\theta)^{1/2}+\\ &\left[\mathbf{E}_{\text{inc}}(\theta,\phi)\cdot\begin{pmatrix}\cos\phi\\ \sin\phi\\ 0\end{pmatrix}\right]\begin{pmatrix}\cos\phi\cos\theta\\ \sin\phi\cos\theta\\ -\sin\theta\end{pmatrix}\sqrt{\frac{n_1}{n_2}}(\cos\theta)^{1/2}.\end{aligned} \tag{2.54}$$

where we have assumed a good antireflection coating, such that t^s and t^p can be taken to be 1.

Therefore, Eq. (2.54) calculates the refracted field for any incident beam that passes through the aplanatic system.

Chapter 3

Faraday Effect for Focused Vector Vortex Beams

3.1 Introduction

Magneto-optical effects describe how magnetic fields influence the interaction between light and matter, modifying either the properties of the medium or the light [86, 87, 88]. There are many such effects, such as the Faraday effect, the Kerr effect, and the Voigt effect [89].

In 1845, Michael Faraday discovered that the polarization plane of light rotates as it propagates through a material in the presence of a magnetic field aligned with the direction of propagation (Figure. 3.1). It was the first experimental evidence revealing the relationship between light and electromagnetism [18, 90, 91]. Later, in 1876, John Kerr discovered another effect that involves the interaction of the electric field of light with the magnetization of the material, known as the Kerr effect [92]. This effect typically occurs upon reflection from a magnetized surface, unlike the Faraday effect, which occurs during transmission. In 1898, Woldemar Voigt introduced the Voigt effect, a quadratic, reciprocal counterpart to the Faraday effect [89]. The Voigt effect manifests as magnetically induced birefringence due to a transverse magnetic field and is even under field reversal [93]. Among the earliest and most widely studied of these is the Faraday effect, which not only revealed a fundamental link between light and electromagnetism but also laid the foundation for modern magneto-optics.

The Faraday effect remains a cornerstone of magneto-optical research due to its ubiquity across various media and wide-ranging applications in optical isolators, magneto-optical imaging, and quantum optics [94, 95, 96]. It also exhibits unique characteristics, such as non-reciprocity and the ability to interact with the spin angular momentum of light [97, 98]. These features make it especially ap-

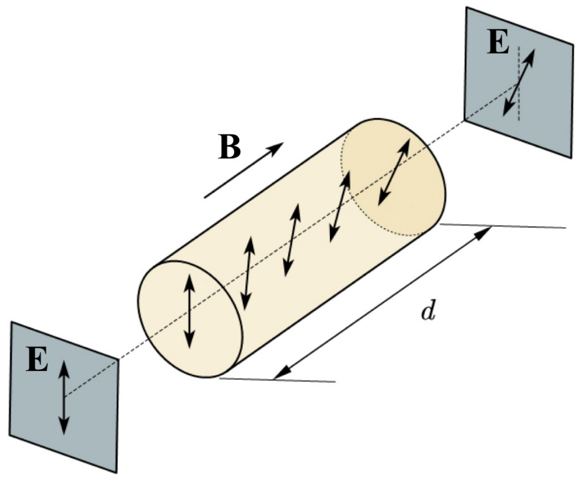

Figure 3.1: A schematic of the linear Faraday effect illustrates the influence of a magnetic field applied along the propagation direction of a dielectric medium. The magnetic field is aligned with the optical axis, and as a linearly polarized light beam passes through the medium, its polarization direction rotates.

pealing for studies involving structured light, such as vector vortex beams, which carry spatially varying polarization and orbital angular momentum.

Recently, the importance of strong focusing has grown significantly, particularly in the context of nanophotonics and structured materials. With the rise of metasurfaces, plasmonic nanostructures, and other sub-wavelength objects, many optical experiments require the use of tightly focused beams to interact with features at the nanoscale [99]. However, tight focusing introduces non-paraxial effects that fundamentally alter the beam's polarization distribution, including the emergence of longitudinal field components and spatially varying polarization [39, 100, 101]. These polarization changes are particularly relevant in magneto-optical studies: if not considered, they can lead to misinterpretation of the Faraday rotation or magneto-optical signals. For example, structured beams can acquire spin-orbit coupling effects under strong focusing, modifying how light interacts with magnetization in a sample [102].

Thus, a refined understanding of the Faraday effect under strong focusing is not only of fundamental interest but also crucial for correctly interpreting and designing experiments involving nanoscale magneto-optical systems. When vector vortex beams are tightly focused, their complex internal structure interacts non-trivially with material anisotropies and external fields. For such structured beams, the depiction and analysis of the Faraday effect on a linearly polarized light becomes insufficient. For later convenience, we refer to the Faraday effect which rotates linearly polarized light as the *linear Faraday effect*, and the more subtle rotation arising from the unique properties of vector vortex beams will be termed the *secondary Faraday effect*.

This chapter investigates the magnetic Faraday effect and how focused vector vortex beams reveal new aspects of this classic phenomenon. We start with a paraxial vector vortex beam, where the effect is relatively simple and dominated by the linear Faraday rotation (section 3.2). We then analytically demonstrate in section 3.3 how a secondary Faraday effect arises in a radially polarized beam (RPB). In subsection 3.3.1, simulation results show that while a paraxial RPB experiences inhomogeneous polarization rotation in a Faraday medium, the effect is typically weak and overshadowed by the linear rotation. In section 3.4, we show that strongly focusing the RPB magnifies the inhomogeneous rotation, making it comparable to the linear Faraday effect. This also induces a radially varying polarization pattern, as demonstrated in section 3.5. We further discuss the oblique incidence case in section 3.6, where both the Voigt and Faraday effects contribute simultaneously. This scenario introduces new complexity and is a direction for future research. An eigenmode solution for the combined effect is provided, and the chapter concludes in section 3.7.

In this chapter, I am responsible for the whole thoery part, and the experiment was carried out by Sphinx. Svensson under the guidance of Prof. Sonja Franke-Arnold.

3.2 Faraday Effect for Linearly Polarized Beam

We begin with a brief analysis of the linear Faraday effect for linearly polarized light. As stated in the introduction, a linearly polarized beam would experience a rotation of its polarization direction due to the applied magnetic field. The reason behind this is clear: linearly polarized light can be decomposed into two circularly polarized components, with equal amplitude profiles but orthogonal polarization directions, as

$$\begin{aligned}\mathbf{p} &= \cos\theta\mathbf{e}_x + \sin\theta\mathbf{e}_y \\ &= \frac{1}{\sqrt{2}}\cos\theta\left(\mathbf{e}_R + \mathbf{e}_L\right) - \frac{i}{\sqrt{2}}\sin\theta\left(\mathbf{e}_L - \mathbf{e}_R\right) \\ &= \frac{1}{\sqrt{2}}\left(\cos\theta + i\sin\theta\right)\mathbf{e}_R + \frac{1}{\sqrt{2}}\left(\cos\theta - i\sin\theta\right)\mathbf{e}_L \\ &= \frac{1}{\sqrt{2}}\left(\exp\left(i\theta\right)\mathbf{e}_R + \exp\left(-i\theta\right)\mathbf{e}_L\right)\end{aligned} \tag{3.1}$$

where $\mathbf{p}$ represents a linear polarization at an arbitrary angle θ to the x-axis, and $\mathbf{e}_x$, $\mathbf{e}_y$, $\mathbf{e}_R$ and $\mathbf{e}_L$ stand for different polarizations as indicated by their subscripts. It is not difficult to see that when the two circularly polarized components experience different refractive indices, a beam $\mathbf{E}$ would evolve along its propagation direction as

$$\begin{aligned}
\mathbf{E} =& \frac{1}{\sqrt{2}}\left(e^{i\theta}e^{ik_0 n_R z}\boldsymbol{e}_R + e^{-i\theta}e^{ik_0 n_L z}\boldsymbol{e}_L\right)\\
=& \frac{1}{\sqrt{2}}e^{ik_0(n_R+n_L)z/2}\left(e^{i\theta}e^{ik_0(n_R-n_L)z/2}\boldsymbol{e}_R + e^{-i\theta}e^{-ik_0(n_R-n_L)z/2}\boldsymbol{e}_L\right)\\
=& \frac{1}{\sqrt{2}}e^{ik_0\frac{(n_R+n_L)}{2}z}\left(e^{i(\theta+\Delta\theta)}\boldsymbol{e}_R + e^{-i(\theta+\Delta\theta)}\boldsymbol{e}_L\right)\\
=& e^{ik_0(n_R+n_L)z/2}\left(\cos\left(\theta+\Delta\theta\right)\boldsymbol{e}_x + \sin\left(\theta+\Delta\theta\right)\boldsymbol{e}_y\right),
\end{aligned} \tag{3.2}$$

where $\Delta\theta = k_0(n_R - n_L)z/2$ is the angle rotated as the beam propagates along $\mathbf{z}$, n_R and n_L represents different refractive indices for left and right circularly polarized beam. In general, the refractive index can be complex, i.e., $n_{R,L} = n'_{R,L} + in''_{R,L}$, where the real parts $n'_{R,L}$ are responsible for phase differences between circular polarization components, while the imaginary parts $n''_{R,L}$ describe absorption, or circular dichroism (see chapter 5 of [88]). In what follows, we focus on the Faraday effect arising from birefringence, and for simplicity denote the refractive indices by n_R and n_L.

When the beam propagates in the dielectric medium in the presence of a magnetic field, its two circularly polarized components propagate with different speeds due to slightly different refractive indices, thus a (constant) phase difference will be introduced to the propagation term, which accumulates to cause the rotation. This is just like the birefringence nature of certain materials. With the presence of the magnetic field, the dielectric medium exhibits this birefringence property, and becomes a Faraday medium which causes the rotation.

We now calculate the rotation of a linearly polarized beam within a Rayleigh range, z_R, as an example, due to its physical significance as the effective path length over which the beam maintains its focus. As calculated above, the rotation angle is given by

$$\Delta\theta = k_0(n_R - n_L)z/2 = \pi(n_R - n_L)z/\lambda, \tag{3.3}$$

where λ is the wavelength. So the rotation angle of the length of Rayleigh range can be represented as

$$\Delta\theta_R = \frac{\pi\left(n_L - n_R\right)}{\lambda}\cdot z_R = \frac{\pi^2 w_0^2\left(n_L - n_R\right)}{\lambda^2}. \tag{3.4}$$

3.3 Faraday Effect for Paraxial Vector Vortex Beams

We want to investigate the Faraday effect for more intricate structured light beams, and we start with a paraxial vector vortex beam. A radially polarized beam has been chosen for this purpose, which can be created using the superposition of two Hermite Gaussian (HG) modes encoded with orthogonal linear polarization components or two Laguerre Gaussian (LG) modes encoded with orthogonal circular polarizations. Specifically, we have

$$|\psi\rangle = \frac{1}{\sqrt{2}}\left(\mathrm{LG}_0^1|\hat{r}\rangle + \mathrm{LG}_0^{-1}|\hat{l}\rangle\right) = \frac{1}{\sqrt{2}}\left(\mathrm{HG}_{10}|\hat{h}\rangle + \mathrm{HG}_{01}|\hat{v}\rangle\right) \tag{3.5}$$

where $|\psi\rangle$ represents a radially polarized beam, as shown in Figure 3.2.

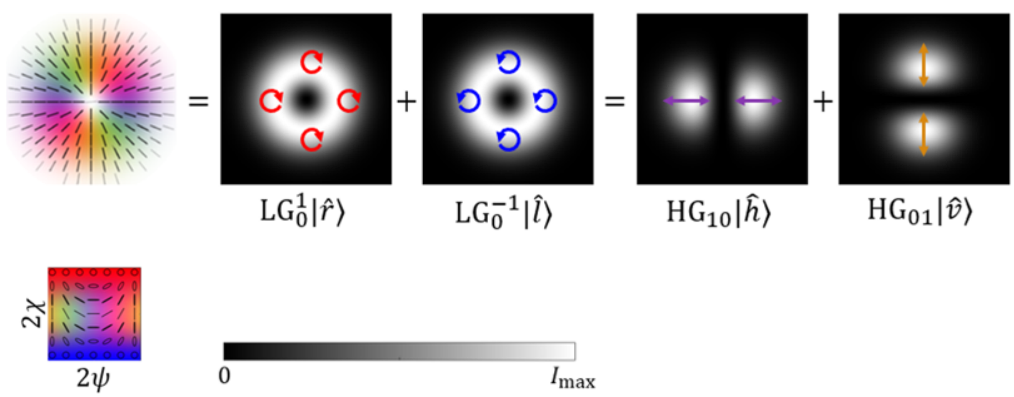

Figure 3.2: Radially polarized beam composed from LG beams and HG beams, respectively.

As the Faraday effect is associated with circular birefringence, it can most easily be analyzed for circularly polarized components, thus we choose to decompose the radially polarized beam into LG modes, corresponding to the first expression in Eq. (3.5).

We have introduced LG beams in subsection 2.3.2, where a general form of LG beams has been given in Eq. (2.23). It is well known that LG beams are a class of solutions to the paraxial wave equation. In section 2.3 we have explained how the approximations are made, which allows us to reduce the more general wave equation Eq. (2.3) to the paraxial wave equation Eq. (2.6). The solutions to the time-independent wave equation, i.e. the Helmholtz equation, are further written in the form of $U_0(r,z,t) = E(r,z)\,e^{ikz}$ in this process. This means that the solutions to the paraxial wave equation do not contain the propagating term e^{ikz} (or equivalently e^{ik_0nz}, where n is the refractive index). For our purpose of exploring the Faraday effect, however, we must take this propagation term into account. This means we should add the propagation term to Eq. (2.23), and obtain the general form of propagating LG beams as

$$\begin{aligned}\mathrm{LG}_p^l\left(r,\phi,z\right)=&\sqrt{\frac{2p!}{\pi\left(p+|l|!\right)}}\,\frac{1}{w\left(z\right)}\,\left(\frac{\sqrt{2}r}{w\left(z\right)}\right)^{|l|}L_p^{|l|}\left(\frac{2r^2}{w\left(z\right)^2}\right)\cdot\\&e^{-\frac{r^2}{w(z)^2}}\,e^{i\left(l\phi+\frac{kr^2}{2R(z)}-(2p+|l|+1)\varphi_g\right)}\,e^{ik_0nz},\end{aligned}\tag{3.6}$$

where l is the winding number which characterizes the phase singularities, p is the radial angular momentum number, and $L_p^{|l|}$ are the associated Laguerre polynomials.

We will now analyze the secondary Faraday effect for a radially polarized beam (RPB). Using its decomposition in terms of right and left circular polarisation from Eq. (3.5) we substitute the relevant indices $|l|=1$, $p=0$, $n=n_R$ or $n=n_L$ into Eq. (3.6) to obtain the desired beam profiles. We know from the linear Faraday effect that the refractive indices would be slightly different for left- and right-handed polarizations, meaning that the beam radius $w(z)$, wavefront radius $R(z)$, Gouy phase φ_g and Rayleigh range z_R which depend on the refractive indices will all be affected. Therefore, we assign subscripts R and L to these variables to distinguish their values for right and left circular polarization, respectively. We can write the RPB as

$$\begin{aligned}\mathrm{RPB}=&\sqrt{\frac{2}{\pi}}\,\frac{1}{w_R\left(z\right)}\,\left(\frac{\sqrt{2}r}{w_R\left(z\right)}\right)\cdot e^{-\frac{r^2}{w_R(z)^2}}\,e^{i\left[\phi+\frac{kr^2}{2R_R(z)}-2\varphi_{gR}\right]}\,e^{ik_0n_Rz}\boldsymbol{e}_R+\\&\sqrt{\frac{2}{\pi}}\frac{1}{w_L\left(z\right)}\,\left(\frac{\sqrt{2}r}{w_L\left(z\right)}\right)\cdot e^{-\frac{r^2}{w_L(z)^2}}e^{i\left[-\phi+\frac{kr^2}{2R_L(z)}-2\varphi_{gL}\right]}\,e^{ik_0n_Lz}\boldsymbol{e}_L,\end{aligned}\tag{3.7}$$

where we have used the property of associated Laguerre polynomial that $L_0^1=1$.

It is the phase difference between the LHP and RHP that accumulates to cause the rotation we are interested in. Therefore, we can ignore the intensity profiles for our purpose. For the phase terms, we can apply the same method used in Eq. (3.2). We first write the phase-related terms of the **E** field of the radially polarized beam, represented by $\mathbf{\Phi}_{\mathrm{RPB}}$, as

$$
\begin{aligned}
\mathbf{\Phi}_{\mathrm{RPB}} =& e^{i\left[\phi+\frac{kr^2}{2R_R(z)}-2\varphi_{gR}\right]}e^{ik_0n_Rz}\boldsymbol{e}_R + e^{i\left[-\phi+\frac{kr^2}{2R_L(z)}-2\varphi_{gL}\right]}e^{ik_0n_Lz}\boldsymbol{e}_L \\
=& e^{i\phi}e^{i\phi_R}e^{ik_0n_Rz}\boldsymbol{e}_R + e^{-i\phi}e^{i\phi_L}e^{ik_0n_Lz}\boldsymbol{e}_L \\
=& e^{i[(\phi_R+k_0n_Rz)+(\phi_L+k_0n_Lz)]/2}\cdot \\
& \left[e^{i\phi}\cdot e^{i[(\phi_R+k_0n_Rz)-(\phi_L+k_0n_Lz)]/2}\boldsymbol{e}_R + e^{-i\phi}\cdot e^{i[-(\phi_R+k_0n_Rz)+(\phi_L+k_0n_Lz)]/2}\boldsymbol{e}_L\right] \\
=& e^{i[(\phi_R+k_0n_Rz)+(\phi_L+k_0n_Lz)]/2}\cdot\left[e^{i(\phi+\Delta\phi)}\boldsymbol{e}_R + e^{-i(\phi+\Delta\phi)}\boldsymbol{e}_L\right] \\
=& \sqrt{2}e^{i[(\phi_R+k_0n_Rz)+(\phi_L+k_0n_Lz)]/2}\left[\cos\left(\phi+\Delta\phi\right)\boldsymbol{e}_x + \sin\left(\phi+\Delta\phi\right)\boldsymbol{e}_y\right],
\end{aligned}
\tag{3.8}
$$

where we have set $\phi_L = \frac{kr^2}{2R_L(z)} - 2\varphi_{gL}$ and $\phi_R = \frac{kr^2}{2R_R(z)} - 2\varphi_{gR}$. We see that the linear polarization of the initial RPB is rotated by an angle

$$
\Delta\phi = \frac{(\phi_R + k_0n_Rz) - (\phi_L + k_0n_Lz)}{2}. \tag{3.9}
$$

This angle has the form similar to the rotation angle $\Delta\theta$ we obtained in section 3.2 for linear polarized light, with a slightly more complicated structure that contributes to a secondary rotation, which we write out explicitly as

$$
\begin{aligned}
\Delta\phi =& \frac{(\phi_R + k_0n_Rz) - (\phi_L + k_0n_Lz)}{2} \\
=& \frac{k_0\left(n_R-n_L\right)z}{2} + \frac{1}{2}\left[\left(\frac{kr^2}{2R_R\left(z\right)} - 2\varphi_{gR}\right) - \left(\frac{kr^2}{2R_L\left(z\right)} - 2\varphi_{gL}\right)\right].
\end{aligned}
\tag{3.10}
$$

If we compare the $\Delta\phi$ we rearranged here with the $\Delta\theta$ we obtained in Eq. (3.2), we recognize that the first term is the rotation due to the linear Faraday effect which exists in linearly polarized beam, as we discussed before. The second term is a rotation due to what we call a *secondary Faraday effect*, and it is the consequence of the structure of the LG beams.

With further rearrangements, we can write out the rotation term due to the secondary Faraday effect which we represent as $\Delta\phi_{2nd}$, as

$$
\Delta\phi_{2nd} = \frac{kr^2}{4}\left(\frac{1}{z+\frac{z_{R_R}^2}{z}} - \frac{1}{z+\frac{z_{R_L}^2}{z}}\right) + \left(-\arctan\frac{z}{z_{R_R}} + \arctan\frac{z}{z_{R_L}}\right), \tag{3.11}
$$

where we have used $R_{R,L}(z) = z\left(1+\frac{z_{R_{R,L}}^2}{z^2}\right)$. The first term of the rotational angle arises from the Rayleigh range difference between the RHP and LHP components, while the second term is due to their Gouy phase difference.

From Eq. (3.11), we observe that the secondary Faraday effect depends on two variables, r and z, where r is the radial distance from the optical axis and z is the propagation distance. This implies that the rotation angle will vary as the beam propagates, and for any fixed propagation distance will change as a function of r. One may assume the natural way of analyzing this variation is to take partial derivatives with respect to each variables. However, the partial derivatives do not yield sensible results as the dependence on the variables cannot be separated neatly.

At this stage, we are unable to proceed analytically without further assumptions, and will instead tackle the problem numerically. We assign specific values to the refractive indices for the two beam components. We set $n_R = 1.45$ and $n_L = 1.55$, these values are realistic and can be achieved in experiments. Additionally, we assign plausible values to the wavelength and other relevant beam parameters. We set $\lambda = 520$ nm, therefore $k \approx 1.209 * 10^{-7}$ m^{-1}, and the beam waist to be 1 mm. From these values we can calculate the Rayleigh ranges for left-handed and right-handed polarization to be $z_{R_L} = 9.36$ m and $z_{R_R} = 8.76$ m.

We now simulate $\Delta\phi_{2nd}$ as a function of z, considering specific values of r: $r = w_0$ and $r = \sqrt{2}w_0$. These values are chosen because they correspond to the typical beam radius at the focus and the Rayleigh range, respectively. Additionally, z is evaluated from the focus to approximately the Rayleigh range which is generally regarded as the region where the paraxial approximation remains valid [49]. The resulting rotation angles and their individual contributions are shown in Figure 3.3, where solid lines correspond to beam radius $r = w_0$ and dashed lines to $r = \sqrt{2}w_0$.

As derived in Eq. (3.11), the rotational angle of the secondary Faraday effect consists of two terms, one arising from the Rayleigh range difference, and the other from the Gouy phase difference. They are plotted separately in blue and red, respectively, in Figure. 3.3. The total secondary effect is plotted in green. Note that the Gouy phase term is independent of the beam radius, so the corresponding red curve is identical for both cases in Figure 3.3. It is evident that the two terms contribute oppositely to the rotation direction, with the Gouy phase term gradually becoming dominant as it accumulates during propagation.

For the parameters of our setup, we estimate that the magnitude of the linear Faraday effect is approximately 10^8 times greater than that of the secondary Faraday effect. Consequently, the rotation due to the difference in refractive indices in the propagation term remains the dominant contribution. It is evident that the secondary effect cannot be observed in the presence of this overwhelmingly large term. To isolate the secondary effect in our calculations, we set the refractive indices to be equal in the *propagation term* for both left- and right-handed polarizations while maintaining their differences in the other terms. This adjustment is implemented using Mathematica simulations to effectively eliminate the linear

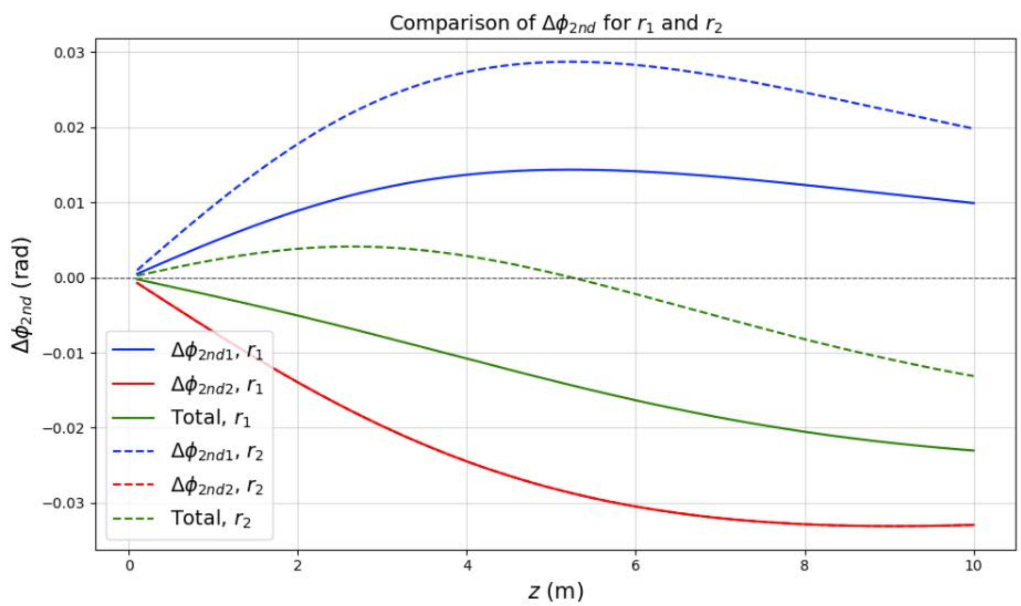

Figure 3.3: Plot of the two terms in Eq. (3.11) describing the secondary rotation, showing their behaviour for two different values of r: $r_1 = w_0$ (solid lines) and $r_2 = \sqrt{2}w_0$ (dashed lines). The blue lines represent the first term, which arises from the Rayleigh range difference; the red lines represent the second term, due to the Gouy phase difference; and the green lines show the total secondary effect. Note that the solid and dashed red lines overlap because the Gouy phase term is independent of r.

Faraday effect. The details and results of these simulations are presented in the next subsection.

3.3.1 Simulation Results for Paraxial RPB

Previously we introduced the secondary Faraday effect, which for paraxial light presents a minute modification to the linear Faraday effect arising purely from propagation with a circularly dichroic medium. Here, we aim to investigate the spatial dependence of this effect in more detail. The refractive indices, wavelength and beam waist are set to be the same as the previous section, and we propagate the beam from $z = -8$ m to $z = 8$ m to ensure that it is within the Rayleigh range. The beam waist is set to be at $z = 0$ m.

In the paraxial regime, we eliminate the linear Faraday effect by setting the refractive indices to be equal in the *propagation term* for both left- and right-handed polarizations while maintaining their differences in the other terms. Consequently, the observed effects on both r and z are exclusively due to the secondary Faraday effect.

The secondary Faraday effect is too weak to produce visually distinguishable differences in the polarization distribution when simulated directly. The resulting patterns appear identical to those of a uniformly rotated linearly polarized beam. Therefore, to highlight the subtle inhomogeneity in the polarization rotation, we instead present the distribution of orientation angle differences relative to the central, un-rotated polarization direction. This enables us to observe the radial and transverse inhomogeneity in polarization rotation. To achieve this, we extract the orientation information of the polarization at every field point using the properties of the polarization ellipse. Specifically, we determine the local orientation of the polarization ellipse from the corresponding local field values, as [69, 68]:

$$\tan(2\psi) = \frac{2E_x E_y \cos\varphi}{|E_x|^2 - |E_y|^2}, \tag{3.12}$$

where ψ is the orientation angle of the polarization ellipse, as given in figure. 2.5, while $\varphi = \varphi_1 - \varphi_2$ is the phases difference between E_x, E_y field components (Eq. (2.31)). This relation can be derived from the expression of Stokes parameters, by taking the ratio of S_2 and S_1 in Eq. (2.33).

In our simulation, we set the beam waist ($z = 0$ m) as the starting plane. This means that the polarization ellipses in this plane are not rotated. As the beam propagates along the $\mathbf{B}$ field, it begins to rotate as it moves further from the beam waist in either the $\pm$ directions. For each plane at a step distance $z_i = i * 2$ m, we calculate the orientation angle at each field point, $\psi(x_j, y_k, z_i)$, and compare it with the orientation angle at the same location in the beam waist plane $\psi(x_j, y_k, 0)$. We then plot the orientation angle difference $\psi(x_j, y_k, z_i) - \psi(x_j, y_k, 0)$, at each $z = z_i$ plane.

In each sub-figure of Figure. 3.4 and Figure. 3.5 we present the spatially resolved orientation angle difference with respect to the non-rotated case as the beam is propagating through the Rayleigh range. In Figure. 3.4, we use different scales for each location in order to emphasize the phase difference distribution of the rotation angles. The scales used for each sub-figure are shown in the attached legends. In Figure. 3.5, as a comparison, we plot the first four figures using the same scale, so that each colour corresponds to a specific rotation angle, with red representing clockwise and blue anticlockwise rotations. The common scale is indicated in the plot legend. We show rotation angles as a density plot rather than a polarization plot as the local rotation inhomogeneity is miniscule, and impossible to observe for paraxial light beams.

The Rayleigh range measures how collimated a beam is, and a beam is typically considered paraxial within the Rayleigh range distance. The mathematical expression for the Gouy phase, $\varphi_g = -\arctan\left(\frac{z}{z_R}\right)$, implies a faster change when the beam is closer to focus. Both of these factors justify our choice to propagate the beam at the Rayleigh range level. Transversely, we looked at the range within $x = y = w_0$, meaning the the radial distance from the optical axis ranges from 0 to $1/\sqrt{2}w_0$. With the analysis given in section 3.3, we can safely conclude that for the chosen transverse and longitudinal ranges, the rotation results from a combination of the Gouy phase difference and the Rayleigh range difference between the two beam components. We can therefore conclude that, in the paraxial case, there exists a secondary Faraday effect that rotates the polarization distribution inhomogeneously.

Recall the Gouy phase we introduced in section 2.4, which is a phase associated with the properties of Gaussian beams. In short, the Gouy phase arises due to the (finite) curvature of the wavefront radius. A finite beam implies a finite spatial distribution, and, according to the uncertainty principle, this in turn means a finite distribution of momentum. That is, a finite beam will have a spread in transverse momentum. Consequently, the secondary Faraday effect will be more pronounced if we increase the transverse momentum, for example, through strong focusing. This is what we will explore in the next section, where we will examine the secondary Faraday effect in the focused case.

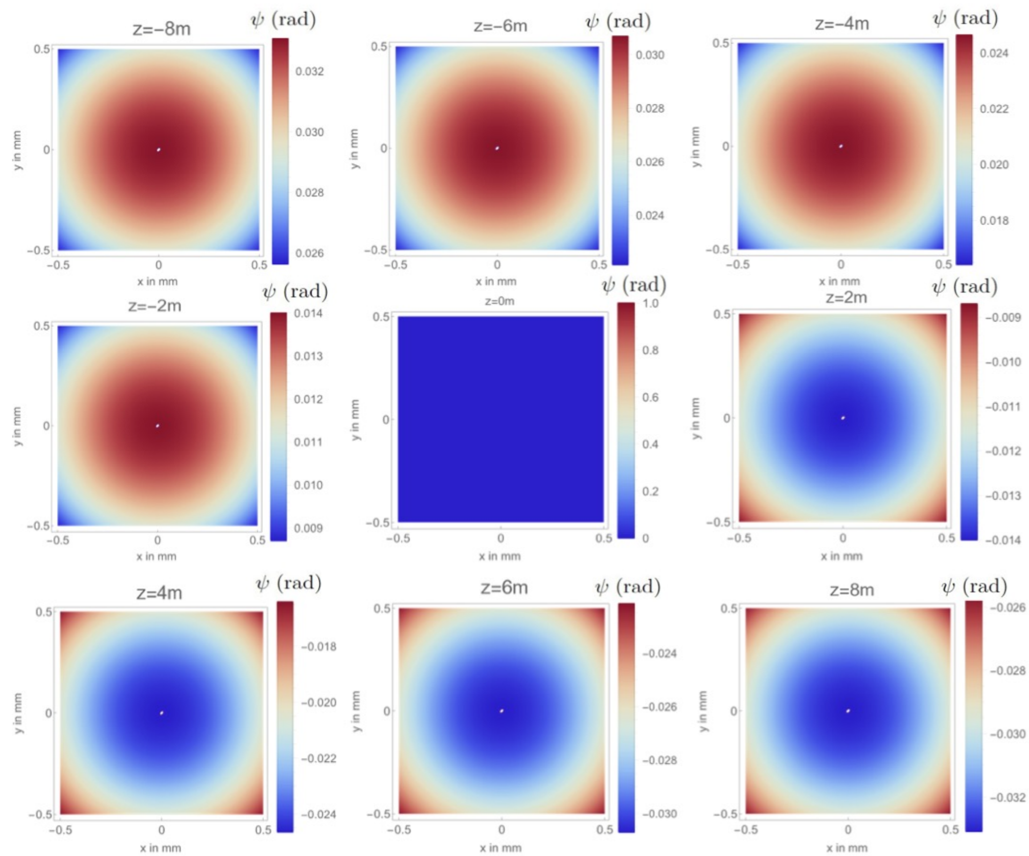

Figure 3.4: Spatial variation of the secondary Faraday effect for a paraxial beam in different propagation planes. Each sub-figure in this figure shows the orientation angle difference relative to the orientation distribution at the focal plane (in units of radians). Note that each sub-figure is plotted with different scales, as shown in their legends. The beam has been propagated approximately a Rayleigh range length. Plus-valued angle corresponds to counter-clockwise rotation and minus-valued angle corresponds to clockwise rotation.

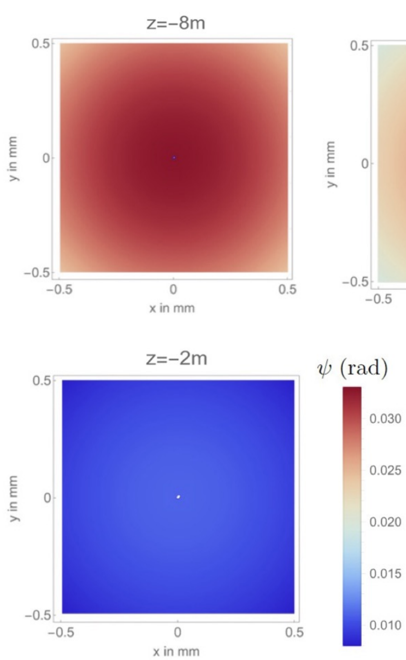

Figure 3.5: Spatial variation of the secondary Faraday effect in a paraxial beam, as in Figure. 3.4 but with all secondary Faraday rotations plotted on the same scale between 0.01 and 0.03 radians. We have plotted the first 4 slices of Fig. 3.4, propagating from -8 m to -2 m.

3.4 Faraday Effect for Strongly Focused RPB

We now know that for paraxial vector vortex beams, the Faraday effect exhibits subtleties compared to simple linearly polarized beams. In the paraxial regime, this secondary effect is many orders of magnitude smaller than the linear Faraday effect, meaning that even in simulations, it can only be observed in the absence of the linear effect. A natural extension of this work is to tightly focus the beam and explore the effect in the non-paraxial regime.

We typically think of paraxial beams as transverse electromagnetic beams; however, this is not entirely accurate, as demonstrated in the previous section, where the secondary Faraday effect arises as a consequence of the Gouy phase and beam radius differences. The longitudinal components are comparably small in the paraxial regime, which is a result of the paraxial approximation [39]. However, under strong focusing, the longitudinal components of the electromagnetic fields become comparable to the transverse components [103]. This leads us to hypothesize that strong focusing could amplify the secondary Faraday effect, making it comparable to the linear Faraday effect.

3.4.1 Focused Radially Polarized Light

In section 2.6, we introduced the theory of Richards and Wolf regarding the propagation and focusing of polarized light using angular spectrum techniques. In scenarios of non-paraxial fields, polarization can exhibit significant variations over length scales approximately equivalent to the wavelength [38]. Here, we present our first application of this theory. To compare with the paraxial case, we specially analyze how the strong focusing system acts on a radially polarized beam and how the strongly focused RPB is affected by the Faraday effect. We still decompose the radially polarized beam into two LG beams, as indicated in Eq. (3.5), but with a slight detour: we first calculate the focused field for HG beams. The advantage of doing so is that the integrations of HG beams are much easier to perform compared to those for LG beams. We then use the relations between HG and LG beams to obtain the focused LG beams.

Strong focusing can be achieved by the aplanatic system introduced in subsection 2.6.2, where the far field of an incident beam, whatever the form, can be calculated on the reference sphere (Figure. 2.7) using Eq. (2.53). By plugging the far field into Eq. (2.49), and with some suitable conversion of variables, we get

$$\begin{aligned} k_x &= k \sin\theta \cos\phi, \\ k_y &= k \sin\theta \sin\phi, \\ k_z &= k \cos\theta, \end{aligned} \tag{3.13}$$

and

$$\begin{aligned} x &= \rho\cos\varphi, \\ y &= \rho\sin\varphi, \end{aligned} \tag{3.14}$$

where θ and ϕ are spherical angles, while ρ and φ are not geometrically meaningful variables, but rather, a mathematical treatment which allows the integration to be evaluated in a closed form [81]. With these new integration variables, we are able to write Eq. (2.49) as

$$\mathbf{E}(\rho,\varphi,z) = -\frac{\mathrm{i}kf\mathrm{e}^{-\mathrm{i}kf}}{2\pi}\int_0^{\theta_{\max}}\int_0^{2\pi}\mathbf{E}_\infty(\theta,\phi)\mathrm{e}^{\mathrm{i}kz\cos\theta}\mathrm{e}^{\mathrm{i}k\rho\sin\theta\cos(\phi-\varphi)}\sin\theta\mathrm{d}\phi\mathrm{d}\theta. \tag{3.15}$$

This equation integrates to give the focal field of arbitrary input paraxial beams by passing them through an aplanatic system with focal length f and numerical aperture NA $= n\sin\theta_{\max}$. This system was introduced in detail in subsection 2.6.2. We will now calculate the far field (the field on the reference sphere), which links the paraxial field to the focused field.

For calculation convenience, and to make use of some results from [39], we first calculate the focal fields for HG beams and then use the relation between HG and LG beams to obtain the focal fields of LG beams. When decomposed into HG beams, the relation between RPB and HG beams is RPB $= \frac{1}{\sqrt{2}}\left(\mathrm{HG}_{10}\boldsymbol{e}_x + \mathrm{HG}_{01}\boldsymbol{e}_y\right)$. We now need to calculate the far field $\mathbf{E}_\infty(\theta,\phi)$ relevant to the $\mathrm{HG}_{10}\boldsymbol{e}_x$ and $\mathrm{HG}_{01}\boldsymbol{e}_y$ beams in order to get the focused field, with the general expression for the far field given in Eq. (2.54). We assume that the incident beam hits the lens at its beam waist, where the wavefront curvature of the beam is infinite. Additionally, we assume the lens has a good anti-reflection coating, so that the transmission coefficients can be assumed to be 1 [39]. With these assumptions we can calculate the far field for the **x**-polarized component as

$$\mathbf{E}^x_\infty(\theta,\phi) = \mathrm{HG}_{10}\left(\rho,\theta,\phi\right)\frac{1}{2}\begin{bmatrix} (1+\cos\theta)-(1-\cos\theta)\cos(2\phi) \\ -(1-\cos\theta)\sin(2\phi) \\ -2\cos\phi\sin\theta \end{bmatrix}\sqrt{\frac{n_1}{n_2}}(\cos\theta)^{1/2}, \tag{3.16}$$

the far field for the **y**-polarized component can be calculated similarly, as

$$\mathbf{E}^y_\infty(\theta,\phi) = \mathrm{HG}_{01}\left(\rho,\theta,\phi\right)\frac{1}{2}\begin{bmatrix} (\cos\theta-1)\sin 2\phi \\ (1+\cos\theta)+(1-\cos\theta)\cos(2\phi) \\ -2\sin\phi\sin\theta \end{bmatrix}\sqrt{\frac{n_1}{n_2}}(\cos\theta)^{1/2}, \tag{3.17}$$

where the beam profiles of higher-order HG beams can be calculated from Eq. (2.20), with a basis transformation from Cartesian coordinates to spherical coordinates in order to perform the integration.

Using mathematical relations, we can integrate Eq. (3.15) in terms of Bessel functions. These can be expressed as integral abbreviations to reduce the length of the matrices. In this thesis, we define a convention using three indices for the integral abbreviations. The first index stands for $(1 \pm \cos\theta)$, with 1 for plus and 0 for minus, and 3 if there is no such term. The second index represents the order of $\sin\theta$, and the third index corresponds to the order of the Bessel functions. With these conventions, we can have

$$\begin{aligned}
&\int_0^{\theta_{\max}} f_w(\theta)(\cos\theta)^{1/2}\sin\theta(1+\cos\theta)J_0(k\rho\sin\theta)\mathrm{e}^{\mathrm{i}knz\cos\theta}\mathrm{d}\theta = I_{110},\\
&\int_0^{\theta_{\max}} f_w(\theta)(\cos\theta)^{1/2}\sin^2\theta J_1(k\rho\sin\theta)\mathrm{e}^{\mathrm{i}knz\cos\theta}\mathrm{d}\theta = I_{321},\\
&\int_0^{\theta_{\max}} f_w(\theta)(\cos\theta)^{1/2}\sin\theta(1-\cos\theta)J_2(k\rho\sin\theta)\mathrm{e}^{\mathrm{i}knz\cos\theta}\mathrm{d}\theta = I_{012},\\
&\int_0^{\theta_{\max}} f_w(\theta)(\cos\theta)^{1/2}\sin^3\theta J_2(k\rho\sin\theta)\mathrm{e}^{\mathrm{i}kz\cos\theta}\mathrm{d}\theta = I_{332},
\end{aligned} \tag{3.18}$$

where n in the propagation term is the refractive index which would be different for left- and right-handed polarizations. The expression $f_w(\theta) = e^{-\left(x^2+y^2\right)/w_0^2}$ gives the apodization function.

We can calculate the focused field by substituting Eq. (3.16) and Eq. (3.17) into Eq. (3.15) and perform the integration. The results can then be expressed in terms of the integral abbreviations defined above. However, we can take it a step further by defining a coefficient matrix for each HG beam. These matrices act on the incident polarization vector (in Jones vector form) and yield the corresponding focused electric field vector. Each matrix element is a coefficient that represents how the different polarization components contribute to the focused field at a given spatial mode. The advantage of doing so is that these matrices can be used to calculate the focused field for arbitrary polarizations. Using our definition of the integral abbreviations, the coefficient matrices for HG beams can be constructed as

$$\begin{aligned}
\mathrm{HG}_{10} &= c\cdot\begin{bmatrix} iI_{121}\cos\varphi + iI_{023}\cos(3\varphi) & -iI_{021}\sin\varphi + iI_{023}\sin(3\varphi) \\ -iI_{021}\sin\varphi + iI_{023}\sin(3\varphi) & (I_{121}+2I_{021})\cos\varphi - iI_{023}\cos(3\varphi) \\ -2I_{330} + 2I_{332}\cos(2\varphi) & 2I_{332}\sin(2\varphi) \end{bmatrix},\\
\mathrm{HG}_{01} &= c\cdot\begin{bmatrix} i(I_{121}+2I_{021})\sin\varphi + iI_{023}\sin(3\varphi) & -iI_{021}\cos\varphi - iI_{023}\cos(3\varphi) \\ -iI_{021}\cos\varphi - iI_{023}\cos(3\varphi) & iI_{121}\sin\varphi - iI_{023}\sin(3\varphi) \\ 2I_{332}\sin(2\varphi) & -2I_{330} - 2I_{332}\cos(2\varphi) \end{bmatrix},
\end{aligned} \tag{3.19}$$

where c is the coefficient defined as $c = -\frac{ikf}{2}\sqrt{\frac{n_1}{n_2}}E_0 e^{ikf}$, with E_0 being the scalar field strength, f the focal length, k the wave number, and n_1, n_2 are the refractive indices before and after focusing, as given in Figure. 2.7. (Note that the equivalent

Eq. (3.62) in [39] is wrong.) When applying this equation later, n_2 will be replaced by n_R or n_L, depending on the relevant context.

Using the relationship between HG and LG modes, we can also construct the coefficient matrices for the LG beams as follows:

$$\begin{aligned}\mathrm{LG}_0^1 &= \frac{ikf^2}{2w_0}\sqrt{\frac{n_1}{n_R}}E_0e^{ikn_Rf}\cdot\begin{bmatrix}M_{11} & M_{12}\\ M_{21} & M_{22}\\ M_{31} & M_{32}\end{bmatrix},\\ \mathrm{LG}_0^{-1} &= \frac{ikf^2}{2w_0}\sqrt{\frac{n_1}{n_L}}E_0e^{ikn_Lf}\cdot\begin{bmatrix}N_{11} & N_{12}\\ N_{21} & N_{22}\\ N_{31} & N_{32}\end{bmatrix},\end{aligned} \tag{3.20}$$

where M_{ij}, N_{ij} are the matrices elements defined as follows:

$$\begin{aligned}M_{11} &= iI_{121}\cos\varphi + iI_{023}\cos(3\varphi) - (I_{121}+2I_{021})\sin\varphi - I_{023}\sin(3\varphi),\\ M_{12} &= -iI_{021}\sin\varphi + iI_{023}\sin(3\varphi) + I_{021}\cos\varphi + I_{023}\cos(3\varphi),\\ M_{21} &= -iI_{021}\sin\varphi + iI_{023}\sin(3\varphi) + I_{021}\cos\varphi + I_{023}\cos(3\varphi),\\ M_{22} &= i(I_{121}+2I_{021})\cos\varphi - iI_{023}\cos(3\varphi) - I_{121}\sin\varphi + I_{023}\sin(3\varphi),\\ M_{31} &= -2I_{330} + 2I_{13}\cos(2\varphi) + 2iI_{13}\sin(2\varphi),\\ M_{32} &= 2I_{13}\sin(2\varphi) - 2iI_{330} - 2iI_{13}\cos(2\varphi),\end{aligned} \tag{3.21}$$

and

$$\begin{aligned}N_{11} &= iI_{121}\cos\varphi + iI_{023}\cos(3\varphi) + (I_{121}+2I_{021})\sin\varphi + I_{023}\sin(3\varphi),\\ N_{12} &= -iI_{021}\sin\varphi + iI_{023}\sin(3\varphi) - I_{021}\cos\varphi - I_{023}\cos(3\varphi),\\ N_{21} &= -iI_{021}\sin\varphi + iI_{023}\sin(3\varphi) - I_{021}\cos\varphi - I_{023}\cos(3\varphi),\\ N_{22} &= i(I_{121}+2I_{021})\cos\varphi - iI_{023}\cos(3\varphi) + I_{121}\sin\varphi - I_{023}\sin(3\varphi),\\ N_{31} &= -2I_{330} + 2I_{332}\cos(2\varphi) - 2iI_{332}\sin(2\varphi),\\ N_{32} &= 2I_{332}\sin(2\varphi) + 2iI_{330} + 2iI_{332}\cos(2\varphi).\end{aligned} \tag{3.22}$$

respectively.

From Eq. (3.5), we multiply these coefficient matrices with corresponding polarizations. After simplification, we can express the strongly focused radially polarized beam as follows:

$$
\begin{aligned}
\mathrm{RPB}_{\text{focused}} =& \frac{1}{\sqrt{2}}\left(\mathrm{LG}_0^1 \boldsymbol{e_R} + \mathrm{LG}_0^{-1}\boldsymbol{e_L}\right) \\
=& \frac{1}{\sqrt{2}}\frac{ikf^2}{2w_0}\sqrt{\frac{n_1}{n_R}}E_0 e^{ikn_R f}\left[\begin{array}{c} i\left(I_{121}-I_{021}\right)\cos\varphi - \left(I_{121}+3I_{021}\right)\sin\varphi \\ i\left(I_{121}-I_{021}\right)\sin\varphi + \left(I_{121}+3I_{021}\right)\cos\varphi \\ -4I_{330} \end{array}\right] + \\
& \frac{1}{\sqrt{2}}\frac{ikf^2}{2w_0}\sqrt{\frac{n_1}{n_L}}E_0 e^{ikn_L f}\left[\begin{array}{c} i\left(I_{121}-I_{021}\right)\cos\varphi + \left(I_{121}+3I_{021}\right)\sin\varphi \\ i\left(I_{121}-I_{021}\right)\sin\varphi - \left(I_{121}+3I_{021}\right)\cos\varphi \\ -4I_{330} \end{array}\right].
\end{aligned}
\tag{3.23}
$$

This is the RPB after focusing. In the next simulation section, we will verify how the secondary effect affects the focused beam. We have chosen a high NA to observe the effect, which results in strong focusing [79].

3.4.2 Gouy phase for strongly focused RPB

One may pose the question how the Gouy phase shift, which is also a rotational effect upon focusing, would affect the polarization structure as the beam propagates. For the case of a paraxial beam, the Gouy phase takes the form of $\arctan((1+N)z/z_R)$, where $N = n + m = |l| + 2p$ is the mode number [49]. For typical radially polarized beams, the mode numbers of both orthogonal polarization components are equal. While each component experiences a phase shift as it propagates through the focus, this phase shift is equal for both components, so that no dephasing occurs, and the common Gouy phase cannot be observed. A simulation of the propagation of a paraxial RPB is given in Figure. 3.6, where we have set the refractive indices to be the same for both left- and right- handed polarization. No polarization rotation is observed. We conclude that the inhomogeneous rotation is solely due to the Faraday effect, or more explicitly, the difference in refractive indices between the two circular polarization components, which we will examine in the following section, and specifically in Figure 3.7 and Figure 3.8.

In the case of strong focusing, however, the Gouy phase no longer takes the form $\arctan((N+1)z/z_R)$. Instead, one should use directly the physical meaning that the Gouy phase is the difference between the phase of the actual field and that of a non-diffracted spherical wave. In [104], the Gouy phase of a strongly focused RPB has been investigated, where again, the aplanatic strong focusing system has been used. The calculation result of a strongly focused RPB field, expressed in terms of its radial and longitudinal components and adapted to our

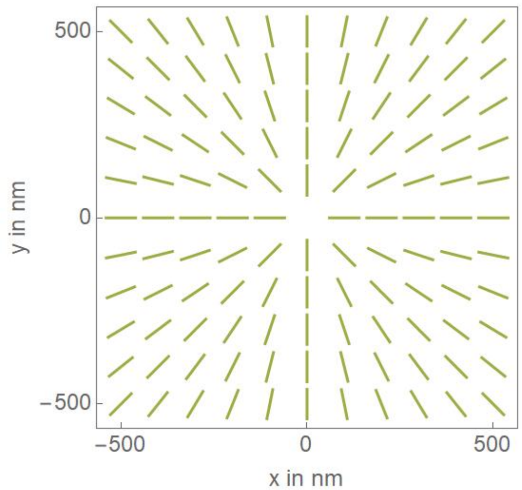

Figure 3.6: The paraxial RPB under the influence of only the Gouy phase during propagation, where the beams remains the same during propagation as in the figure.

mathematical framework, can be written as

$$\begin{aligned} E_z(\rho,z) &= -\mathrm{i}kf^2E_0\int_0^{\theta_{\max}} f_w(\theta)\sin^3\theta(\cos\theta)^{1/2}e^{\mathrm{i}kz\cos\theta}J_0(k\rho\sin\theta)\mathrm{d}\theta, \\ E_\rho(\rho,z) &= -4kf^2E_0e^{ikf}\int_0^{\theta_{\max}} f_w(\theta)(\cos\theta)^{3/2}\sin^2\theta e^{\mathrm{i}kz\cos\theta}J_1(k\rho\sin\theta)e^{\mathrm{i}kz\cos\theta}\mathrm{d}\theta. \end{aligned} \tag{3.24}$$

By comparing the phase of the above expressions and that of a spherical wave, one would obtain [104]

$$\begin{aligned} \delta_z(u,v) &= \arg\left[e_z(u,v)\right] - \mathrm{sign}(u)kR, \\ \delta_\rho(u,v) &= \arg\left[e_\rho(u,v)\right] - \mathrm{sign}(u)kR, \end{aligned} \tag{3.25}$$

where u, v are Lommel variables defined as $u = kz\sin^2\theta_{\max}$ and $v = k\rho\sin\theta_{\max}$ [41]. The Gouy phase for the radial component stabilizes at 2π even for large angles. The Gouy phase for the longitudinal component, however, approaches π as the angle increases. These results and relevant figures can be found in [104] and [105].

3.5 Simulation Results for Strong Focusing Field

In the simulation, we have set the parameters for strong focusing as follows: the numerical aperture is NA = 0.98, the focal length is 0.5 m, and the maximum angle $\theta_{\max}$ is determined by the aplanatic lens in the strong focusing system, defined as $\arctan(\mathrm{NA}/n) = 0.58$ radians. The filling factor can be calculated as $f_0 = \frac{w_0}{f \sin\theta_{\max}}$. And the propagation distance is approximately one wavelength, which is much shorter than the Rayleigh range due to strong focusing. Other parameters, such as the beam waist, field strength, refractive indices, and wavelength, are kept the same as in subsection 3.3.1. For strong focusing, we propagate approximately one wavelength with a suitable cross-sectional area, and we start from the focal point as before.

In Figure. 3.7 we present the total Faraday effect for the strongly focused RPB. Unlike the paraxial case, we do not exclude the linear Faraday effect in the simulation here, as the secondary effect is now comparable to the linear effect.

For comparison, we present the linear Faraday effect for the radially polarized beam in Figure. 3.8, ignoring all secondary effects. The inhomogeneous rotation of the polarization ellipse orientation induced by the secondary effect can be clearly observed when comparing each sub-figure in Figure. 3.7 and Figure. 3.8, as concluded in section 3.3. In addition to the change of the local orientation with the polarization pattern, we observe a change in ellipticities under strong focusing conditions. This becomes even more apparent when again exclude the linear Faraday effect and present only the changes in rotation and ellipticity due to secondary Faraday effect in Figure. 3.9. Finally, in Figure. 3.10, we explicitly present the orientation angle difference between each sub-plot in Figure. 3.7 and Figure. 3.8, providing a clearer presentation of the secondary effect in terms of rotating the rotation of polarization ellipse orientations.

We would like to remark that the Richards and Wolf model is a pure geometrical model. Both the far-field method and the aplanatic system treat the beam as rays. The phase information of the beam is accounted for by the angular spectrum/Fourier optics approach. This means that the phase properties of the beam play a role in its propagation. We can thus conclude that, of the phase term $e^{i\mathbf{kr}}$, the factor $e^{ik_z z}$ causes the linear Faraday effect, while $e^{i(k_x x + k_y y)}$ accounts for the secondary Faraday effect.

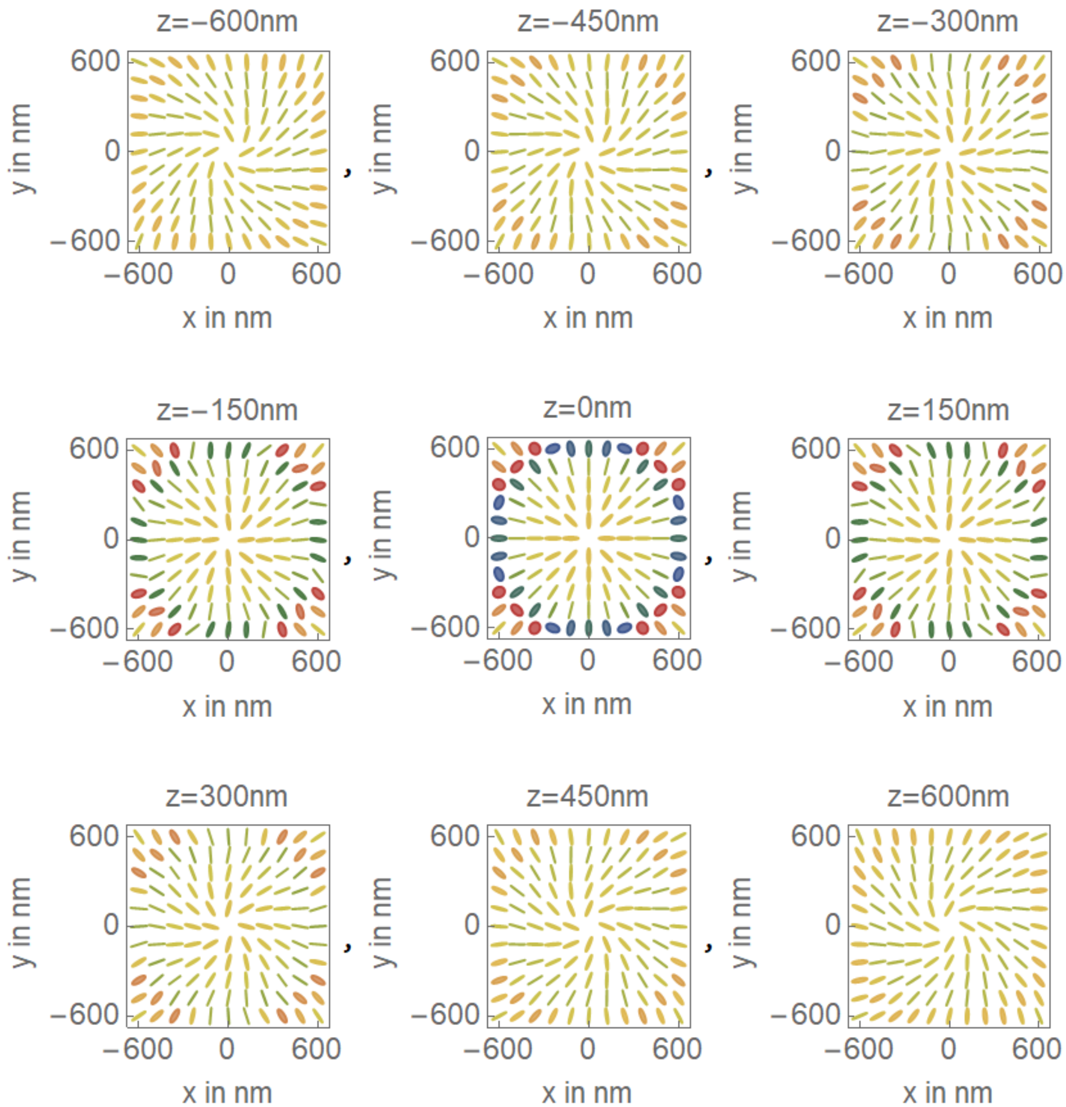

Figure 3.7: The total Faraday effect for a strongly focused radially polarized beam (RPB) is examined. The beam waist is set to 1 mm at focus, consistent with the paraxial case investigated earlier, and the NA is 0.98. The beam at focus is set to be un-rotated, but is also not pure radially polarized due to strong focusing. It is propagated over a distance of approximately one wavelength. The polarization distributions at various propagation distances are presented. The inhomogeneity of the rotation, particularly with respect to the central figure, is also observed.

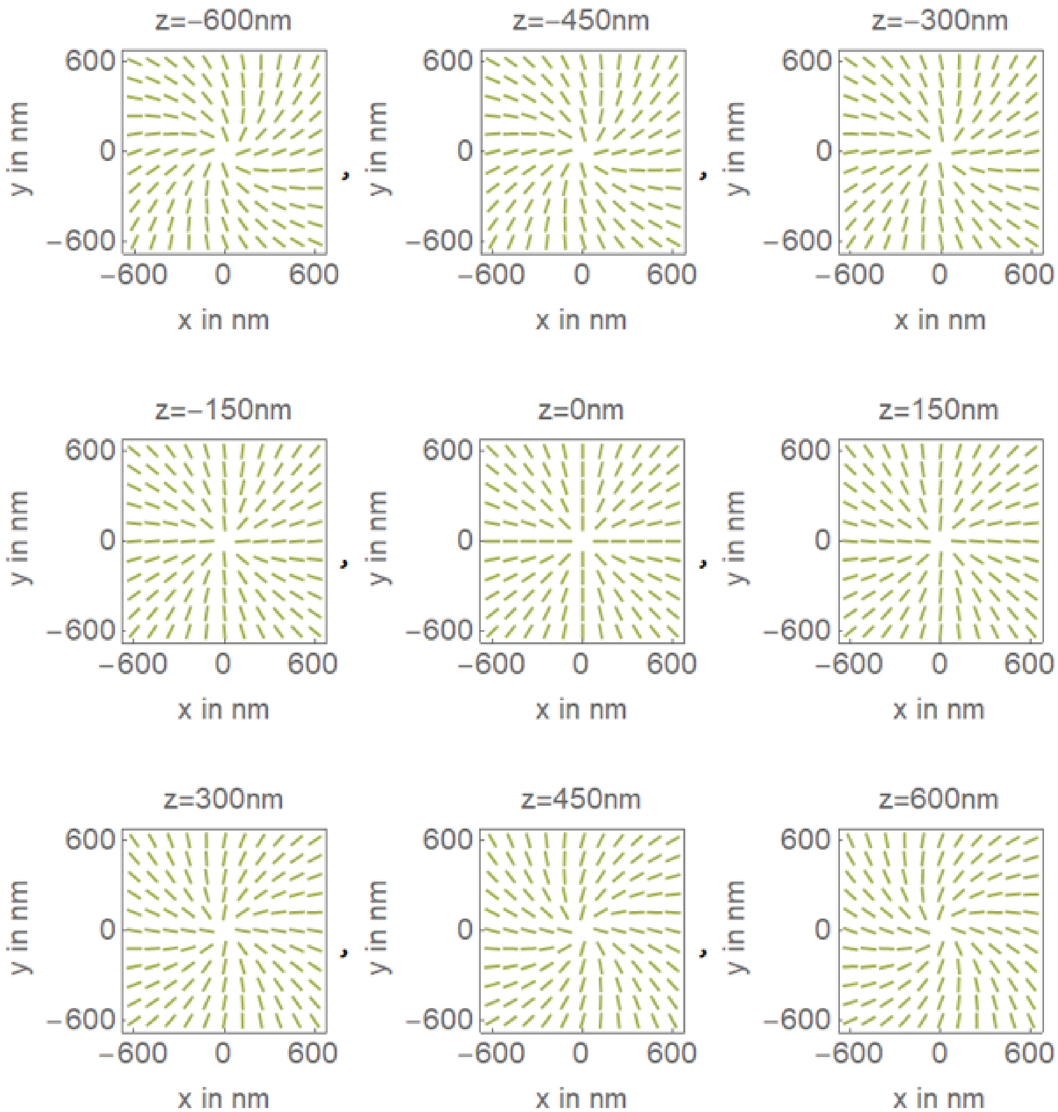

Figure 3.8: Linear Faraday effect for the focused RPB, with beam parameters consistent with Figure 3.7.

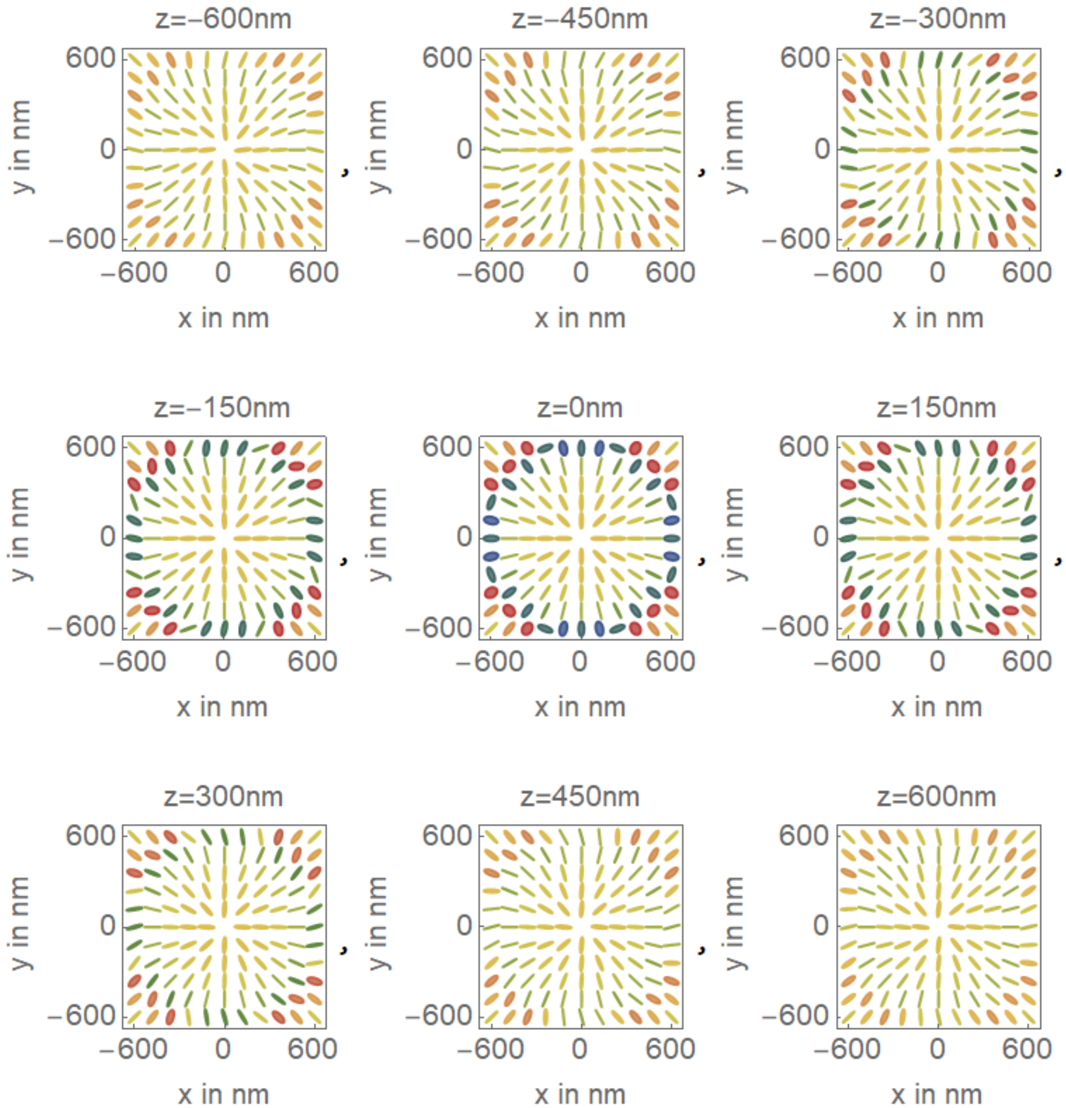

Figure 3.9: In this figure, the linear Faraday effect is excluded, and only the secondary Faraday effect is presented. The beam at the focus is once again set to be unrotated. Polarization distributions at various distances are shown, emphasizing the inhomogeneity of the rotation relative to the central figure. The beam parameters are consistent with Figure 3.7.

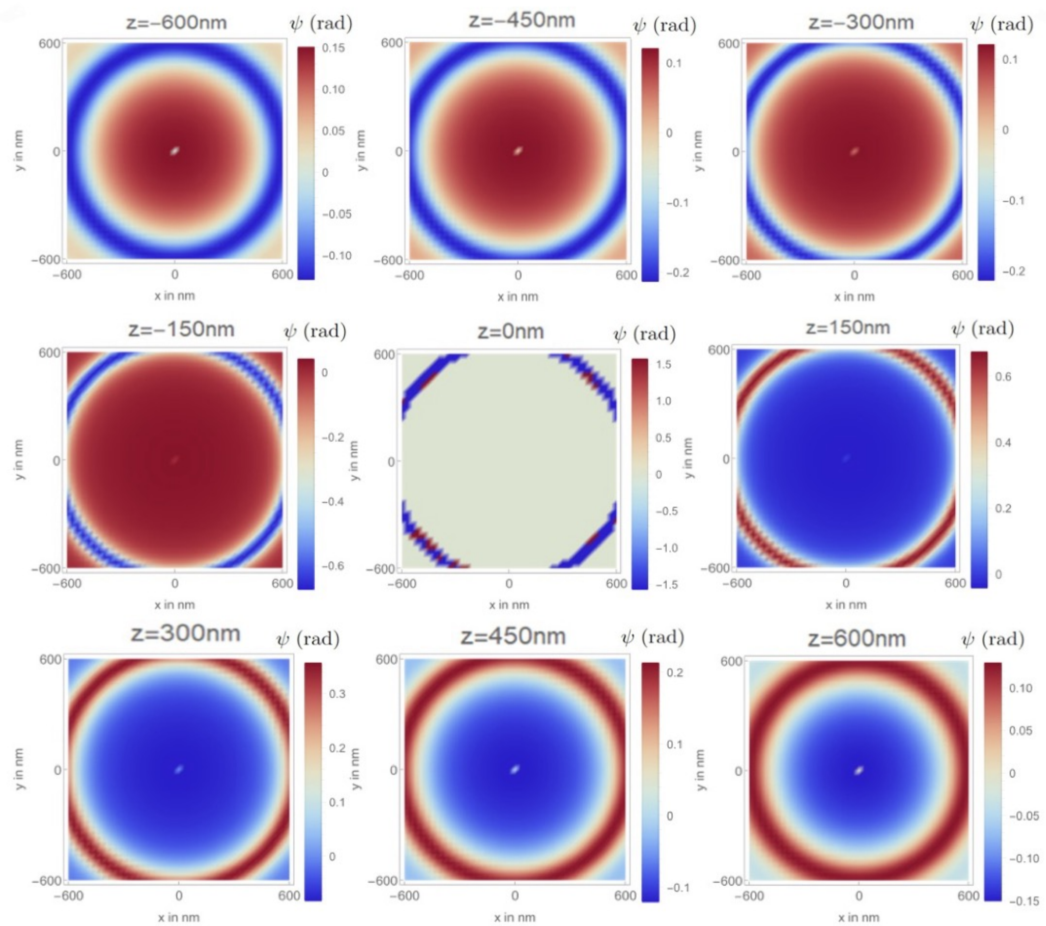

Figure 3.10: The rotational angle difference between the total Faraday effect and the linear Faraday effect for the focused RPB is presented to illustrate the rotational angle direction in transverse planes at each step. At $z = 0$, the plot shows a uniform gray area indicating no rotation across the transverse plane. This serves as a comparison with Figure 3.4 and Figure 3.5. The colour bars (note the different scalings) are in units of radians.

3.6 Preliminary Experimental Results and Outlook

An preliminary experimental result was obtained by Sphinx Svensson from the Optics Group. The Faraday effect measurements were performed using a tightly focused radially polarized beam with NA=0.7 under a near-uniform magnetic field generated by anti-Helmholtz coils (radius $r = 12.5$ cm, an applied voltage of $U = 1.59$ V, and an electric current of $I = 0.5$ A). These coils create a quadrupole magnetic field gradient ($\sim$ 10G/m) central to magneto-optical trapping (MOT) of Rb-87 atoms.

The observed inhomogeneous polarization rotation in Figure 3.11 aligns with predictions for strongly focused beams, where tilted wavevectors induce a mix of Faraday and Voigt effects. The ellipticity χ and orientation ψ changes correlate with the beam's longitudinal polarization component, a feature unique to non-paraxial regimes. Longitudinal polarization components (absent in collimated beams) drive π-tramsitions in Rb-87, marking the first direct observation of such absorption in atomic spectra.

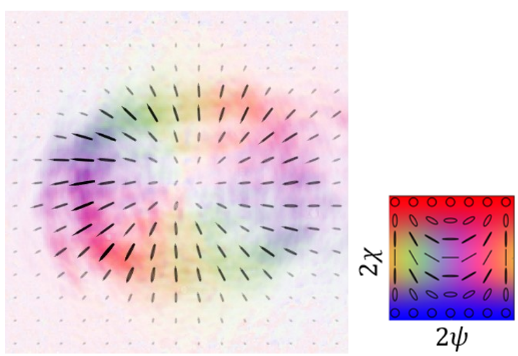

Figure 3.11: Experimental Faraday effect for a tightly focused RPB (NA=0.7) under a magnetic field $\mathbf{B}$ from anti-Helmholtz coils with $r = 12.5$ cm, at $I = 0.5$ A and $U = 1.59$ V. The colour scheme we used is defined in terms of orientation ψ and ellipticity χ, revealing radially inhomogeneous rotation and secondary Faraday effects. Ellipse lengths correlate with local field strength, consistent with nonparaxial longitudinal polarization components

For more details of the experiment we refer the reader to Sphinx's thesis and the upcoming publication.

3.6.1 Discussion of the longitudinal component

Some special-designed, tightly focused structured light modes have been presented in the literature. For example, in [106], a paraxial skyrmion with topological number $n = 2$ is focused, and a Bloch C-skyrmion can be obtained upon focusing with suitable parameters. In [107], a q-plate generates a Poincaré beam from a circularly polarized Gaussian input beam. When tightly focused, the non-paraxial conditions introduce a longitudinal electric field component, twisting the polarization ellipses into a Möbius strip in the focal plane. This topology is experimentally confirmed via 3D nanotomography. In our exploration of the Faraday effect, we also have a non-negligible longitudinal component upon focusing. However, since our beam does not have a special topological structure, it would have a topologically trivial longitudinal component, the behaviour of which is expected to be similar to the transverse component we explored.

3.6.2 Calculation of off-axis incidence

The limitations of the conventional Faraday effect model arise from two idealized assumptions: (1) that the medium is characterized by a simple, linear constitutive relation, and (2) that the beam propagates strictly along the optical axis. While these assumptions may hold in the paraxial regime, they become inaccurate under strong focusing conditions. In particular, strong focusing causes the propagation direction to deviate from the optical axis, introducing longitudinal and oblique field components. Under these circumstances, the Faraday and Voigt effects are no longer separable and must be treated simultaneously. To accurately account for these effects, we consider an optically active medium described by a full susceptibility tensor, following the formalism of [67],

$$\boldsymbol{\chi} = \begin{bmatrix} \chi_{11} & i\chi_{12} & 0 \\ -i\chi_{12} & \chi_{11} & 0 \\ 0 & 0 & \chi_{33} \end{bmatrix}. \tag{3.26}$$

We can construct the wave equation for a plane wave by substituting the above matrix into Maxwell's equations, and using the relation between $\mathbf{D}$ and $\mathbf{E}$. This gives us:

$$\mathbf{k} \times (\mathbf{k} \times \mathbf{E}) + \frac{\omega^2}{c^2}\mathbf{E} = \boldsymbol{\chi}\mathbf{E}, \tag{3.27}$$

the component form of which are not difficult to calculate and can be written in matrix form as

$$\begin{bmatrix} -k_y^2 - k_z^2 + \frac{\omega^2}{c^2}\left(1+\chi_{11}\right) & k_x k_y + i\frac{\omega^2}{c^2}\chi_{12} & k_x k_z \\ k_x k_y - i\frac{\omega^2}{c^2}\chi_{12} & -k_x^2 - k_z^2 + \frac{\omega^2}{c^2}\left(1+\chi_{11}\right) & k_y k_z \\ k_x k_z & k_y k_z & -k_x^2 - k_y^2 + \frac{\omega^2}{c^2}\left(1+\chi_{33}\right) \end{bmatrix} \cdot \mathbf{E} = 0, \tag{3.28}$$

For nontrivial solutions to exist, the determinant of the above matrix must vanish, which leads to a relation between k, ω, and χ. Such relations can also be represented by 3D surface in **k**-space [108]. In this thesis, we focus on the eigenmode solutions to Eq. (3.28). For a given propagation direction, there exist two eigenwaves associated with each solution to the null space of k matrix [108, 109].

The eigenmode of the above wave equation can be calculated to be

$$\mathbf{E} = \begin{bmatrix} \left(k^2 - \frac{\omega^2}{c^2}\left(1+\chi_{11}\right)\right)\left(k^2 - \frac{\omega^2}{c^2}\left(1+\chi_{33}\right)\right) k_x k_y + \left(k^2 - \frac{\omega^2}{c^2}\left(1+\chi_{33}\right)\right) i\frac{\omega^2}{c^2}\chi_{12} k_y^2 \\ \left(k^2 - \frac{\omega^2}{c^2}\left(1+\chi_{11}\right)\right)\left(k^2 - \frac{\omega^2}{c^2}\left(1+\chi_{33}\right)\right) k_y^2 - i\frac{\omega^2}{c^2}\chi_{12}\left(k^2 - \frac{\omega^2}{c^2}\left(1+\chi_{33}\right)\right) k_x k_y \\ -\frac{\omega^4}{c^4}\chi_{12}^2 k_y k_z + \left(-k^2 + \frac{\omega^2}{c^2}\left(1+\chi_{11}\right)\right)^2 k_y k_z \end{bmatrix}. \tag{3.29}$$

As stated above, for each k value, there is an associated eigen polarization. These are the eigenmode solutions for the given propagation direction.

It is possible to use Richards and Wolf focusing system to calculate the beam profile with the above calculated eigenmode, and to capture a full picture involving Faraday effect and Voigt effect.

3.7 Conclusions

In this chapter, we first introduce the Faraday effect for linearly polarized beams, which we referred to as the linear Faraday effect. We then investigate how this birefringence-like property manifests when a beam with a more complex structure is propagated. Specifically, we identified a more subtle, secondary effect that arises for paraxial radially polarized beams. We analyzed the factors contributing to this secondary effect and conclude that the Rayleigh range and the Gouy phase difference between the left and right-handed polarizations are the factors. The secondary Faraday effect leads to an inhomogeneous rotation of the polarization in both radial and longitudinal directions. The simulation results were presented in the absence of the linear Faraday effect, which is strong enough to overshadow the secondary effect.

Strong focusing magnifies the longitudinal component of the beam, which significantly enhances the Gouy phase effect which is related to the longitudinal beam component. This motivates us to investigate the secondary Faraday effect for the strongly focused radially polarized beam. In the case of strong focusing, the secondary Faraday effect becomes comparable to the linear effect, in the sense that it is observable in the presence of the linear effect. Simulation results, along with preliminary experimental results, are presented, showing an inhomogeneous rotation of polarization as one moves radially outward from the optical axis and propagates away from the beam waist (which we set as the starting point). Additionally, changes in the ellipticity of the polarization are observed, but their detailed investigation must be postponed to future research.

We discussed the rotations that a strongly focused radially polarized beam can undergo due to the Gouy phase effect, and briefly related this to the presence of longitudinal polarization components of the beam. These are implicitly included in the Richards & Wolf simulation. We also briefly presented an alternative approach based on identifying the eigenmodes of propagation in a given magnetic field. This method allows us to interpret what we termed the secondary Faraday effect as a combination of Voigt and Faraday effects for off-axis light propagation of the strongly focused beam. It will be interesting to compare the two approaches to obtain a more complete picture of the problem.

Chapter 4

An Introduction to skyrmions

4.1 Introduction

Skyrmions are topological solitons that were first proposed by Tony Skyrme in 1961 [20]. This concept has since had wide-reaching impacts and research interests in various fields of physics. In recent years, this key concept has been developing in optics, enriching light field modulation. In 2020, the Quantum Theory Group of the University of Glasgow proposed the theory of paraxial optical skyrmion beams, where LG beams are used to construct them [22]. As one of my PhD projects, I worked on further developing the theory, including the topological definition of skyrmions, the skyrmion lines, and the change of basis in measuring skyrmion numbers. These contributions are presented in chapter 4 and chapter 5. For the completeness, we include section 4.2, section 4.3, and section 4.4 which summarize Dr. Sijia Gao's work. For a complete and detailed description, we refer the reader to Dr. Gao's published paper and thesis [22, 34].

Polarization states are commonly described by normalized Stokes parameters, which can be represented as the expectation values of Pauli matrices with respect to a beam state. Therefore, we frame this entire theory in the language of quantum mechanics, allowing us to apply the representations and techniques learned from quantum mechanics. Given that skyrmionic structures have also been observed in photon spins [33], this approach will also enhance the description within the quantum mechanical context.

In this chapter, we first provide a brief introduction to the history of skyrmions, with particular emphasis on section 4.2 on how the theory transitions from magnetic skyrmions to optical skyrmions, highlighting both the similarities and differences in their respective research backgrounds. In section 4.3, we introduce how a simple optical skyrmion beam can be constructed by superimposing two Laguerre-Gaussian beams with orthogonal polarizations, and represent their parameters using the language of quantum mechanics. The spatially varying polarization is characterized by normalized Stokes parameters, from which we can define a skyrmion number that describes the topological properties of the beam. A vector field can also be identified from the definition of the skyrmion number, providing the skyrmion number physical meaning as the flux of the skyrmion field.

Because the skyrmion field is divergenceless, as we will show later in section 4.3, it is natural for us to define a vector potential associated with the field, as in section 4.4. We then continue in section 4.5 with the calculation of skyrmion numbers. In addition to the initial definition of the field flux, we can use Stokes' theorem to calculate the skyrmion number through the vector potential, whose form is determined using the Mermin-Ho relation. We explain in detail how the Mermin-Ho relation has been applied in such calculation. We then emphasize a new calculation method which only depends on the phase of relevant Stokes parameters. This new definition emphasizes the topological properties of the field, and is of great significance in practice. In section 4.6 we introduce a new concept of skyrmion field lines, which is a line of constant polarization.

To provide a more intuitive understanding of these abstract topological structures, we conclude this introduction with a visualization of the polarization profile of a skyrmion beam, presented as a stereographic projection of the Poincaré sphere. This mapping helps relate the polarization distribution in real space to a geometric interpretation, allowing one to grasp the meaning of skyrmion numbers more visually.

Skyrmionic beams possess a robust topological structure and specific polarization distributions. By examining the polarization distribution of a skyrmionic beam, one can observe that the polarization pattern can be related to the Poincaré sphere through a stereographic projection, as shown in Figure 4.1, where the colour scheme is defined by spherical angles χ and ψ, which are defined in Figure 2.5 and Figure. 2.6. By counting how many times a skyrmion pattern wraps around the Poincaré sphere, we can determine the skyrmion number. The skyrmion number is typically an integer, although fractional skyrmions—whose skyrmion numbers are not integers—also exist, though they are not discussed in this thesis.

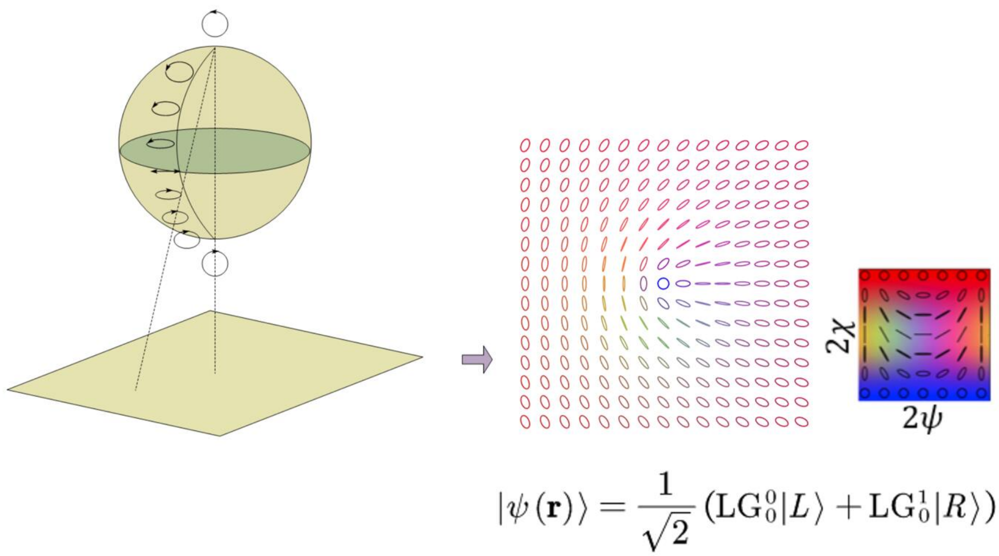

Figure 4.1: Figure illustrating the geometrical interpretation of a skyrmion field. On the left is the stereographic projection of the Poincaré sphere, with the projection point being the North pole of the sphere. On the right is the projected pattern of an n=1 skyrmion texture. This beam is constructed from the LG beams, as shown in the figure. The states $|R\rangle$ and $|L\rangle$ represent right- and left-handed polarizations, respectively. The colour scheme we used is defined in terms of orientation ψ, and ellipticity χ.

4.2 From Magnetic to Optical skyrmions

The concept of skyrmions was first introduced by Tony Skyrme in the 1960s [20], where he proposed a topological soliton model within the framework of nonlinear field theory in particle physics [24]. Although this model did not gain widespread acceptance in mainstream particle theory, it was embraced by the condensed matter community and used to describe spin structures in magnetic materials [110, 111]. These quasiparticles became known as the magnetic skyrmion, a topologically protected structure. The experimental creation and annihilation of magnetic skyrmions have been successfully demonstrated [112]. As a result, magnetic skyrmions have been proposed for various applications, including the development of next-generation information storage devices [113]. Similar features to skyrmions also appear in the theory of superfluids, where the idea of expressing the skyrmion field in terms of the curl of a vector potential $\mathbf{v}$ has been proposed [114, 115], which we will explain in section 4.4.

Magnetic skyrmions can be formed on the surface of a suitable material [116], and can be visualized as a covering of Bloch sphere, on which local magnetization is wrapped around. Magnetic skyrmions are mapped from the stereographic projection of the 3D sphere onto the 2D plane of the magnetic surface [117]. The direction of magnetization at the centre of magnetic skyrmion is opposite to that at a faraway distance from the centre, and it changes gradually from one point to its adjacent. The skyrmion number has been defined counting the number of rotations of the magnetization around the Bloch sphere as we traverse one closed circuit around the centre of the skyrmion pattern, mathematically defined as [116]

$$n = \frac{1}{4\pi} \int \mathbf{M} \cdot \left(\frac{\partial \mathbf{M}}{\partial x} \times \frac{\partial \mathbf{M}}{\partial y} \right) \mathrm{d}x \mathrm{d}y, \tag{4.1}$$

where $\mathbf{M}$ is the local direction of magnetization, such that $\mathbf{M}$ is a unit vector, hence corresponds directly to the Bloch vector on the Bloch sphere.

To transit to the paraxial optics, we replace the local magnetization direction by the normalized Stokes vector $\mathbf{S}$, whose components are normalized Stokes parameters [6, 118]. One important difference between the two is that the normalized Stokes vector, with its components being the normalized Stokes parameters, lives in the Poincaré sphere, which is in parameter space, so a point on the Poincaré sphere does not correspond to a physical direction, while a point on the Bloch sphere corresponds to a specific orientation of the spin. This is a topic we will discuss further in later chapters.

4.3 Paraxial Optical Skyrmion Beams and Skyrmion Fields

We limit our discussion to a paraxial skyrmion beam, which can be constructed using two Laguerre-Gaussian beams with orthogonal polarizations [22]. Borrowing from bra-ket notation, a normalized polarization state representing such a beam can be constructed as:

$$|\psi(\mathbf{r})\rangle = \frac{u_0(\mathbf{r})|0\rangle + e^{i\varphi}u_1(\mathbf{r})|1\rangle}{\sqrt{|u_0(\mathbf{r})|^2 + |u_1(\mathbf{r})|^2}}, \tag{4.2}$$

where $u_0(\mathbf{r})$ and $u_1(\mathbf{r})$ are LG beam profiles, $|0\rangle$ and $|1\rangle$ are two orthonormal polarization states, and φ is a global phase difference between the two states. We could further reduce this form by assign $\mu = e^{i\varphi}u_1(\mathbf{r})/u_0(\mathbf{r})$ as the ratio of the beam profiles of these two LG beams, therefore

$$|\psi(\mathbf{r})\rangle = \frac{|0\rangle + \mu(\mathbf{r})|1\rangle}{\sqrt{1 + |\mu(\mathbf{r})|^2}}. \tag{4.3}$$

The general expression of LG beams, introduced in Eq. (2.23), tells us that $\mu(\mathbf{r})$ takes the form

$$\mu(\mathbf{r}) = f(\rho, z)e^{i\Phi(\rho,\phi,z)} = f(\rho, z)e^{i\ell_d\phi}e^{i\Theta(\rho,z)}, \tag{4.4}$$

where $f(\rho, z)$ is the modulus of $\mu(\mathbf{r})$, $\ell_d = \ell_{u_1} - \ell_{u_0}$ is the winding number difference, and $e^{i\Theta(\rho,z)}$ includes the global phase and the Gouy phase which accounts for the phase change during propagation.

With Eq. (4.4) we write Eq. (4.3) as

$$|\psi(\mathbf{r})\rangle = \frac{|0\rangle + |\mu(\mathbf{r})|\, e^{i\Phi}|1\rangle}{\sqrt{1 + |\mu(\mathbf{r})|^2}}. \tag{4.5}$$

We have introduced the concepts of polarizations and how they are defined on the Poincaré sphere in section 2.5. The (normalized) local polarization can be expressed as the expectation value of the Pauli operator, or equivalently the Pauli vector, $\boldsymbol{\sigma}$, with respect to the polarization state, as [119]

$$\mathbf{S} = \langle\psi(\mathbf{r})|\boldsymbol{\sigma}|\psi(\mathbf{r})\rangle. \tag{4.6}$$

We write out the component form of the Pauli vector, whose components are the Pauli matrices, as follows:

$$\begin{aligned}\sigma_x &= |0\rangle\langle 1| + |1\rangle\langle 0|,\\ \sigma_y &= i(|1\rangle\langle 0| - |0\rangle\langle 1|),\\ \sigma_z &= |0\rangle\langle 0| - |1\rangle\langle 1|.\end{aligned} \tag{4.7}$$

At this stage we do not specify what orthonormal pair $|0\rangle$ and $|1\rangle$ in Eq. (4.5) are referring to, but notice that they are the same orthonormal pair that construct the Pauli matrices. This implies that we are always working in a basis in which $|0\rangle$ and $|1\rangle$ are eigenvectors of σ_z. We call this a *consistent basis measurement*, which means we construct and measure the polarization states in the same orthonormal basis. Physically, this means we have a rotated Poincaré sphere, and the Stokes vector rotates consistently with the sphere. We will discuss the bases more in chapter 5.

With all the above equations, we can calculate the explicit form of the components of $\mathbf{S}$ as [34, 120, 37]

$$\begin{aligned}S_x = S_1 &= \langle\psi|\sigma_x|\psi\rangle\\ &= \frac{1}{1+|\mu|^2}\left(\langle 0| + |\mu|\, e^{-i\Phi}\langle 1|\right)(|0\rangle\langle 1| + |1\rangle\langle 0|)\left(|0\rangle + |\mu|\, e^{i\Phi}|1\rangle\right)\\ &= \frac{1}{1+|\mu|^2}\left(|\mu|\, e^{i\Phi} + |\mu|\, e^{-i\Phi}\right)\\ &= \frac{2\Re(\mu)}{1+|\mu|^2}\\ &= \frac{2f\cos\left[\Theta + (\ell_1 - \ell_0)\,\phi\right]}{1+f^2},\end{aligned} \tag{4.8}$$

$$\begin{aligned}S_y = S_2 &= \langle\psi|\sigma_y|\psi\rangle\\ &= \frac{1}{1+|\mu|^2}\left(\langle 0| + |\mu|\, e^{-i\Phi}\langle 1|\right) i(|1\rangle\langle 0| - |0\rangle\langle 1|)\left(|0\rangle + |\mu|\, e^{i\Phi}|1\rangle\right)\\ &= \frac{i}{1+|\mu|^2}\left(|\mu|\, e^{-i\Phi} - |\mu|\, e^{i\Phi}\right)\\ &= \frac{2\Im(\mu)}{1+|\mu|^2}\\ &= \frac{2f\sin\left[\Theta + (\ell_1 - \ell_0)\,\phi\right]}{1+f^2},\end{aligned} \tag{4.9}$$

$$
\begin{aligned}
S_z = S_3 &= \langle\psi|\sigma_z|\psi\rangle \\
&= \frac{1}{1+|\mu|^2}\left(\langle 0| + |\mu|\, e^{-i\Phi}\langle 1|\right)\left(|0\rangle\langle 0| - |1\rangle\langle 1|\right)\left(|0\rangle + |\mu|\, e^{i\Phi}|1\rangle\right) \\
&= \frac{1-|\mu|^2}{1+|\mu|^2} \\
&= \frac{1-f^2}{1+f^2}.
\end{aligned}
\tag{4.10}
$$

Note that, for later convenience, we have used the labels 1, 2, and 3 here for *consistent basis measurements.* The above are components of the Stokes vector, which can be used to construct the skyrmion field as follows:

$$
\Sigma_i = \frac{1}{2}\varepsilon_{ijk}\mathbf{S}\cdot\left(\frac{\partial\mathbf{S}}{\partial x_j}\times\frac{\partial\mathbf{S}}{\partial x_k}\right). \tag{4.11}
$$

We can prove that the skyrmion field is divergenceless, using the property that $\mathbf{S}$ is a unit vector. To do this we Taylor expand a unit vector at an arbitrary spatial point $\mathbf{r}$, in a vicinity point we call $\mathbf{r}_0$, as

$$
\mathbf{S}|_r = \mathbf{S}|_{r_0} + \left[(\mathbf{r}-\mathbf{r}_0)\cdot\nabla\right]\mathbf{S}|_{r_0}. \tag{4.12}
$$

If we take the modulus square on both sides, we get

$$
\left|\mathbf{S}|_r\right|^2 = \left|\mathbf{S}|_{r_0}\right|^2 + 2\mathbf{S}|_{r_0}\cdot\left((\mathbf{r}-\mathbf{r}_0)\cdot\nabla\right)\mathbf{S}|_{r_0} + O\left(\mathbf{r}-\mathbf{r}_0\right)^2, \tag{4.13}
$$

but $\mathbf{S}$ is a unit vector everywhere, which means that $\left|\mathbf{S}|_r\right|^2 = \left|\mathbf{S}|_{r_0}\right|^2 = 1$. This means that the second term is 0, therefore $\boldsymbol{\Sigma}$ is divergenceless. This proof has been presented in [34, 37]w.

For beams propagating along the z-axis, we are interested in the transverse polarization distribution in the xy-plane. Therefore, we evaluate the skyrmion number by integrating the z-component of $\boldsymbol{\Sigma}$ over this transverse plane:

$$
n = \frac{1}{4\pi}\int_A \mathbf{S}\cdot\left(\frac{\partial\mathbf{S}}{\partial x}\times\frac{\partial\mathbf{S}}{\partial y}\right)\mathrm{d}x\mathrm{d}y = \frac{1}{4\pi}\int_A \Sigma_z \mathrm{d}x\mathrm{d}y. \tag{4.14}
$$

The skyrmion number is a topological invariant that counts how many times the polarization state wraps around the Poincaré sphere.

4.4 Skyrmion Potential

Due to the transversality of the field, we are able to define a vector potential. This vector potential is not of physical significance, but it is of mathematical convenience. To find this vector potential, a theorem of Mermin-Ho relation from superfluid theory has been applied [121], where two vectors $\mathbf{m}$ and $\mathbf{n}$ are defined to form an orthonormal triad with $\mathbf{S}$ such that $\mathbf{S} = \mathbf{m} \times \mathbf{n}$. The Mermin-Ho relation allows us to find the relevant vector potential from these vectors as

$$v_i = \mathbf{m} \cdot \frac{\partial}{\partial x_i} \mathbf{n}, \tag{4.15}$$

where v_i is the vector potential in its component form. Using Stokes' theorem, the skyrmion number can therefore be calculated from this vector potential by line integration

$$n = \frac{1}{4\pi} \oint_C \mathbf{v} \cdot \mathrm{d}\boldsymbol{\ell}, \tag{4.16}$$

where C is the suitable contour around the area of integration A.

To calculate a skyrmion number in practice however, is not as simple as choosing a large circle around the area. It involves subtleties of excluding the singularities, this has been discussed in detail in [37]. Here we will use a figure to illustrate how the contour is chosen. The way in which this is achieved is analogous to that employed in contour integration for dealing with poles in the complex plane. An example of this is depicted in Fig. (4.2): the required contour omits any singular points in $\mathbf{v}$ by passing from the large radius contour, in towards any singular points, circling them and then returning to the large radius component of the closed contour. In this way the singularities of $\mathbf{v}$ are left outside the integration contour. The line integrals along the straight lines in from the outer circular path cancel with those in the opposite direction. Hence we are left only with contributions from the large circular contour and those around and close to the singular points. Consequently, the skyrmion number is

$$n = \frac{1}{4\pi} \left(\oint_{\mathcal{L}_\infty} \mathbf{v} \cdot \mathrm{d}\boldsymbol{\ell} - \sum_j \oint_{\mathcal{L}_j} \mathbf{v} \cdot \mathrm{d}\boldsymbol{\ell} \right), \tag{4.17}$$

where $\mathcal{L}_\infty$ is the outside circle, and $\mathcal{L}_j$ are the circles around singularity points.

We will explain in detail in the next section how different methods of calculating skyrmion number works. We will focus on the topological method, which is most convenient for experimental measurements.

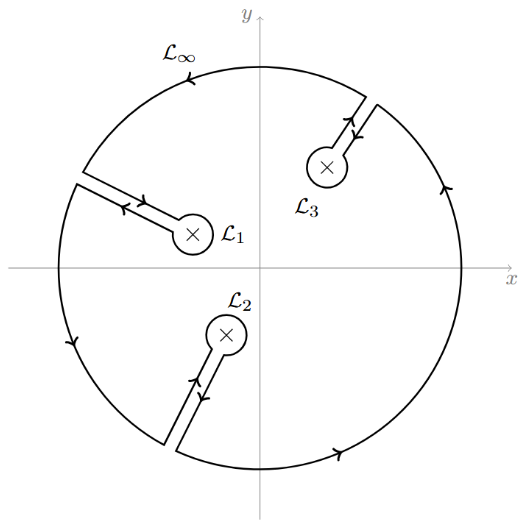

Figure 4.2: Figure indicating the suitable contour for calculating skyrmion numbers, where all singularities are excluded.

4.5 Calculating skyrmion Numbers: From Definition to a Topological Way

From Eq. (4.14) and Eq. (4.16) we already know there are two ways to calculate the skyrmion number, based on the skyrmion field and its relevant vector potential. As stated before, the vector potential can be found through the Mermin-Ho relation, which we now demonstrate in detail. A suitable choice of **m** and **n** are as follows

$$\begin{aligned}\mathbf{m} &= \frac{1}{\sqrt{S_x^2+S_y^2}}\left(S_y\hat{\mathbf{x}} - S_x\hat{\mathbf{y}}\right), \\ \mathbf{n} &= \frac{1}{\sqrt{S_x^2+S_y^2}}\left[-S_zS_x\hat{\mathbf{x}} - S_zS_y\hat{\mathbf{y}} + \left(S_x^2+S_y^2\right)\hat{\mathbf{z}}\right],\end{aligned} \tag{4.18}$$

where **m** can be found simply by observation, and **n** is just $\mathbf{S}\times\mathbf{m}$. We can find the vector potential by plugging Eq. (4.18) into Eq. (4.15) and get

$$v_i = \frac{S_z}{S_x^2+S_y^2}\left(S_y\frac{\partial}{\partial x_i}S_x - S_x\frac{\partial}{\partial x_i}S_y\right). \tag{4.19}$$

This is the quantity we integrate over the suitably chosen integration path. We see that there are derivative terms we need to calculate. This form of integral, by the means of an integration over vector potential (as in Eq. (4.17)) is already better than the integration over the second derivative, which would be required if we used the skyrmion field to calculate the skyrmion number (Eq. (4.14)). We want to avoid derivative terms in practice for the reason that the area of singularities would be low intensity area in experiment, where noise become comparable with the data, and any derivative would only worsen the situation. We could even do better with one step further, by defining a new set of variables. Resembling the raising and lowering operators in quantum theory, we get what we call *complex Stokes parameter*, as

$$S_{\pm} = S_x \pm iS_y, \tag{4.20}$$

where S_x and S_y are Stokes parameters in any of the consistent basis measurements. A *Stokes phase* can be defined for the complex Stokes parameters, as

$$\Phi = \arctan\frac{S_y}{S_x}. \tag{4.21}$$

Substituting the expressions of S_x and S_y calculated in Eq. (4.8) and Eq. (4.9), we obtain

$$\begin{aligned} S_{\pm} &= \frac{1}{1+|\mu|^2}\left(|\mu|\,e^{i\Phi} + |\mu|\,e^{-i\Phi}\right) \mp \frac{1}{1+|\mu|^2}\left(|\mu|\,e^{-i\Phi} - |\mu|\,e^{i\Phi}\right) \\ &= \frac{2\,|\mu|}{1+|\mu|^2}e^{\pm i\Phi} \\ &= |S_{\pm}|\,e^{\pm i\Phi}, \end{aligned} \tag{4.22}$$

where $S_{\pm}$ are complex conjugate to each other, and we can calculate $|S_+| = |S_-| = \frac{2|\mu|}{1+|\mu|^2}$.

Clearly, S_x and S_y can be expressed in terms of $S_{\pm}$, which allows the vector potential to be written as

$$v_i = \frac{S_z}{2S_+S_-}i\left(S_-\frac{\partial}{\partial x_i}S_+ - S_+\frac{\partial}{\partial x_i}S_-\right). \tag{4.23}$$

Substituting Eq. (4.22) to Eq. (4.23), we can calculate the derivatives

$$\begin{aligned} &S_-\partial_i S_+ - S_+\partial_i S_- \\ &= |S_+|\,e^{-i\Phi}\left(e^{i\Phi}\partial_i\,|S_+| + |S_+|\,\partial_i e^{i\Phi}\right) - |S_+|\,e^{i\Phi}\left(e^{-i\Phi}\partial_i\,|S_+| + |S_+|\,\partial_i e^{-i\Phi}\right) \\ &= |S_+|^2\left(e^{-i\Phi}\partial_i e^{i\Phi} - e^{i\Phi}\partial_i e^{-i\Phi}\right) \\ &= 2i\,|S_+|^2\,\partial_i\Phi, \end{aligned} \tag{4.24}$$

from which we simplify Eq. (4.23) as

$$v_i = -S_z \partial_i \Phi. \tag{4.25}$$

Now, from Eq. (4.17), we see clearly that the skyrmion number of a field can be calculated in the following way:

$$n = \sum_j \frac{1}{4\pi} \oint_{\beta_j} S_z \partial\Phi \cdot \mathrm{d}\boldsymbol{\ell} - \frac{1}{4\pi} \oint_{\alpha} S_z \partial\Phi \cdot \mathrm{d}\boldsymbol{\ell}, \tag{4.26}$$

where α, β are contours over the periphery of the field and around the singularity(s), respectively. As Stokes parameter S_z approaches a single value both at singularity(s) and infinity, we can take it out of the integral and now what's been evaluated is the winding number

$$N = (2\pi)^{-1} \oint \partial\Phi \cdot \mathrm{d}\boldsymbol{\ell}. \tag{4.27}$$

From this we identify a topological definition of the skyrmion number

$$n = \frac{1}{2}\left(\sum_j S_z^{(j)} N_j - \bar{S}_z^{(\infty)} N_\infty\right), \tag{4.28}$$

where $\bar{S}_z^{(\infty)}$ is the value of S_z at infinity, N_j counts the number of rotations around singularities, and N_∞ is the winding number at infinity. It is not difficult to identify that $\sum_j N_j = N_\infty$ by a continuous deformation of the integration lines, as shown in Figure. 4.3: in (a) we have inner integration lines around each of the singularities. These integration lines can be connected without changing the result as the straight lines would cancel each other out, as shown in (b). (b) and (c) are topologically equivalent, and from (c) to (d) the straight lines again cancel out. We see from these figures how $\sum_j N_j = N_\infty$.

This allows us to write Eq. (4.28) as

$$n = \frac{1}{2}\sum_j \left(S_z^{(j)} - \bar{S}_z^{(\infty)}\right) N_j. \tag{4.29}$$

The polarization direction at the center of a skyrmion pattern is always opposite to that at infinity, due to the way it is constructed. This ensures that the two Stokes parameters at the center and at infinity have the same parity, which implies that, despite the presence of the $\frac{1}{2}$ coefficient, n remains an integer.

This is what we call the topological method of calculating the skyrmion numbers.

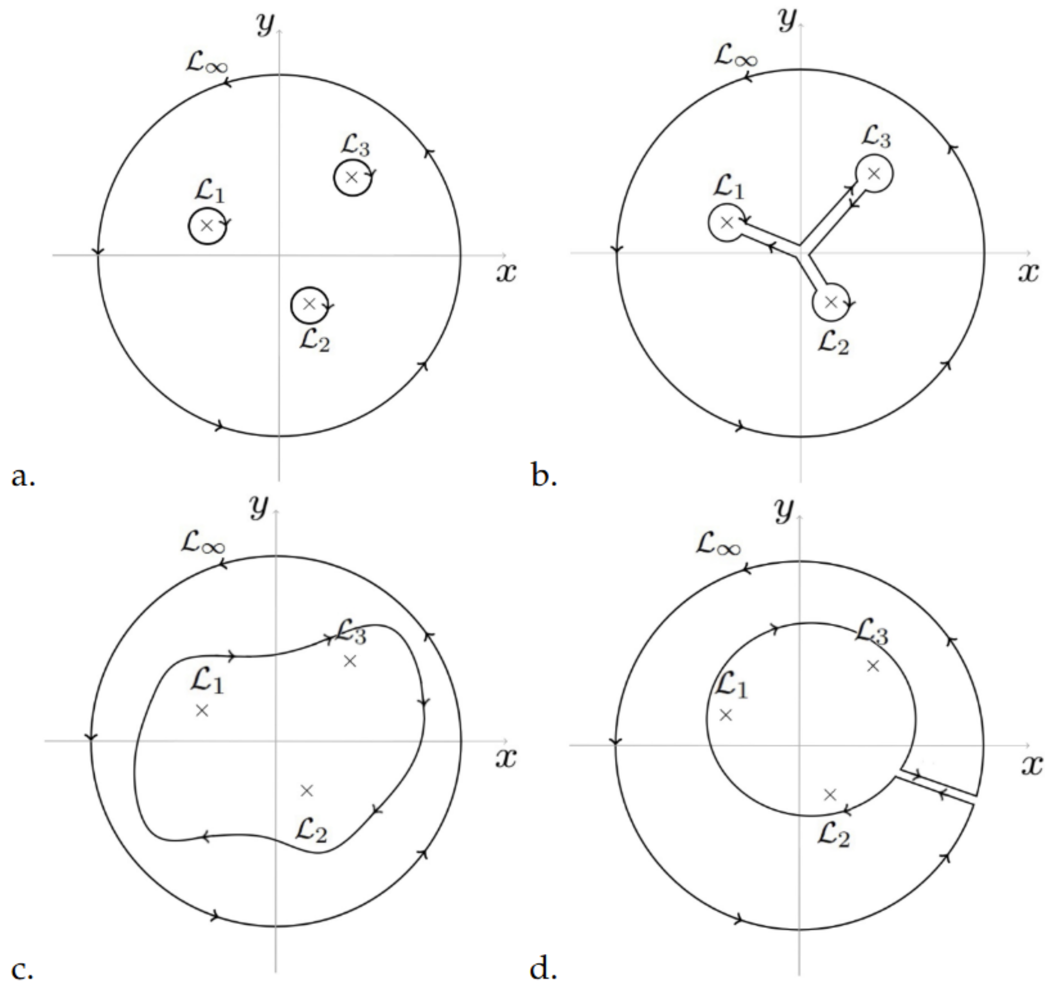

Figure 4.3: Inner and outer integration contours can be deformed and stretched (from a to d) without changing the value of the skyrmion number.

4.6 Skyrmion Field Lines

The mathematical properties of the skyrmion field lines are derived directly from their definition. Firstly, the skyrmion field is transverse, $\boldsymbol{\nabla} \cdot \boldsymbol{\Sigma} = 0$, and it follows that the skyrmion field lines are unbounded; they can exist only as closed loops or extend to infinity. It follows, also, that they cannot merge or split. Secondly, the skyrmion field lines are basis independent in that they are unchanged by a global rotation of the Stokes vector on the Poincaré sphere. This means that knowledge of the skyrmion field does not determine the polarization pattern. It remains, however, to determine the physical significance of the skyrmion field lines and we address this here.

Inspection of numerous polarization patterns leads to the conjecture that skyrmion field lines are lines of constant polarization. That this is indeed the case was proven in [122] but, for completeness, we give a summary of the main points here. We start with the observation that our general polarization pattern can be written in the form of a spatially varying ket as given in Eq. (4.3). It follows that the polarization at any given point is determined solely by, and in one-to-one correspondence with, the complex field $\mu(\mathbf{r})$. Hence lines of constant polarization are contours of constant μ.

The transverse nature of the skyrmion field means that at any given point, $\mathbf{r}_0$, only a single skyrmion field line is present and, moreover, that this line is continuous at this point. It follows that at $\mathbf{r}_0$ there is a direction $u(\mathbf{r}_0)$ along which the Stokes parameters, $\mathbf{S}$, do not change:

$$\mathbf{u}(\mathbf{r}_0) \cdot \nabla S_i(\mathbf{r}_0) = 0\,. \tag{4.30}$$

As the Stokes parameters do not change in this direction it follows, necessarily, that the polarization also does not change. Hence $\mathbf{u}(\mathbf{r}_0)$ determines the direction of a line of constant polarization, which includes but is not restricted to C lines and L lines (lines of circular and specific linear polarization) [60, 123, 124].

To prove that lines of constant polarization are also skyrmion field lines, we return to the definition of the skyrmion field, given in Eq. (4.11), and evaluate this expression by introducing, at each point, two unit vectors $\mathbf{v}(\mathbf{r}_0)$ and $\mathbf{w}(\mathbf{r}_0)$, where $\mathbf{u}$, $\mathbf{v}$ and $\mathbf{w}$ are orthonormal vectors satisfying the right-hand rule so that, for example, $\mathbf{u} = \mathbf{v} \times \mathbf{w}$, as depicted in Fig. 4.4 a. Hence the components of the skyrmion field in this coordinate system are

$$\Sigma_u = \frac{1}{2}\varepsilon_{pqr}\; S_p \left(\frac{\partial S_q}{\partial v}\frac{\partial S_r}{\partial w} - \frac{\partial S_q}{\partial w}\frac{\partial S_r}{\partial v} \right)\,, \tag{4.31}$$

$$\Sigma_v = \frac{1}{2}\varepsilon_{pqr}\; S_p \left(\frac{\partial S_q}{\partial w}\frac{\partial S_r}{\partial u} - \frac{\partial S_q}{\partial u}\frac{\partial S_r}{\partial w} \right)\,, \tag{4.32}$$

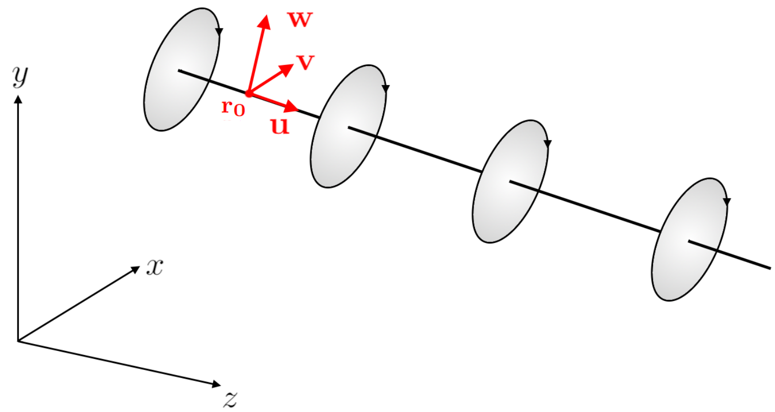

a.

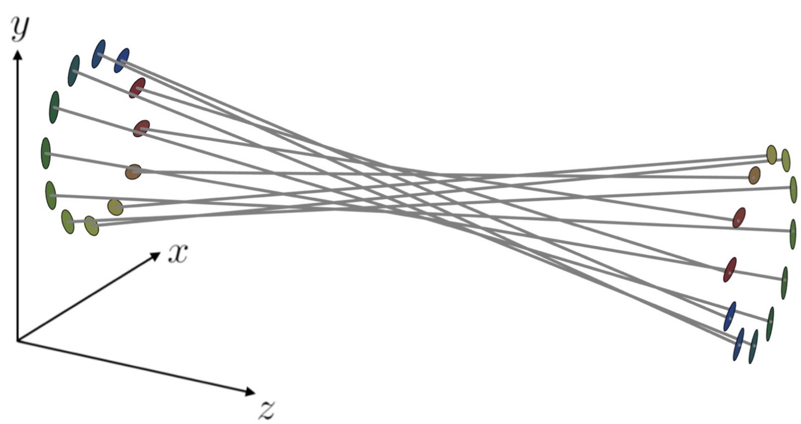

b.

Figure 4.4: a. A line of constant elliptical polarization and the local coordinate system **u**,**v**,**w** at $\mathbf{r_0}$. b. A twisted mesh of lines of constant polarization for a paraxial skyrmion beam ($n = 1$) freely propagating over eight Rayleigh ranges [37].

$$\Sigma_w = \frac{1}{2}\varepsilon_{pqr}\ S_p \left(\frac{\partial S_q}{\partial u}\frac{\partial S_r}{\partial v} - \frac{\partial S_q}{\partial v}\frac{\partial S_r}{\partial u}\right). \tag{4.33}$$

The derivatives of the Stokes parameters are zero along the direction $\mathbf{u}$ and it follows, therefore, that $\Sigma_v = 0 = \Sigma_w$. The one remaining non-zero component of the skyrmion field at $\mathbf{r}_0$ is Σ_u and it follows, therefore, that the skyrmion field line at any point, $\mathbf{r}_0$, points along the direction of constant polarization. Further details and consequences of this may be found in [122]. In a typical skyrmionic optical beam with $n = 1$ the lines of constant polarization form a twisted mesh of straight lines shown in Fig. 4.4 b.

The identification of skyrmion field lines with lines of constant polarization is general and holds whether or not the structured light has a non-zero skyrmion number. As such, skyrmion field lines provide a natural way to extend studies of L and C lines to arbitrary polarizations. A fully general comparison, however, requires an extension of the ideas presented here to non-paraxial fields. We intend to explore this in the future work.

4.7 Conclusions

In this chapter, we have introduced the concepts of skyrmions, which was originally formed in particle physics, and later applied in magnetic materials. Optical skyrmions were formed in analog with the magnetic skyrmions, but have their own features as light beams with spatially varying polarization pattern. We have introduced the formation of such beams using LG beams, and the important topological feature captured by the skyrmion number. From the skyrmion number we identify a vector field as the skyrmion field, from which a vector potential can be defined. This definition allows us to calculate the skyrmion number as line integral of the vector potential with suitable integration contours. On the ground of this, we proposed a new topological way of calculating skyrmion numbers using the complex Stokes phase and winding numbers. We also proposed the concept of skyrmion field lines, which are lines of constant polarization, which is a concept that can be used to track the propagation of skyrmion beams, a generalization of the current singular lines, and can potentially be generalized to higher dimensions.

Chapter 5

Basis Change in Constructing and Measuring of Skyrmion Field

5.1 Introduction

In chapter 4, we introduced skyrmionic structures in magnets and extended the theory to paraxial optical science. In this chapter, we further develop the theory in the context of a generalization of parameters, which allow us to understand how optical skyrmions, recently discovered optical bimeronic structures, and countless intermediate structures can be unified.

The structure of this chapter is as follows: in section 5.2, we discuss the basis-independent property of skyrmion fields within the framework of *consistent basis measurements*, a term we briefly mentioned in section 4.3, using the language of matrix representations. This approach provides a new way of proving the divergenceless, or transversality, property of a skyrmion field, which we previously demonstrated using a Taylor expansion in section 4.3. Writing the skyrmion field which has the form of a triple product in the matrix language is not something new [34], but we offer a more reasonable way of constructing it, with a new geometrical interpretation which provides intuitive understanding of the invariance of such quantity under a rotation.

In section 5.3, we explore the consequences of using different bases for constructing a skyrmion beam and measuring the Stokes parameters, thereby deviating from the consistent basis measurements. We demonstrate that the skyrmion field is unaffected by a *mixed-up bases measurement*. In section 5.4, we calculate the skyrmion potential for such generalized measurements, proving that, despite changes in the vector potentials in mixed-up bases measurements, the curl relation between the vector potential and skyrmion fields remains valid. In section 5.5, we introduce our construction of general orthonormal states and the generalized

Pauli matrices that can be derived from these generalized states. In section 5.5, we present skyrmion textures and their generalized equivalents, also extending the concept of singularities in this context. Such generalization is beneficial not only in the theoretical aspect, but also in the accuracy of the experimental results. We present experimental setups and measurement results in section 5.8. Finally, in section 5.9, we summarize the chapter.

In this chapter, I am responsible for the whole theory part, and the experiment is carried out by the Optics Group, with Prof. Sonja Franke-Arnold took the lead, and Dr. Claire Cisowski and Dr. Amy McWilliam doing the measurements and data analysis. I was involved in discussing the experimental design and data analysis.

5.2 Base Independence of Skyrmion Field in Consistent Basis Measurements

Previous studies have shown that the skyrmion field is independent of the choice of coordinate system [37, 34]. There are several ways to prove this claim, the most straightforward way is by brute force calculation from Eq. (4.11), which we will not reproduce here. Instead, we introduce a determinant representation which will relate to later constructions, as we show in the following.

Since the skyrmion field is defined as a triple product, it is naturally suited to be written as a determinant. To analyze its behaviour under basis changes (which correspond to spatial rotations), we construct a skyrmion matrix whose determinant yields the skyrmion field. Matrices respond predictably to rotations, while the determinant remains invariant as a scalar.

Due to the properties of determinants, there are many alternative ways to construct a skyrmion matrix whose determinant relate to the same skyrmion field, and we have to be careful which one we choose. To rotate the matrix "correctly", i.e., we require that its determinant always corresponds to the skyrmion field constructed from the Stokes vector in the same frame: before rotation for the original matrix, and after rotation for the rotated one. we write it as

$$\mathbf{M}_{\mathrm{s}} = \begin{bmatrix} S_p & \partial_j S_p & \partial_k S_p \\ S_q & \partial_j S_q & \partial_k S_q \\ S_r & \partial_j S_r & \partial_k S_r \end{bmatrix}, \tag{5.1}$$

and we claim its rotated form is

$$\mathbf{M}'_{\mathrm{s}} = \begin{bmatrix} S'_p & \partial_j S'_p & \partial_k S'_p \\ S'_q & \partial_j S'_q & \partial_k S'_q \\ S'_r & \partial_j S'_r & \partial_k S'_r \end{bmatrix}. \tag{5.2}$$

where the determinant of $\mathbf{M}_{\mathrm{s}}$ is the skyrmion field, the subscript "s" indicates "skyrmion" and not a component. And un-primed elements correspond to a un-rotated frame, while primed elements corresponds to a rotated frame.

In the matrix for the rotated skyrmion field, the first column is just $[S_p, S_q, S_r]^T$ after rotation. We want the matrix to rotate "correctly", just like column vectors. For this we must examine the derivative terms also rotate "correctly". To do this we prove that the derivative operator and the rotational operator commute (taking a two-component vector for simplicity, the same rule applies to a 3-vector):

$$\begin{aligned} \mathbb{R}\begin{bmatrix} \partial_j S_p \\ \partial_j S_q \end{bmatrix} &= \begin{bmatrix} \cos\theta\partial_j S_p - \sin\theta\partial_j S_q \\ \sin\theta\partial_j S_p + \cos\theta\partial_j S_q \end{bmatrix}, \\ \partial_j\left(\mathbb{R}\begin{bmatrix} S_p \\ S_q \end{bmatrix}\right) &= \partial_j\begin{bmatrix} \cos\theta S_p - \sin\theta S_q \\ \sin\theta S_p + \cos\theta S_q \end{bmatrix} = \begin{bmatrix} \cos\theta\partial_j S_p - \sin\theta\partial_j S_q \\ \sin\theta\partial_j S_p + \cos\theta\partial_j S_q \end{bmatrix}. \end{aligned} \tag{5.3}$$

Note that $\cos\theta$ and $\sin\theta$ are constants so they can be taken out of the derivative. This means the derivative terms rotate just the same way as the normal terms, which allows us to relate the skyrmion matrix constructed from the $\mathbf{S}'$ and $\mathbf{S}$ by a rotational matrix as

$$\begin{aligned} \mathbf{M}'_{\mathrm{s}} = \mathbb{R}\mathbf{M}_{\mathrm{s}} &= \begin{bmatrix} R_{11} & R_{12} & R_{13} \\ R_{21} & R_{22} & R_{23} \\ R_{31} & R_{32} & R_{33} \end{bmatrix}\begin{bmatrix} S_p & \partial_j S_p & \partial_k S_p \\ S_q & \partial_j S_q & \partial_k S_q \\ S_r & \partial_j S_r & \partial_k S_r \end{bmatrix} \\ &= \begin{bmatrix} S'_p & \partial_j S'_p & \partial_k S'_p \\ S'_q & \partial_j S'_q & \partial_k S'_q \\ S'_r & \partial_j S'_y & \partial_k S'_r \end{bmatrix}. \end{aligned} \tag{5.4}$$

The rotated skyrmion field can therefore be obtained just by taking the determinant of the rotated skyrmion matrix $\mathbf{M}'_{\mathrm{s}}$:

$$\begin{aligned} \Sigma'_i &= \det\begin{bmatrix} S'_p & \partial_j S'_p & \partial_k S'_p \\ S'_q & \partial_j S'_q & \partial_k S'_q \\ S'_r & \partial_j S'_r & \partial_k S'_r \end{bmatrix} \\ &= \det\left(\begin{bmatrix} R_{11} & R_{12} & R_{13} \\ R_{21} & R_{22} & R_{23} \\ R_{31} & R_{32} & R_{33} \end{bmatrix}\begin{bmatrix} S_p & \partial_j S_p & \partial_k S_p \\ S_q & \partial_j S_q & \partial_k S_q \\ S_r & \partial_j S_r & \partial_k S_r \end{bmatrix}\right) \\ &= \det\left(\begin{bmatrix} S_p & \partial_j S_p & \partial_k S_p \\ S_q & \partial_j S_q & \partial_k S_q \\ S_r & \partial_j S_r & \partial_k S_r \end{bmatrix}\right) = \Sigma_i. \end{aligned} \tag{5.5}$$

Going from the second to third row we have used the fact that determinants are multiplicative, and that $\det\mathbb{R} = 1$, thus we proved that Σ'_i has the same value as Σ_i.

An argument that one may have here is that a matrix can be viewed as a rank 2 tensor, and a rank 2 tensor would be rotated as $\mathbb{R}\mathbf{M}\mathbb{R}^T$. To understand this we can think about the skyrmion field, being a triple product, as a volume of a parallelepiped, as in Figure. 5.1. To rotate a volume, one would want to rotate all three vectors which determines the volume together, which means that for the rotated volume, we write

$$\begin{aligned} V &= \det\left[\mathbb{R}\begin{bmatrix} S_p \\ S_q \\ S_r \end{bmatrix} \quad \mathbb{R}\begin{bmatrix} \partial_j S_p \\ \partial_j S_q \\ \partial_j S_r \end{bmatrix} \quad \mathbb{R}\begin{bmatrix} \partial_k S_p \\ \partial_k S_q \\ \partial_k S_r \end{bmatrix}\right] \\ &= \det\left[\mathbb{R}\mathbf{M}_s\right]. \end{aligned} \tag{5.6}$$

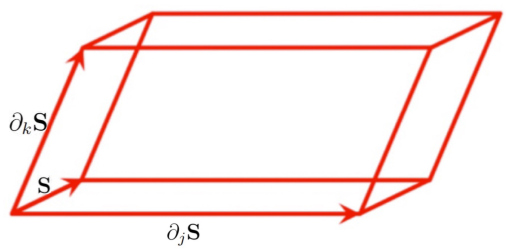

Figure 5.1: Volume of a parallelepiped representing the skyrmion field. It is easy to understand that a volume is unchanged under a rigid rotation, and so as the skyrmion field.

This volume also helps understanding the invariance of a skyrmion field under basis change, as this basis change corresponds to a rigid rotation of the parallelepiped which keeps its volume.

There is an implicit condition in the above statement: all quantities are calculated in a consistent Schmidt basis. More explicitly, the claim assumes that the Stokes parameters are evaluated in the same orthonormal basis in which the skyrmion field was constructed. This is intuitive, as a change of basis is equivalent to a rotation of the Poincaré sphere, which does not alter the skyrmion pattern or the nature of the projection.

5.3 Skyrmion Fields in Mixed-up Bases Measurements

Paraxial light with spatially varying polarizations underpins many recent developments in the field of structured light. Such structured light can be decomposed into fundamental beam modes, whether as a physical quantity in the lab, or as a mathematical object, and they can be expressed by any suitable basis. In previously developed theory, we have used a consistent basis throughout the calculation of skyrmion numbers, characterizing its geometrical properties, and its propagating dynamics. This, however, is not a necessary requirement, and may not provide the best accuracy in experimental evaluations, as we shall see in the following. In this section, we demonstrate how a skyrmion field can be constructed and measured in different bases and prove that the skyrmion number is unchanged under such manipulations.

We begin by introducing a skyrmion field, as

$$|\psi(\mathbf{r})\rangle = \frac{|H\rangle + \mu|V\rangle}{\sqrt{1+|\mu|^2}}, \tag{5.7}$$

where we have substituted the general orthonormal basis $|0\rangle$ and $|1\rangle$ in Eq. (4.3) with a specific basis. In this case, we designate $|H\rangle$ and $|V\rangle$ as the basis used to construct the skyrmion field. Now, we use $|R\rangle$ and $|L\rangle$ to construct the Pauli matrices as follows

$$\begin{aligned} \sigma_x &= |R\rangle\langle L| + |L\rangle\langle R|, \\ \sigma_y &= i(|L\rangle\langle R| - |R\rangle\langle L|), \\ \sigma_z &= |R\rangle\langle R| - |L\rangle\langle L|. \end{aligned} \tag{5.8}$$

Before we continue, we would like to clarify the meaning of the different types of indices used in this thesis. We will use indices 1, 2, 3 for fixed-value Pauli matrices, which are defined as follows

$$\begin{aligned} \sigma_1 &= \begin{pmatrix} 0 & 1 \\ 1 & 0 \end{pmatrix}, \\ \sigma_2 &= \begin{pmatrix} 0 & -i \\ i & 0 \end{pmatrix}, \\ \sigma_3 &= \begin{pmatrix} 1 & 0 \\ 0 & -1 \end{pmatrix}. \end{aligned} \tag{5.9}$$

These are the conventional Pauli matrices which people are most familiar with. The Pauli matrices we defined in Eq. (5.8) can be linked with the conventional Pauli matrices by some rotational matrix as $[\sigma_x, \sigma_y, \sigma_z]^T = \mathbb{R}\,[\sigma_1, \sigma_2, \sigma_3]$, where the alphabetic indices x, y, z refer to rotated Pauli matrices. The relations between the Pauli matrices constructed from three commonly used orthonormal pairs and the conventional Pauli matrices are shown in Table. 5.1. The generalized Pauli matrices regarding arbitrary basis will be discussed in later sections, but the Pauli matrices presented in the table are most relevant to the experiments. Note that, in this table, we have used a modified $|D\rangle, |A\rangle$ basis, the relation between this modified basis and the conventional one is by a unitary transformation, as

$$U = \frac{1}{\sqrt{2}} \begin{pmatrix} 1 & 1 \\ i & -i \end{pmatrix}. \tag{5.10}$$

The modified $|D\rangle, |A\rangle$ basis under this unitary transformation can be calculated as

$$\begin{aligned} |D\rangle &= \frac{1+i}{2} \begin{pmatrix} 1 \\ 1 \end{pmatrix}, \\ |A\rangle &= \frac{1-i}{2} \begin{pmatrix} 1 \\ -1 \end{pmatrix}. \end{aligned} \tag{5.11}$$

This modified basis guarantees a straightforward permutation relation. It is equivalently valid if we use the conventional $|D\rangle, |A\rangle$ basis, which would give the relation as $[\sigma_x, \sigma_y, \sigma_z] = [\sigma_3, -\sigma_2, \sigma_1]$, while the modified $|D\rangle, |A\rangle$ basis would give us $[\sigma_x, \sigma_y, \sigma_z] = [\sigma_2, \sigma_3, \sigma_1]$. Note that the two bases differ by a global phase factor, which does not alter the polarization and has no effect on the experiment. We introduce it here solely for notational convenience.

Table 5.1: Pauli matrices for the three commonly used orthonormal bases.

	HV	RL	DA (modified)
σ_x	σ_1	σ_3	σ_2
σ_y	σ_2	σ_1	σ_3
σ_z	σ_3	σ_2	σ_1

Now we get back to our main theme of this section of exploring the properties of a skyrmion field under a mixed-up bases measurement. Using the notation we defined above, we can write a generalized skyrmion field as

$$\begin{aligned} \Sigma_i = S_x \left(\frac{\partial S_y}{\partial x_j} \frac{\partial S_z}{\partial x_k} - \frac{\partial S_z}{\partial x_j} \frac{\partial S_y}{\partial x_k} \right) + S_y \left(\frac{\partial S_z}{\partial x_j} \frac{\partial S_x}{\partial x_k} - \frac{\partial S_x}{\partial x_j} \frac{\partial S_z}{\partial x_k} \right) \\ + S_z \left(\frac{\partial S_x}{\partial x_j} \frac{\partial S_y}{\partial x_k} - \frac{\partial S_y}{\partial x_j} \frac{\partial S_x}{\partial x_k} \right), \end{aligned} \tag{5.12}$$

where the alphabetic indices x, y, z are for the Stokes parameters calculated under mixed-up bases measurements. To prove that the properties of a skyrmion field is unchanged in such measurements, we calculate the relation between the generalized Stokes parameters, and the conventional Stokes parameters. Without loss of generality, we have our specifications of states as in Eq. (5.7) and Eq. (5.8), this specification of mixed-up bases measurements pins up components of our rotated Pauli matrices. From Table. 5.1 we know the relation is $[\sigma_x, \sigma_y, \sigma_z] = [\sigma_3, \sigma_1, \sigma_2]$.

Accordingly, we can calculate the components of Stokes vector for this specification from Eq. (4.6) as

$$\mathbf{S}' = (S_x, S_y, S_z) = (S_3, S_1, S_2). \tag{5.13}$$

For such specification, the skyrmion field under this mixed-up bases measurement can be found by substituting Eq. (5.13) into Eq. (5.12) as

$$\begin{aligned}\Sigma_i =& S_3 \left(\frac{\partial S_1}{\partial x_j}\frac{\partial S_2}{\partial x_k} - \frac{\partial S_2}{\partial x_j}\frac{\partial S_1}{\partial x_k}\right) + S_1 \left(\frac{\partial S_2}{\partial x_j}\frac{\partial S_3}{\partial x_k} - \frac{\partial S_3}{\partial x_j}\frac{\partial S_2}{\partial x_k}\right) + \\ & S_2 \left(\frac{\partial S_3}{\partial x_j}\frac{\partial S_1}{\partial x_k} - \frac{\partial S_1}{\partial x_j}\frac{\partial S_3}{\partial x_k}\right).\end{aligned} \tag{5.14}$$

We also write out Eq. (4.11) for consistent basis measurement explicitly, where $\mathbf{S}$ in its component form is $\mathbf{S}$=(S_1, S_2, S_3), as

$$\begin{aligned}\Sigma_i =& \frac{1}{2}\varepsilon_{ijk}\mathbf{S} \cdot \left(\frac{\partial \mathbf{S}}{\partial x_j} \times \frac{\partial \mathbf{S}}{\partial x_k}\right) \\ =& S_1 \left(\frac{\partial S_2}{\partial x_j}\frac{\partial S_3}{\partial x_k} - \frac{\partial S_3}{\partial x_j}\frac{\partial S_2}{\partial x_k}\right) + S_2 \left(\frac{\partial S_3}{\partial x_j}\frac{\partial S_1}{\partial x_k} - \frac{\partial S_1}{\partial x_j}\frac{\partial S_3}{\partial x_k}\right) + \\ & S_3 \left(\frac{\partial S_1}{\partial x_j}\frac{\partial S_2}{\partial x_k} - \frac{\partial S_2}{\partial x_j}\frac{\partial S_1}{\partial x_k}\right).\end{aligned} \tag{5.15}$$

We notice immediately that the result of Eq. (5.14) is nothing but a cyclic permutation of Eq. (5.15). Therefore, we proved that the expression of the skyrmion field is unchanged for a mixed-up bases measurement, which is not obvious from first sight as $\mathbf{S}$ is altered under basis change.

For convenience, we present the relations between the generalized Stokes vector under the three common mixed-up bases measurements and the consistent bases measurements, as in Table. 5.2.

Table 5.2: Stokes parameters for each possible mix-up with RL bases, where the Pauli matrices are constructed using the RL basis, and the skyrmion beam is constructed in HV, RL and DA bases, respectively.

	HV&RL	RL&RL	DA(modified)&RL
S_x	S_3	S_1	S_2
S_y	S_1	S_2	S_3
S_z	S_2	S_3	S_1

From a geometrical point of view, when using consistent basis measurements, the coordinate system of the parameter space and the Stokes vector always rotate in the same way, therefore the components of the Stokes vector always stay the same, as $(S_x, S_y, S_z) = (S_1, S_2, S_3)$, as shown in Figure. 5.2. We will talk more about the geometrical interpretation in subsection 5.6.2.

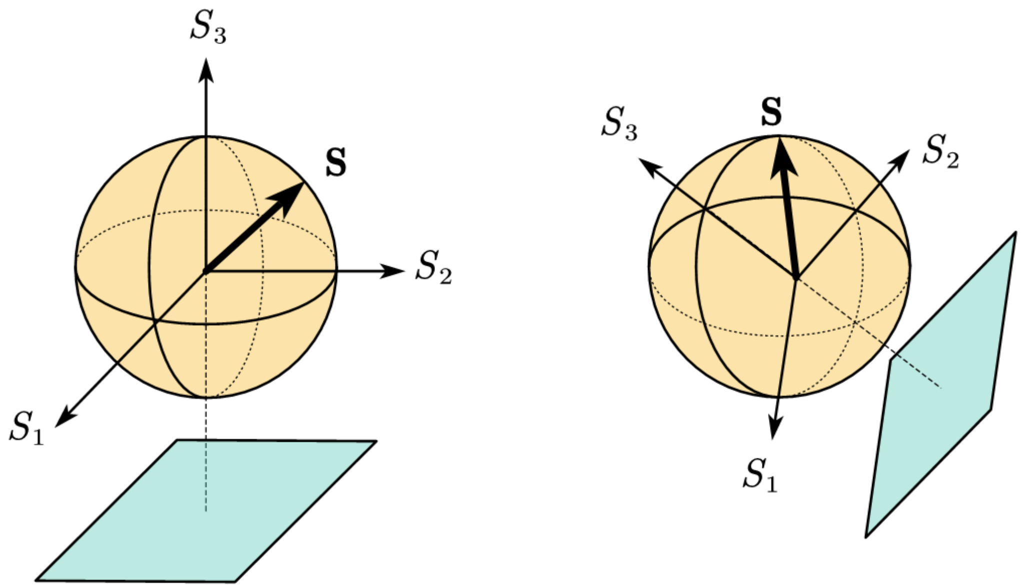

Figure 5.2: On the left is the fixed-value case, which corresponds to unrotated Poincaré sphere, and is one special case of consistent Schmidt bases (right). On the right is a representation of the consistent Schmidt bases, which corresponds to a consistent rotation of both the Poincaré sphere and the Stokes' vector $\mathbf{S}$.

The result that the properties of the skyrmion field is unchanged under mixed-up bases measurement is not as trivial as it might seem. Shen pointed out in his paper that a new type of field with topological significance, the optical bimeron, which is a topological transition of skyrmion, can be constructed with suitable states different from that of a skyrmion [125]. Our mixed-up bases measurements, however, has the power to generate bimeronic structures without changing the original construction of the field: while the underlying skyrmion field remains unchanged, the observable topological structure that emerges can depend on the basis used for measurement. This is why we refer to them as different *measurements* rather than different constructions. The field is the same, but the observed topology shifts due to measurement basis, a concept that will be clarified with specific examples and visualizations in the following sections. In later sections we will propose a more intuitive projection which extends the concepts of singularities in terms of Stokes phase which benefit measurements in our experiment. This result also has no conflict with our intuition as we do not need to know in which basis the skyrmion field is prepared in order to measure the skyrmion number.

5.4 Skyrmion Potential in Mixed-up Bases Measurements

As we mentioned in section 5.3, a second method of calculating the skyrmion number is by the means of a line integration over the vector potential of the skyrmion field, which can eventually lead to the most sophisticated third method of calculating skyrmion number by the topological winding numbers and a phase defined with respect to complex Stokes parameters. We now calculate the form of the vector potential for mixed-up bases measurements, as specified in Eq. (5.7) and Eq. (5.8), again without loss of generality. This specification yields the Stokes vector of its component form, $\mathbf{S}' = (S_3, S_1, S_2)$, as shown in Eq. (5.13). From this, we can find $\mathbf{m}'$ and $\mathbf{n}'$ relative to $\mathbf{S}'$ as

$$\begin{aligned}
\mathbf{m}' &= \frac{1}{\sqrt{S_x^2 + S_y^2}} \left(S_y \hat{\mathbf{x}} - S_x \hat{\mathbf{y}} \right) \\
&= \frac{1}{\sqrt{S_3^2 + S_1^2}} \left(S_1 \hat{\mathbf{x}} - S_3 \hat{\mathbf{y}} \right), \\
\mathbf{n}' &= \frac{1}{\sqrt{S_x^2 + S_y^2}} \left[-S_z S_x \hat{\mathbf{x}} - S_z S_y \hat{\mathbf{y}} + \left(S_x^2 + S_y^2 \right) \hat{\mathbf{z}} \right] \\
&= \frac{1}{\sqrt{S_3^2 + S_1^2}} \left[-S_2 S_3 \hat{\mathbf{x}} - S_2 S_1 \hat{\mathbf{y}} + \left(S_3^2 + S_1^2 \right) \hat{\mathbf{z}} \right].
\end{aligned} \tag{5.16}$$

We can construct the vector potential from $\mathbf{m}'$ and $\mathbf{n}'$ for this the mixed-up bases measurement using the Mermin-Ho relation [121]

$$v_i' = \frac{S_2}{S_3^2 + S_1^2} \left(S_1 \frac{\partial}{\partial x_i} S_3 - S_3 \frac{\partial}{\partial x_i} S_1 \right). \tag{5.17}$$

We have the skyrmion potential in consistent basis measurements calculated in Eq. (4.19). If we plug in the relation $(S_x, S_y, S_z) = (S_1, S_2, S_3)$ for consistent basis measurements, we can write Eq. (4.19) as

$$\begin{aligned}
v_i &= \frac{S_z}{S_x^2 + S_y^2} \left(S_y \frac{\partial}{\partial x_i} S_x - S_x \frac{\partial}{\partial x_i} S_y \right) \\
&= \frac{S_3}{S_1^2 + S_2^2} \left(S_2 \frac{\partial}{\partial x_i} S_1 - S_1 \frac{\partial}{\partial x_i} S_2 \right).
\end{aligned} \tag{5.18}$$

If we recall the values of $S_{1,2,3}$ obtained in Eq. (4.8), we can easily calculate that the vector potential in this mixed-up bases measurement differs from that in a consistent basis measurement. That is to say, unlike the skyrmion field, the skyrmion vector potential does change under mixed-up bases measurements. However, this change would not affect the calculation of the skyrmion number, as the curl relation between the vector potential and the skyrmion field remains valid. Furthermore, this change in the vector potential can be understood as a gauge difference. We will prove in the following that this is true.

The curl relation we want to prove can be written in its component form, as

$$\mathbf{\Sigma}_i = \left(\nabla \times \mathbf{v}\right)_i . \tag{5.19}$$

The general expression of the vector potential in its component form is

$$v_k = \frac{S_z}{S_x^2 + S_y^2}\left(S_y \frac{\partial}{\partial x_i} S_x - S_x \frac{\partial}{\partial x_i} S_y\right), \tag{5.20}$$

which is the same as Eq. (5.18) because i and k are both dummy indices. In the expression, x, y, z can be any cyclic permutation of $1, 2, 3$.

We expand the right hand side of Eq. (5.19), substitute Eq. (5.20) into it, and we get

$$\begin{aligned}
\left(\nabla \times \mathbf{v}\right)_i =& \varepsilon_{ijk}\partial_j v_k \\
=& \partial_j v_k - \partial_k v_j \\
=& \frac{\partial_j S_x \cdot \left(S_y \partial_k S_z - S_z \partial_k S_y\right)}{S_y^2 + S_z^2} - \frac{\partial_k S_x \cdot \left(S_y \partial_j S_z - S_z \partial_j S_y\right)}{S_y^2 + S_z^2} \\
=& \left(S_y \frac{\partial S_y}{\partial x_j}\frac{\partial S_z}{\partial x_k} - S_y \frac{\partial S_x}{\partial x_j}\frac{\partial S_z}{\partial x_k}\right) + \left(S_z \frac{\partial S_x}{\partial x_j}\frac{\partial S_y}{\partial x_k} - S_z \frac{\partial S_y}{\partial x_j}\frac{\partial S_x}{\partial x_k}\right) + \\
& \left(S_x \frac{\partial S_y}{\partial x_j}\frac{\partial S_z}{\partial x_k} - S_x \frac{\partial S_z}{\partial x_j}\frac{\partial S_y}{\partial x_k}\right).
\end{aligned} \tag{5.21}$$

It is not difficult to identify that Eq. (5.21) will be one permuted form of Eq. (5.14). Therefore, the curl relation between the vector potential and the skyrmion field in a generalized measurement still holds. Which means potentially, there could be many different vector potentials, obtained from different basis measurements, associated with one skyrmion field.

5.5 General Orthonormal States and Their Pauli Matrices

Before we step any further into the mixed-up bases measurements, it is a good point to take a pause and talk about general orthonormal states and how their relevant Pauli matrices are constructed, as an extension to the comments we had about the relations between the Stokes parameters calculated from rotated Pauli matrices and the conventional Pauli matrices. We will use $|\varphi_1\rangle$ and $|\varphi_2\rangle$ for a general pair of orthonormal states.

To begin, we construct general orthonormal polarization states $|\varphi_1\rangle$, $|\varphi_2\rangle$ in terms of spherical polar coordinates (γ, θ), which represent angles on the Poincaré sphere, and the left- and right-handed circular polarizations, as

$$\begin{aligned} |\varphi_1\rangle &= \cos\left(\frac{\gamma}{2}\right)|R\rangle + e^{-i\theta}\sin\left(\frac{\gamma}{2}\right)|L\rangle, \\ |\varphi_2\rangle &= -\sin\left(\frac{\gamma}{2}\right)|R\rangle + e^{-i\theta}\cos\left(\frac{\gamma}{2}\right)|L\rangle. \end{aligned} \tag{5.22}$$

where the geometrical meaning of γ and θ are the azimuthal and polar angles of the sphere respectively, as defined in Figure. 5.3.

The reason we have used $\frac{\gamma}{2}$ instead of γ is because this definition would match the geometry of the Poincaré sphere. This definition is analogous to the general orthonormal states on the Bloch sphere. However, one should notice that the Poincaré sphere and the Bloch sphere typically follow different handedness conventions, as one can find in standard textbooks, e.g., [76, 6]. The Poincaré sphere, defined with inverse handedness, can also be found, for example, in [126], where linearly polarized light transitions from horizontal to anti-diagonal instead of diagonal polarization. Nevertheless, we define the above general orthonormal states according to the convention used in [6], therefore we have defined the exponential terms as $-i\theta$ instead of $i\theta$.

From this definition, we know that the three commonly used orthonormal bases mentioned earlier are simply special cases of this general orthonormal basis, such that the general form would reduce to the special cases with appropriate choice of angles. Namely, if we take $(\gamma, \theta) = (0, 0)$, we would get $|\varphi_1\rangle, |\varphi_2\rangle \to |R\rangle, |L\rangle$. Likewise, for $(\gamma, \theta) = (\pi/2, 0)$, we would get $|\varphi_1\rangle, |\varphi_2\rangle \to |H\rangle, |V\rangle$, and for $(\gamma, \theta) = (\pi/2, \pi/2)$, we would get $|\varphi_1\rangle, |\varphi_2\rangle \to |D\rangle, |A\rangle$.

Note that in the above context, we have used the conventional diagonal and

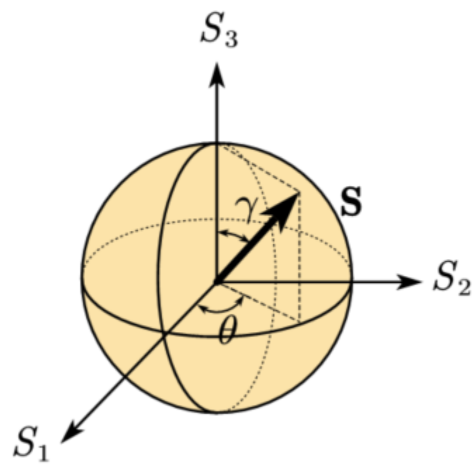

Figure 5.3: Parameters of the Poincaré sphere.

anti-diagonal polarizations, as

$$\begin{aligned} |D\rangle &= \frac{1}{\sqrt{2}}\begin{pmatrix} 1 \\ 1 \end{pmatrix}, \\ |A\rangle &= \frac{1}{\sqrt{2}}\begin{pmatrix} 1 \\ -1 \end{pmatrix}. \end{aligned} \tag{5.23}$$

We can thus construct generalized Pauli matrices similar to those in Eq. (4.7), by replacing $|0\rangle, |1\rangle$ with $|\varphi_1\rangle, |\varphi_2\rangle$, as

$$\begin{aligned} \sigma_x &= |\varphi_1\rangle\langle\varphi_2| + |\varphi_2\rangle\langle\varphi_1| \\ &= \begin{pmatrix} 0 & -i\sin\gamma \\ i\sin\gamma & 0 \end{pmatrix} + \cos\gamma \begin{pmatrix} \cos\theta & \sin\theta \\ \sin\theta & -\cos\theta \end{pmatrix}, \\ \sigma_y &= i(|\varphi_2\rangle\langle\varphi_1| - |\varphi_1\rangle\langle\varphi_2|) \\ &= \begin{pmatrix} \sin\theta & -\cos\theta \\ -\cos\theta & -\sin\theta \end{pmatrix}, \\ \sigma_z &= |\varphi_1\rangle\langle\varphi_1| - |\varphi_2\rangle\langle\varphi_2| \\ &= \begin{pmatrix} 0 & i\cos\gamma \\ -i\cos\gamma & 0 \end{pmatrix} + \sin\gamma \begin{pmatrix} \cos\theta & \sin\theta \\ \sin\theta & -\cos\theta \end{pmatrix}. \end{aligned} \tag{5.24}$$

Eq. (5.24) is a generalization of Table. 5.1, from which a continuous rotation of the measurement at arbitrary angles is possible. The results from section 5.3 tell us that skyrmion fields can have quite robust properties. While these fields are solely determined by Stokes parameters, and the three Stokes parameters should be of equivalent importance, this inspired us that this is the way to generalize the measurements. In the next section, we will discuss how this framework would allow us to calculate generalized Stokes parameters, which are direct results of generalized measurements.

5.6 One Skyrmion Beam and Its Countless Topological Equivalents

In this section, we explore how different textures can be generated from a single skyrmion field using generalized measurements. The skyrmion field itself is constructed in a fixed basis $|L\rangle$ and $|R\rangle$, which remains unchanged throughout. We then introduce generalized polarization states to construct a new set of Pauli matrices, enabling the evaluation of Stokes parameters in an generalized measurement. This naturally leads to the geometrical equivalence of these patterns and a generalization of the concept of singularities, extending beyond C-points to include any possible polarization. We first establish the mathematical framework in subsection 5.6.1, where we calculate generalized Stokes parameters for a fixed skyrmion field. In subsection 5.6.2, we introduce the concept of rational maps, which gives us geometrical interpretations of the change of measurement basis, leading to the generalization of singularities in subsection 5.6.3. Finally, in subsection 5.6.4, we plot a series of examples of patterns generated from generalized measurements on bases rotated at different angles.

5.6.1 Fixed Skyrmion Beam and Generalized Stokes Parameters

We begin by constructing a skyrmion beam with a fixed basis and examining the form of its parameters under generalized measurements. Consider a skyrmion beam of the form

$$\begin{aligned} |\psi(\mathbf{r})\rangle &= \frac{1}{\sqrt{2}}\left(\mathrm{LG}_0^{\ell_0}|0\rangle + e^{i\Theta}\mathrm{LG}_0^{\ell_1}|1\rangle\right) \\ &= \frac{|0\rangle + \mu(\mathbf{r})|1\rangle}{\sqrt{1+|\mu(\mathbf{r})|^2}}, \end{aligned} \tag{5.25}$$

as we introduced in Eq. (4.2). Setting $\ell_0 = 0$, $\ell_1 = +1$, $|0\rangle = |L\rangle, |1\rangle = |R\rangle, \Theta = 0$ produces a Néel-type skyrmion of skyrmion number $n = 1$ [127, 128]. In other words, the construction of the skyrmion field is fixed by choosing the orthonormal basis of construction to be $|L\rangle$ and $|R\rangle$. We now calculate the generalized Stokes parameters using the generalized Pauli matrices we derived in Eq. (5.24).

Substituting Eq. (5.24) into $\mathbf{S} = \langle\psi(\mathbf{r})|\boldsymbol{\sigma}|\psi(\mathbf{r})\rangle$, we obtain

$$\begin{aligned}
S_x &= \langle\psi|\sigma_x|\psi\rangle \\
&= \frac{1}{2}\frac{1}{1+|\mu|^2}\times \\
&\quad \begin{pmatrix} 1+\mu^* & i\,(1-\mu^*) \end{pmatrix} \begin{pmatrix} \cos\gamma\cos\theta & -i\sin\gamma+\sin\theta\cos\gamma \\ i\sin\gamma+\sin\theta\cos\gamma & -\cos\theta\cos\gamma \end{pmatrix} \begin{pmatrix} 1+\mu \\ -i\,(1-\mu) \end{pmatrix} \\
&= \frac{1}{1+|\mu|^2}\left[2\Re(\mu)\cdot\cos\gamma\cos\theta - \left(1-|\mu|^2\right)\sin\gamma - 2\Im(\mu)\cdot\sin\theta\cos\gamma\right].
\end{aligned} \tag{5.26}$$

With similar reasoning, we can calculate S_y and S_z as

$$S_y = \frac{1}{1+|\mu|^2}\left[2\Re(\mu)\sin\theta + 2\Im(\mu)\cos\theta\right], \tag{5.27}$$

$$S_z = \frac{1}{1+|\mu|^2}\left[2\Re(\mu)\sin\gamma\cos\theta + \left(1-|\mu|^2\right)\cos\gamma - 2\Im(\mu)\cdot\sin\gamma\sin\theta\right]. \tag{5.28}$$

We identify here that these generalized parameters are related to the conventional Stokes parameters, which were given in Eq. (4.8), Eq. (4.9) and Eq. (4.10)

$$S_1 = \frac{2\Re(\mu)}{1+|\mu|^2}, \quad S_2 = \frac{2\Im(\mu)}{1+|\mu|^2}, \quad S_3 = \frac{1-|\mu|^2}{1+|\mu|^2}. \tag{5.29}$$

These conventional parameters correspond to the choices $\gamma = 0$ and $\theta = 0$ in Eq. (5.26), Eq. (5.27) and Eq. (5.28). Consequently, the generalized parameters can be expressed in terms of the conventional Stokes parameters as

$$S_x = \cos\gamma\cos\theta S_1 - \sin\gamma S_3 - \sin\theta\cos\gamma S_2, \tag{5.30}$$

$$S_y = \sin\theta S_1 + \cos\theta S_2, \tag{5.31}$$

$$S_z = \sin\gamma\cos\theta S_1 + \cos\gamma S_3 - \sin\gamma\sin\theta S_2. \tag{5.32}$$

This way, we measured the skyrmion beam, constructed in $|L\rangle$, $|R\rangle$ basis, in a completely arbitrary basis, and the measurement results are these generalized Stokes parameters. One can verify these generalized components still keeps the unity of $\mathbf{S}$, such that $|\mathbf{S}| = 1$, as

$$\begin{aligned}
&S_x^2 + S_y^2 + S_z^2 \\
&= (\cos\gamma\cos\theta S_1 - \sin\gamma S_3 - \sin\theta\cos\gamma S_2)^2 + (\sin\theta S_1 + \cos\theta S_2)^2 + \\
&\quad (\sin\gamma\cos\theta S_1 + \cos\gamma S_3 - \sin\gamma\sin\theta S_2)^2 \\
&= \cos^2\theta S_1^2 - 2\cos\theta\sin\theta S_1 S_2 + S_3^2 + \sin^2\theta S_2^2 + \sin^2\theta S_1^2 + 2\sin\theta\cos\theta S_1 S_2 + \cos^2\theta S_2^2 \\
&= \left(\cos^2\theta S_1^2 + \sin^2\theta S_1^2\right) + \left(\sin^2\theta S_2^2 + \cos^2\theta S_2^2\right) + S_3^2 \\
&= S_1^2 + S_2^2 + S_3^2
\end{aligned} \tag{5.33}$$

This enables us to produce equivalent skyrmion potentials for a single skyrmion field simply by choosing different bases $|\varphi\rangle, |\varphi_2\rangle$ in σ_i, as given in Figure 5.4. This means that, the Stokes phase Φ (see Eq. (4.21)) are not necessarily $\arctan\frac{S_2}{S_1}$. Different forms of Stokes phases can be obtained in different measurements, therefore identify different singularities. We will discuss more about the generalized singularities in the following sections.

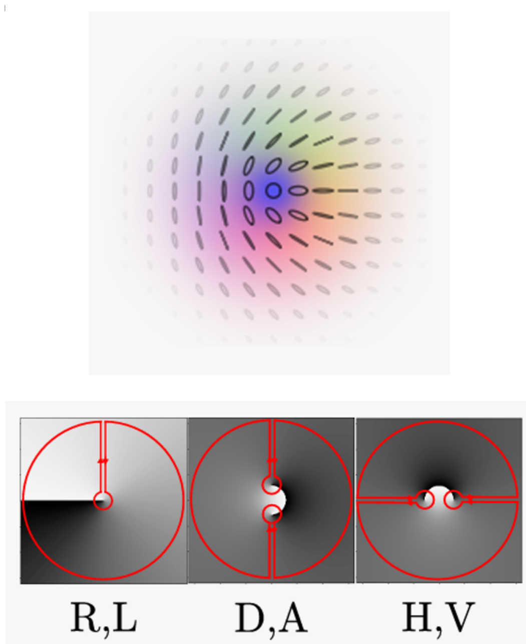

Figure 5.4: Equivalent Φ plots for a $n = 1$ Néel type skyrmion (Eq. (5.25)). With phase plots generated by identifying different singularities in different measurements, the measurement bases are indicated in the labels under the phase plots.

5.6.2 Rational Map and Geometrical interpretations

We now introduce the idea of rational maps and investigate how this idea can be applied to optical skyrmions.

Rational maps were first proposed by Houghton et al. in [129] for the purpose of finding approximate solutions for Skyrme's field equation, which is not integrable. This method is accurate especially for skyrmion fields with low topological numbers [130]. Using rational maps for constructing optical skyrmions offers several advantages: they help us to distinguish intrinsic topological features from beam characteristics influenced by experimental implementation, provide a framework for designing new optical skyrmion fields, and establish a foundation for exploring the distinctions between optical skyrmion fields and their magnetic counterparts [127].

As a mathematical object, the paraxial skyrmion field is a mapping from the plane to the sphere. The idea of rational maps requires that the plane of the beam profile be mapped to a unit sphere Σ and then mapped onto the Poincaré sphere. Different types of skyrmions can therefore be constructed from different mapping functions, which are referred to as rational maps. This construction is conceptually motivated by the *baby skyrmion model* [127], a simplified two-dimensional topological field theory originally developed to study skyrmions in reduced dimensions, which is widely used in the condensed matter community [131] and particle theory [132]. In the optical context, it provides an intuitive picture of how spatially varying polarization fields can inherit the topological structure.

To be brief, paraxial skyrmions are therefore constructed according to a two-step process: the set of unitary Stokes vectors $\mathbf{S} = (S_1, S_2, S_3)$ uniquely identifying fully polarized states of light is first anchored into a three-dimensional physical space [127] (step 1 in figure 5.5). This process associates one polarization state with each point $\mathbf{r} = (x, y, z)$ on S^2. It is possible, however not essential, to picture these polarization states as unitary vectors $\mathbf{S}'(\mathbf{r}) = (S_x(\mathbf{r}), S_y(\mathbf{r}), S_z(\mathbf{r}))$ in $\mathbb{R}^3$ to enable comparisons with condensed matter skyrmions. Each $\mathbf{r}$, along with its polarization state, is then mapped into the plane transverse to the propagation direction of light, $\mathbb{R}^2$, using a stereographic projection (step 2 in figure 5.5). This produces a spatially varying polarization distribution, which can be visualized either as a distribution of $\mathbf{S}'(\mathbf{r})$ or as a distribution of polarization ellipses.

For our construction, we have a fixed S^2 sphere and a rotating Poincaré sphere. The stereographic projection axis is always aligned with the z-axis of the S^2 sphere, which is fixed. Different measurements correspond to different alignments between the Poincaré sphere and the S^2 sphere. In a generalized measurement, as constructed in Eq. (5.24), we align $|\varphi\rangle$ with the z-axis of the S^2 sphere. This alignment determines the resulting pattern and the corresponding singularities. Specific examples of axis alignments will be given in subsection 5.6.3.

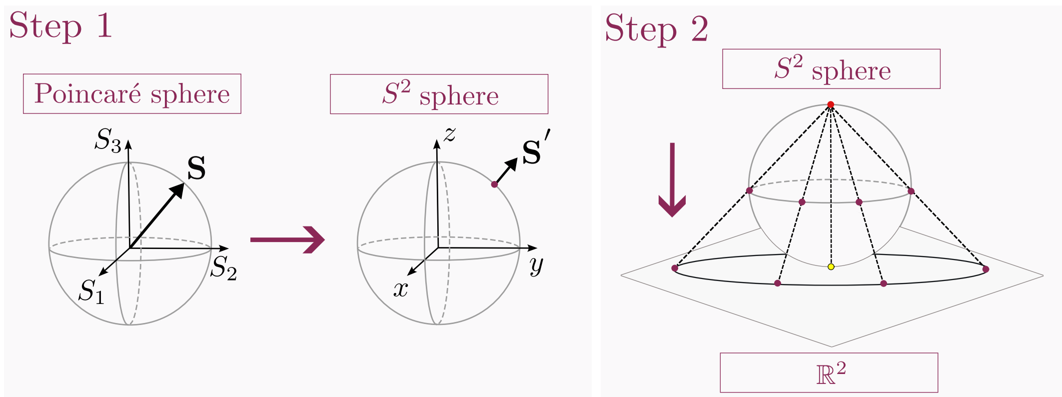

Figure 5.5: Baby skyrmion model applied to optical paraxial skyrmions. In step 1, unitary stokes vectors $\mathbf{S} = (S_1, S_2, S_3)$ embedded in the abstract space of the Poincaré sphere, are anchored into $\mathbb{R}^3$ yielding $\mathbf{S}'(\mathbf{r}) = (S_x(\mathbf{r}), S_y(\mathbf{r}), S_z(\mathbf{r}))$ according to topological considerations outlined in [127]. In step 2, S^2 is mapped into $\mathbb{R}^2$ using a stereographic projection. Here, the north pole is the projection point by which points $\mathbf{r}$ on S^2 are imaged onto $\mathbb{R}^2$. The imaging process is illustrated for a selection of points on the equator. The south pole is imaged as the origin of $\mathbb{R}^2$ whereas the north pole is imaged at spatial infinity.

5.6.3 Generalized Singularities

As we mentioned in subsection 5.6.1, different measurements yield different vector potentials, and consequently different Stokes phases which generalize the concept of singularities. Conventionally, polarization singularities always refer to circular polarizations, where the ellipticity is undefined. This is because the complex Stokes parameter is defined as $S_\pm = S_x \pm iS_y$, as given in Eq. (4.20), which is in the context of consistent basis measurements. Thus, $S_\pm = S_1 \pm iS_2$, and the phase takes the form $\Phi = \arctan(S_2/S_1)$, which is directly related to the ellipticity. In a generalized measurement, however, S_x and S_y take the form of Eq. (5.30) and Eq. (5.31), therefore the singularities are not limited to circular polarizations. In the generalized context, singularities arise when S_y and S_x are both 0. If $(\gamma, \theta) = (0, 0)$, we can calculate $S_x = S_1, S_y = S_2, S_z = S_3$, and Φ is singular when $S_2 = S_1 = 0$, which corresponds to C-points, that is, right-handed and left-handed circularly polarized light (R, L plots in Figure 5.6). Similarly, if $(\gamma, \theta) = (-\pi/2, \pi/2)$, we have $S_x = S_3, S_y = S_1, S_z = S_2$, the phase singularities are diagonal and anti-diagonal linearly polarized light (D,A plots in Figure 5.6) whereas choosing $(\gamma, \theta) = (\pi/2, 0)$ gives $S_x = -S_3, S_y = S_2, S_z = S_1$ corresponding to horizontal and vertical linear polarization states (H,V plots in Figure 5.6). Of course, there are countless formalisms not limited to what we listed above, where we can appoint any arbitrary polarizations as singularities, as will be given in Figure. 5.7 in subsection 5.6.4.

The choice of triad $\mathbf{S}(\mathbf{r})$ for $\mathbf{S}'(\mathbf{r})$ therefore singles out a pair of orthogonal polarization states to act as phase singularities for Φ. These singularities will occupy different positions within the beam profile but cannot be eliminated in analogy to Dirac strings in the theory of magnetic monopoles [133]. Targeting singularities located in regions of low noise is a strategic choice advantageous for experimental measurements of the skyrmion number, as demonstrated in [120].

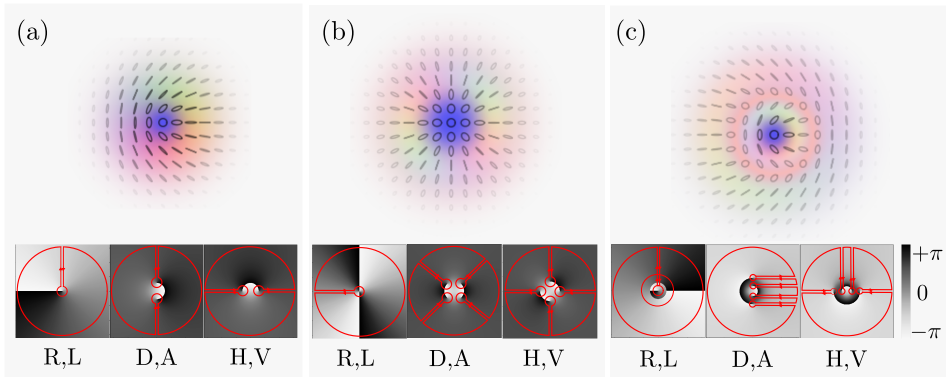

Figure 5.6: Intensity-modulated polarization distributions for (a) a $n = 1$ and (b) a $n = 2$ Néel-type skyrmion and (c) a general Poincaré beam ($n = 0$). Three equivalent Φ plots are provided for each polarization distribution, targeting right and left handed circularly polarized light (R,L), diagonal and antidiagonal linearly polarized light (D,A) and horizontally and vertically polarized light (H,V) as phase singularities. Integration contours regarding equation 4.17 are indicated in red.

5.6.4 Generalized Skyrmion Textures

While Néel-type skyrmions can be regarded as the most fundamental optical skyrmionic structures, one can build an entire atlas of optical skyrmions, encompassing bimerons and Bloch-type skyrmions, by making use of rotations [127, 134]. These do not affect the coverage of the Poincaré sphere, hence the skyrmion number, but change the polarization distribution of the beam. Indeed, countless skyrmion structures, all having the same skyrmion number, can be obtained by rotating either the local polarization vectors $\mathbf{S}(\mathbf{r})$ or by rotating S^2 [127]. In equation 5.25, this freedom is reflected in the choice of polarization states for the orthonormal basis and in the choice of Θ. We show in Figure 5.7 and Figure 5.8 examples of topologically equivalent optical skyrmions, of skyrmion number $n = 1$ and $n = 2$, respectively, obtained by rotating $\mathbf{S}(\mathbf{r})$ by an angle α about the S_2 axis of the Poincaré sphere. Rotating $\mathbf{S}(\mathbf{r})$ produces a smooth transformation from a Néel-type skyrmion ($\alpha = 0°$ in Figure 5.7) into a bimeron ($\alpha = 90°$ in Figure 5.7). Rotations of S^2 are of different nature, and will transform Néel-type skyrmions into Bloch-type skyrmions while preserving the skyrmion number. Note that these two types of rotations can equally be applied to anti-skyrmions, of negative skyrmion numbers, in which case one could effectively create "anti-bimeron" structures. Naturally, Figure 5.7 and 5.8 only provide eight topologically equivalent textures, but many more can be obtained by considering arbitrary rotations of $\mathbf{S}(\mathbf{r})$ and for each of these, additional ones can be created by rotating S^2. This menagerie of paraxial skyrmions is manifestly vast and it would seem that these patterns are completely interchangeable. Based on these considerations, one can produce a set of topologically equivalent skyrmionic structures experimentally by either using SU(2) polarization elements including quarter waveplates and half-waveplates [135] or by rotating the entire polarization profile [136].

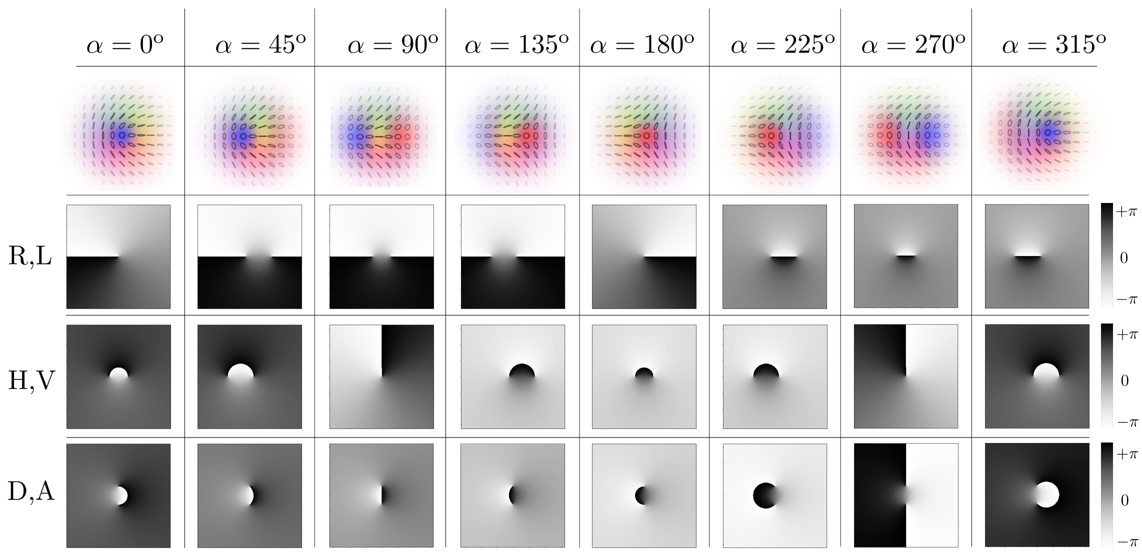

Figure 5.7: Intensity modulated polarization patterns and phase distributions for different bases for $n = 1$ skyrmion. Polarization patterns and phase distributions are shown with respect to right- and left-handed circularly polarized light (R,L), diagonal and anti-diagonal linearly polarized light (D,A) and horizontally and vertically polarized light (H,V) as phase singularities for rotation of $\mathbf{S}$ by an angle α about the S_2 axis, starting from an $n = 1$ Néel-type skyrmion when $\alpha = 0$. All skyrmion beams have a skyrmion number $n = 1$.

The dynamic evolution of the constellations of polarization singularities observed in the Stokes phase distribution Φ can be studied in figure 5.7 and 5.8 as α is varied to create topologically equivalent skyrmion textures. As expected, the choice of basis for Φ affects the trajectory of the individual polarization singularities, with static polarization singularities (here anti-diagonal and diagonal linearly polarized states) being obtained when $\mathbf{S}(\mathbf{r})$ is aligned with the rotation axis (here S_2) used to transform the polarization profile. This has implications for the calculation of the skyrmion number using $N = (2\pi)^{-1} \oint \partial\Phi \cdot \mathrm{d}\boldsymbol{\ell}$, as indicated in Eq. (4.27), as the polarization singularity can migrate to regions of

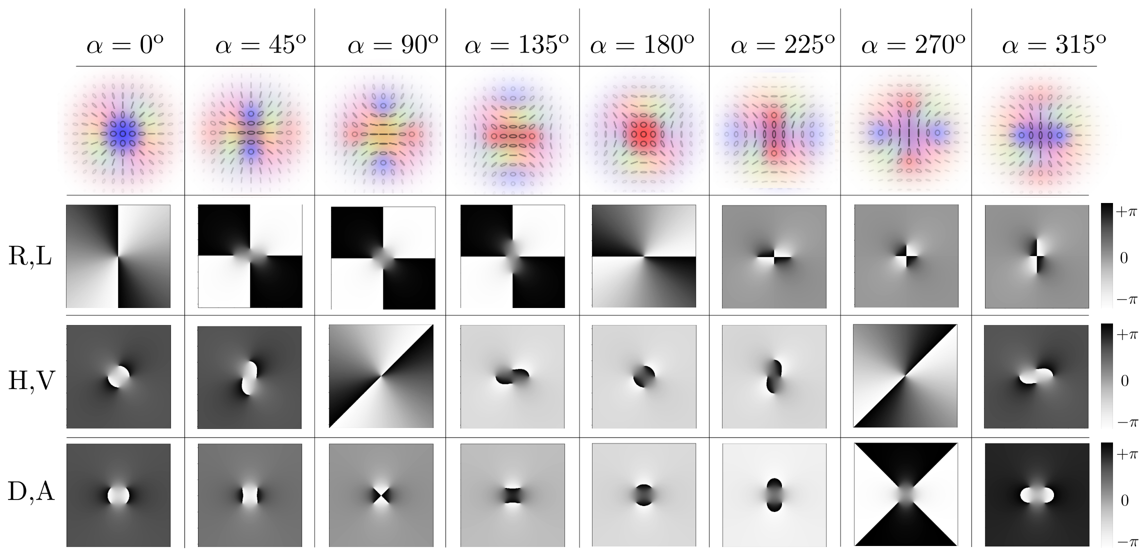

Figure 5.8: Intensity-modulated polarization patterns and phase distributions for different measurement bases for an $n = 2$ skyrmion. Polarization patterns and phase distributions are shown with respect to right- and left-handed circularly polarized light (R, L), diagonal and anti-diagonal linear polarizations (D, A), and horizontal and vertical linear polarizations (H, V). Each configuration corresponds to a rotation of the Stokes vector $\mathbf{S}$ by an angle α about the S_2 axis, starting from an $n = 2$ Néel-type skyrmion when $\alpha = 0$.

low intensity and deteriorate the measured skyrmion number depending on the choice of the vector potential. Indeed, in our example, it would appear that when $\alpha = 0°$, relying on an H,V basis or a D,A basis to measure the skyrmion number is equally advantageous compared to a measurement using the R,L basis where the singularity of left-handed circularly polarized light is located at the beam periphery. However, the two bases no longer provide the same advantage when the skyrmion beam propagates in a medium that realizes the SU(2) transformation corresponding to a rotation about the S_2 axis as the constellation of H and V singularities move to regions of lower intensity whereas D and A singularities remain in regions of low noise and high-intensity. This is therefore a new aspect to consider in the experimental characterization of skyrmion beams. We also note degeneracies in the Φ patterns across different bases (see for example R,L,$\alpha = 0°$ and H,V,$\alpha = 270°$ in figure. 5.7 and 5.8). This is expected as the same type of rotation is used to generate different vector potentials and to induce local rotations of the $\mathbf{S}$ vector.

5.7 Skyrmion Number Calculation for Mixed-up Bases Measurements

We have pointed out in section 5.3 and section 5.4 that while the skyrmion field remains the same under mixed-up bases measurements, the skyrmion potential does not. However, this changing of potential would still give us an unchanged skyrmion number, which is due to the gauge freedom in the vector potential. We have explored in previous sections how this is valid in terms of geometry, and proved it mathematically. There are at least two ways of proving this, and we have chosen the one that is more relevant to the organization and logic of this chapter.

Recall that Eq. (5.21) is a permuted form of Eq. (5.14). Taking our example of mixed-up bases measurements in Eq. (5.13) and substituting it into Eq. (5.21), we obtain the skyrmion field in the form of Eq. (5.15), which we have proven to be equivalent to the skyrmion field in consistent basis measurements.

Therefore, we have proven that despite changes in the form of the vector potential, the curl relation remains valid. We can thus conclude that vector potentials in different bases differ only by a gauge transformation and do not affect the calculation of skyrmion numbers. Moreover, based on this result, it is straightforward to show that the topological method remains valid for this generalization.

We will explain the calculation of skyrmion numbers by some specific examples. In the topological method we introduced in section 4.5, we have Eq. (4.26) which calculates the skyrmion number in terms of Stokes parameters and winding numbers, and Eq. (4.27) which defines the winding numbers. We now generalize Eq. (4.26) to mixed-up bases measurements, as [37]

$$n = \sum_j \frac{1}{4\pi} \oint_{\beta_j} S_z \partial\Phi \cdot d\boldsymbol{l} - \frac{1}{4\pi} \oint_{\alpha} S_z \partial\Phi \cdot d\boldsymbol{l}, \tag{5.34}$$

which means that S_z here can be any one of the Stokes parameters. Here, α and β_j represents our integration lines, as shown in Figure. 5.9. We point out here that the generalized Stokes parameter S_z, regardless of its specific form, is always a constant. As such, it can be factored out of the integration and summation, thereby separating the Stokes parameters from the winding numbers. This results in a topological formulation for calculating the skyrmion number, as we discussed in [120].

$$n = \frac{1}{2} \left(\sum_j S_z^{(j)} N_j - \bar{S}_z^{(\infty)} N_\infty \right). \tag{5.35}$$

This is because around the singularities, the integration contour is always infinitely small, causing the Stokes parameter to take the local value at the singular point. For points at infinity, the stereographic projection ensures that S_z takes the value of the Stokes parameter of the projection point. Now, we proceed to explain the calculation of the skyrmion number for skyrmions (in consistent basis measurements) and bimerons (one case of the mixed-up bases measurements). Note that, the topology has ensured that $N_\infty = \Sigma_j N_j$. In a skyrmion texture, where we recognize circular polarization points as the singularities, there is always only one singularity at the beam centre, and S_z always takes opposite values at beam centre and at the periphery. Therefore, we will always have

$$\begin{aligned} n &= \frac{1}{2}\left(\sum_j S_z N_j - (-S_z)\, N_\infty\right) \\ &= S_z \Sigma_j N_j. \end{aligned} \tag{5.36}$$

For the case of a bimeron, singularities always come in pairs, and these singularities are always opposite points on the Poincaré sphere. Because the integration contour is a loop, this guarantees that the contour around them always takes the same handedness, which on opposite points of thePoincaré sphere means opposite winding numbers. The Stokes parameters take opposite values on these pairs, while the beam periphery will always have zero contribution due to $N = 0$ guaranteed by $N_\infty = \Sigma_j N_j$.

Therefore the skyrmion number for a bimeron is

$$\begin{aligned} n &= \frac{1}{2}\left(\sum_j S_z N_j - 0\right) \\ &= \frac{1}{2}\Sigma_j S_z N_j. \end{aligned} \tag{5.37}$$

In our example of a n=2 bimeron, the horizontal and vertical polarizations are defined as singularities, with $S_z = S_1$. Specifically, we have $S_1 = 1$ for horizontal polarization and $S_1 = -1$ for vertical polarization. The corresponding winding numbers are $N = 1$ and $N = -1$, respectively. By substituting these values into Eq. (5.37), we can calculate the skyrmion number, which yields $n = 2$. The corresponding figures are shown in Figure. 5.9.

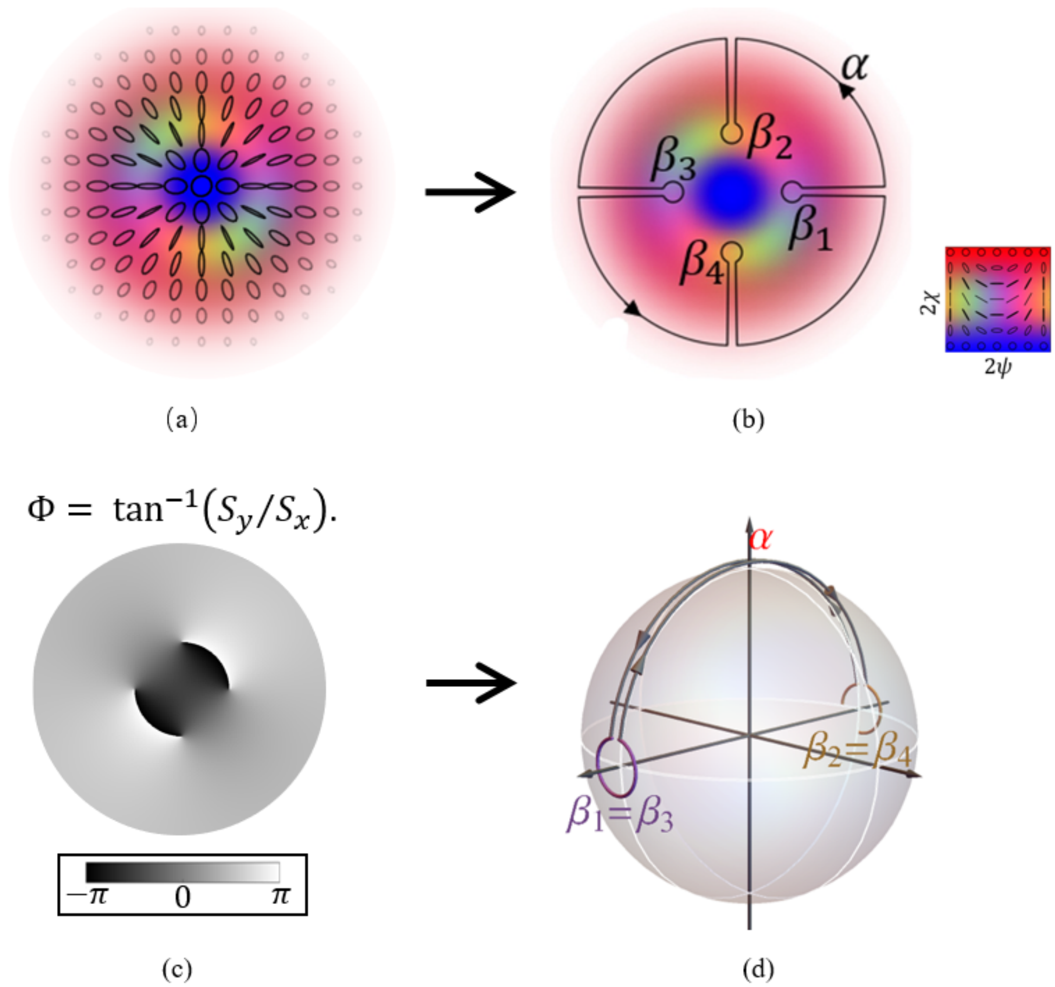

Figure 5.9: n=2 skyrmion (bimeron) under a mixed-up bases measurement. (a) is the original n=2 skyrmion field, (b) is the identification of the singularities and integration contour for the chosen mixed-up bases measurement ($S_z = S_1$). (c) is the corresponding Stokes phase, and (d) is the integration contour on the Poincaré sphere, where α is the integration line that goes counter-clockwise, and β_j are our integration lines which wind clockwise. The phase change on the contour around linear polarizations is directly related to the winding number. The colour scheme we used is defined in terms of orientation ψ, and ellipticity χ. (The figures is adapted from [120]).

5.8 Experimental Evaluations

An experiment has been designed and carried out by the Optics Group. The experimental setup used to generate skyrmion beams is shown in Figure 5.10 (reproduced from the supplementary material of [120]). The process begins with a diagonally polarized beam, which is separated into its horizontal and vertical polarization components using a Wollaston prism. These two beams are then imaged onto a digital micromirror device (DMD), where a binary multiplex hologram is applied to independently shape each component. The beams are subsequently recombined to produce a beam with spatially varying polarization. Stokes polarimetry is used to measure the Stokes parameters, which are then mapped onto the Poincaré sphere.

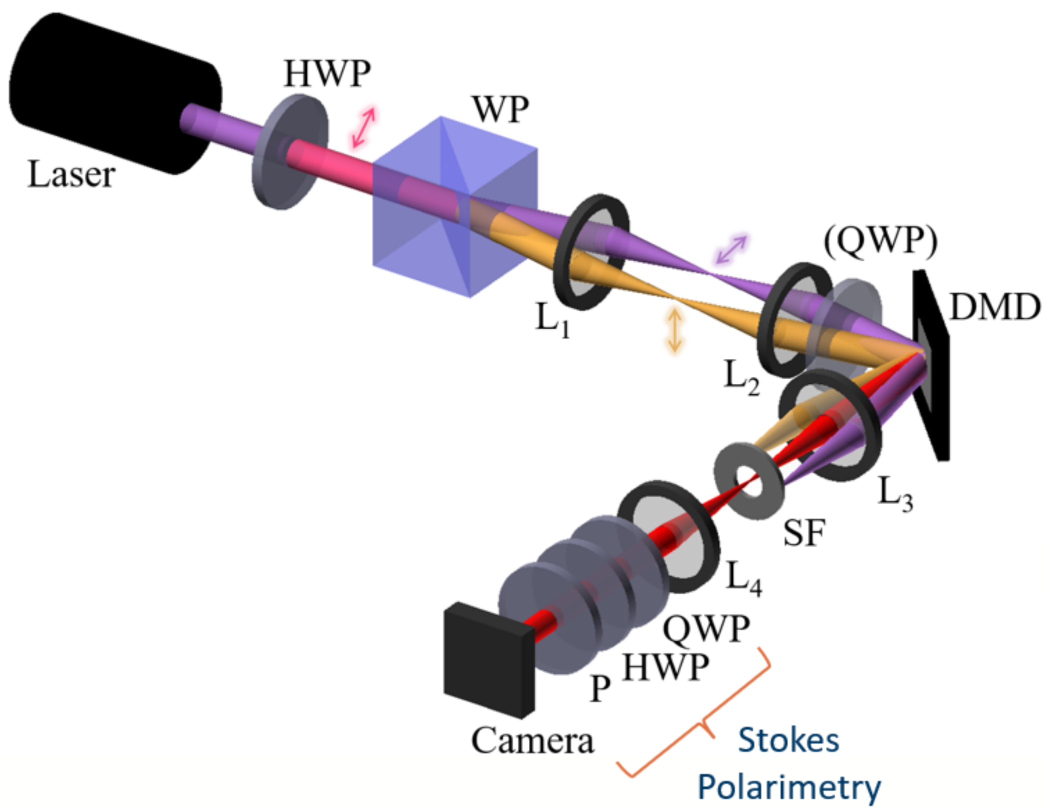

Figure 5.10: Experimental set up for generating skyrmions [120].

In Figure 5.11, experimentally generated skyrmions and bimerons are presented, produced using the setup described above. The bimerons can be interpreted as skyrmions that are prepared in the $|H\rangle$ and $|V\rangle$ basis but measured in the $|R\rangle$ and $|L\rangle$ basis. The use of mixed-up bases measurements offers the advantage of avoiding regions of low intensity. Moreover, such flexibility allows the Stokes parameters to be evaluated at a finite radius. This approach is particularly beneficial when measuring higher skyrmion numbers, as demonstrated in Figure 5.12.

In Figure 5.12, three different skyrmion number measurement methods are compared under increasing levels of background noise. The background noise is applied to simulated Néel-type skyrmion beams with $n = 1$ to 5, and the evaluation is carried out over a disk where the intensity exceeds 5% of the peak value. Solid lines represent values calculated using the standard flux definition: $n = \frac{1}{4\pi}\int_A \mathbf{S}\cdot\left(\frac{\partial \mathbf{S}}{\partial x}\times\frac{\partial \mathbf{S}}{\partial y}\right)\mathrm{d}x\mathrm{d}y$. Dotted lines are using Eq. (5.36) in the consistent basis measurement of the beam ($S_z = S_3$) and dashed lines show values when evaluating in a mixed-up bases measurement using Eq. (5.37) ($S_z = S_1$).

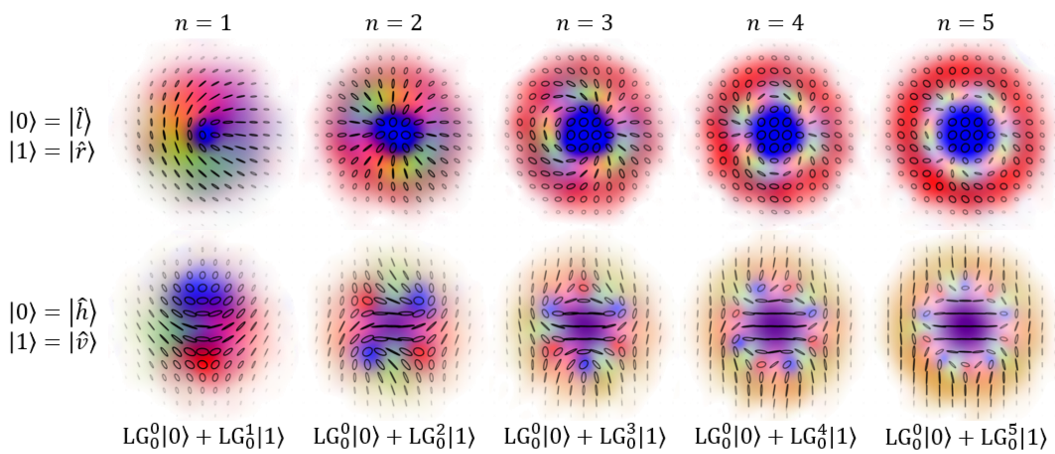

Figure 5.11: Experimentally generated $n = 1$ to 5 skyrmions in consistent basis measurement (top row) and mixed-up bases measurement (bottom row) [120].

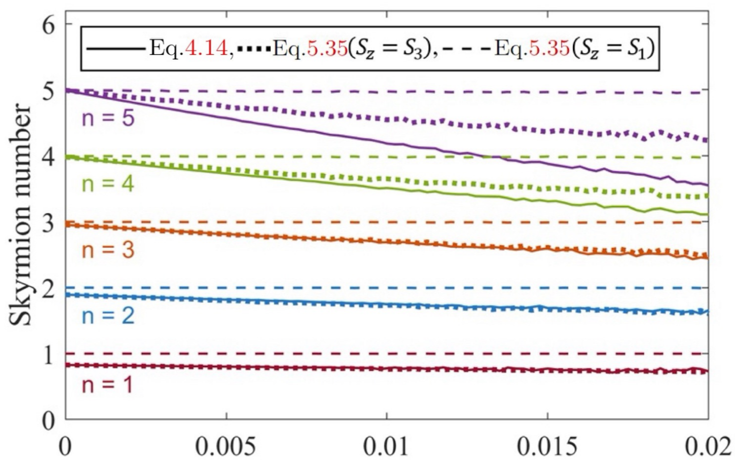

Figure 5.12: Comparison of the performance of skyrmion measurement methods for increasing noise levels. Increasing levels of background noise applied to simulated skyrmions with $n = 1$ to 5 equivalent to the beams shown in the top row of Figure. 5.11. The solid lines indicate values calculated using Eq. (4.14). Dotted lines correspond to values calculated using Eq. (5.35) in the consistent basis measurement ($S_z = S_3$) and dashed lines when evaluating Eq. (5.35) using an mixed-up bases measurement ($S_z = S_1$). (Figure adapted from [120] to fit the thesis).

5.9 Conclusions

In this chapter, we extended the theory of paraxial skyrmions by recognizing topologically equivalent skyrmion fields. An entire library of such equivalent fields can be obtained through rotations. We first proved that a skyrmion field remains unchanged under a consistent change of basis in its construction and measurement. We refer to this scenario as consistent basis measurements, in contrast to the mixed-up basis measurements we proposed. We also showed that, geometrically, a consistent basis measurement corresponds to a consistent rotation of both the Poincaré sphere and the plane of projection.

Next, we demonstrated that, even under a mixed-up basis measurement, the skyrmion field remains unchanged. However, the skyrmion potential undergoes a change, which can be understood as a gauge freedom that does not affect the curl relation. This result ensures that our topological method of calculating skyrmion numbers remains valid, even with a suitable generalization of parameters.

We then introduced a generalization of orthonormal states, which allowed us to construct generalized Pauli matrices and, consequently, generalize the Stokes parameters. Not surprisingly, the generalized Stokes parameters still preserve the unity of the Stokes vector. The concept of singularities is also generalized, extending beyond circular polarizations. We then built an atlas of skyrmion textures based on this generalization.

The practical application of this generalization is in the calculation of skyrmion numbers. We derived theoretical expressions for skyrmion numbers in two special cases: skyrmions and bimerons, and presented experimental results for these measurements. It is clear that this generalization allows us to calculate skyrmion numbers for different equivalences of skyrmion textures, where singularities are identified differently, effectively avoiding low-intensity areas.

Perspectively, topologically equivalent skyrmion beams could prove useful in general bipartite free-space quantum key distribution, where information is encoded in the polarization degree of freedom. Such beams could remove the need to establish a shared reference frame, enhancing the efficiency and security of quantum communication.

Chapter 6

A New Method to Describe 3D Polarized Fields

6.1 Introduction

Previously, we have worked on paraxial skyrmions, or baby skyrmions, where a topologically protected polarization structure was investigated and linked perfectly with the Poincaré sphere. We would, however, want to see how a skyrmion field behaves outside the paraxial regime. For example, how a skyrmion field would behave under strong focusing.

We propose a two-sphere method to characterize 3D polarization, based on the existing Majorana (Poincarana) sphere method [137, 138]. A strongly focused skyrmion beam, which enters the regime of 3D polarization, is one example where this new method can be applied.

The structure of this chapter is as follows: In section 6.2, we briefly review the history of the Majorana sphere and how it became a useful tool for the description of light beam. In section 6.3, we introduce the mathematical construction of the Poincarana sphere, an optimized re-normalization of the Majorana sphere. In section 6.4, we present our two-sphere method as a novel tool for analyzing 3D polarization. And finally in section 6.5, we provide an example of a focused paraxial skyrmion to demonstrate how this new method can be applied.

6.2 Hannay-Majorana Sphere

In his original work, Majorana defined a polynomial, now named after him, the roots of which lie in the complex plane and can be stereographically projected onto a S^2 sphere, in the following paragraph, we will briefly illustrate how his idea works.

The idea of Majorana representation is an elegant treatment of higher-order spinors [139, 140]. To briefly summarize the story, we start with the Jones calculus, where Jones represents the electric field vectors as complex 2-vectors. This construction allows the Stokes parameters, which is an ingenious invention that fully characterizes the transverse rapid oscillations of a light beam, nowadays known as its polarization properties, to be represented by the Pauli matrices. A more precise term for Jones vectors might be Jones spinors instead. Majorana's representation builds on this idea of spinor representation and generalizes it to higher dimensions. A spin-l object, for example, corresponds to a spinor of dimension $N = 2l + 1$.

A special class of spinors can be defined that transform under a subgroup of SU(N). and whose components are related to binomial coefficients. More precisely, the structure of these spinors resembles binomial distributions in the sense that each component is weighted by the square root of a binomial coefficient [139]. These specially structured spinors can be used to define a polynomial of degree $n-1$, constructed by taking an inner product between a conjugated spinor ξ^* and a monomial spinor basis involving powers of the complex variable z. For example, in the case of a 3-spinor, this polynomial takes the form:

$$p(z;\xi) = \xi_0^* z^3 + \sqrt{3}\xi_1^* z^2 + \sqrt{3}\xi_2^* z + \xi_3^*. \tag{6.1}$$

The $n-1$ roots of this polynomial correspond to points in the complex plane, which can be mapped onto a sphere via an inverse stereographic projection. This defines the so-called Majorana sphere representation of the spinor.

Degenerate cases may arise where the leading coefficients vanish (e.g. $\xi_0 = 0$), effectively reducing the degree of the polynomial. While this might seem to reduce the number of solutions, such "missing" roots are interpreted as points at infinity. Following Riemann's prescription, these correspond to the North Pole of the sphere under stereographic projection [141]. Hence, the full set of $n-1$ roots, including repeated and degenerate ones, are mapped to points on the Majorana sphere, with indistinguishable roots occupying the same location, and "infinite" roots mapping to the pole. An example of the Majorana representation is given in Figure. 6.1.

The idea of Majorana sphere was first applied to light by Hannay in 1998 [137]. In his paper, Hannay applied the idea of representing a spin-N system uniquely by $2N$ dots on a unit sphere in real space. He then stressed that light, being a spin-1 object, should correspond to two points on the Majorana sphere. But light has the massless property, which imposes certain restrictions to the points on the sphere. Specifically, the two points representing light on the sphere should determine its propagation direction. Hannay then proposed a projection method

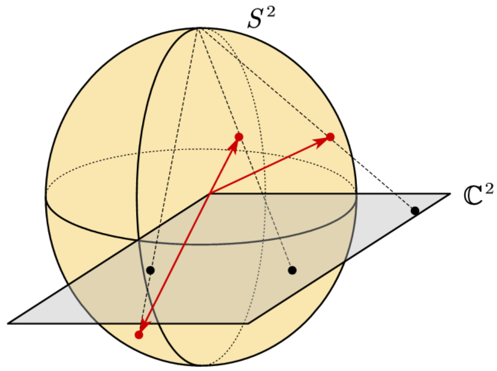

Figure 6.1: An example of the Majorana representation of a 4-spinor, where black dots represent points on the complex plane and red dots represent points on the sphere.

that utilized this property, where he placed a polarization ellipse in the plane of the large circle of the sphere and projecting its foci onto the sphere (Figure. 6.2).

6.3 Constructing the Poincarana Sphere

In this section, we will follow works by Bliokh et al. [138] and Alonso [38] to introduce how the Hannay-Majorana sphere can be applied to structured light and how it is optimized to Poincarana sphere. Consider a monochromatic and fully polarized, non-paraxial 3D electric field with a complex vector form. We are familiar with the 2D form of the $\mathbf{E}$ field, which is expressed in terms of trigonometric functions, and in its propagation direction traces out ellipses that represent the (2D) polarization ellipses. Here, we will write the 3D field in a similar manner, as

$$\mathbf{E} = A \exp{(\mathrm{i}\Phi)}(\mathbf{a} + \mathrm{i}\mathbf{b}), \tag{6.2}$$

where $A = |\mathbf{E}|$, Φ is a global phase, and $\mathbf{a}$ and $\mathbf{b}$ are mutually orthogonal vectors that add up to the unit vector, which traces out the direction of our $\mathbf{E}$ field. Without loss of generality, we can define $|\mathbf{a}| \geq |\mathbf{b}|$. It is not difficult to see that Eq. (6.2) is a 3D ellipse, with $\mathbf{a}$ and $\mathbf{b}$ corresponding to its major and minor axes, respectively. We can also express the phase in terms of our electric field, as

$$\Phi = \frac{1}{2}\mathrm{Arg}(\mathbf{E} \cdot \mathbf{E}). \tag{6.3}$$

Note that there are degenerate cases for this definition, namely when the ellipse becomes circular or linear. In the case of circular polarization, the phase

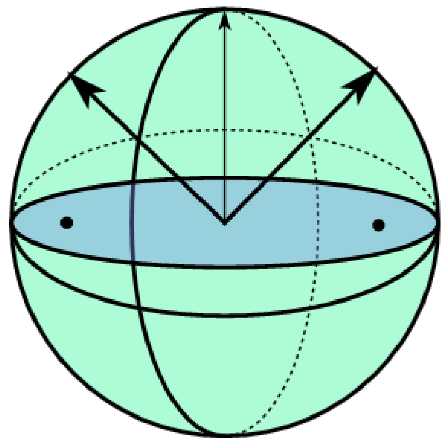

Figure 6.2: A reproduction of Hannay's original figure. The blue ellipse is the polarization ellipse lying in the Majorana unit sphere, its two foci are projection of the two unit vectors which represent the polarization state. Their bisector (or its reverse) is the propagation direction [137].

in Eq. (6.3) would become undefined, which is usually known as the C-points [142].

The next important quantity to define is the spin density $\mathbf{S}$, which is defined as $\mathbf{S} = \mathrm{Im}\left(\mathbf{E}^{*} \times \mathbf{E}\right)$ for a fully polarized beam. Eq. (6.2) expresses $\mathbf{S}$ in terms of $\mathbf{a}$ and $\mathbf{b}$, with some calculations, we can find a relation between the spin density $\mathbf{S}$, and $\mathbf{a}$, $\mathbf{b}$, as $\mathbf{S} = 2A^2\mathbf{a} \times \mathbf{b}$, which tells us that geometrically, this quantity is perpendicular to the plane of the polarization ellipse, as shown in Figure. 6.3.

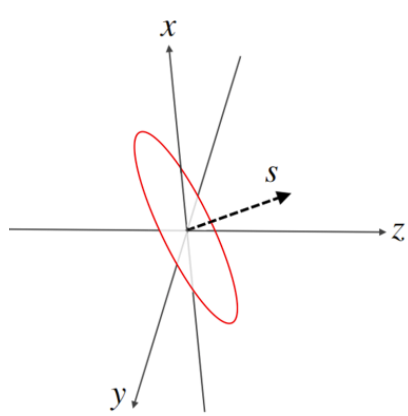

Figure 6.3: Polarization ellipse and spin direction.

For later convenience, we will instead use the normalized spin density, which is defined as

$$\mathbf{s} = \frac{\operatorname{Im}(\mathbf{E}^* \times \mathbf{E})}{|\mathbf{E}|^2} = 2\mathbf{a} \times \mathbf{b}. \tag{6.4}$$

where $\mathbf{s}$ is the normalized spin density, which takes the maximum value of unity, when the polarization is circular, and vanishes when the polarization is linear [38].

One may realize the connection between the spin density and the Stokes vector. In 2D cases, the Stokes parameters are directly linked to the 2D polarization ellipse, and the direction normal to the 2D ellipse being the z direction. However, it is important to notice that the normalized Stokes vector resides in an abstract parameter space (the Poincaré sphere), while the spin density vector lives in real space. Therefore, the components of the Stokes vector do not correspond to the spin density in 2D, due to their incorrect commutation relations and normalizations, as pointed out by Berry [143]. In fact, the z-component of the Stokes vector corresponds to the spin density of the 2D polarization.

We now turn to Hannay's construction. As stated before, light corresponds to two points on the Majorana sphere, with the restriction that their bisector is the propagation direction. Here, we represent these two points on the unit sphere by two positional vectors, $\mathbf{u}_{1,2}$. These unit vectors has four degrees of freedom, thus fully characterizing the 3D ellipse. The tips of the two unit vectors project to the foci of the polarization ellipse by construction.

To better incorporate the normalization of the polarization ellipse, Bliokh et al. [138] proposed the Poincarana sphere, which, in principle, is a re-normalization of the Hannay-Majorana construction. The relation between $\mathbf{u}_{1,2}$ and the spin direction is as follows:

$$\mathbf{u}_{1,2} = \pm\sqrt{1-\beta^2}\bar{\mathbf{a}} + \beta\bar{\mathbf{s}}, \tag{6.5}$$

where the bar above indicates unit vectors, β is the eccentricity of the polarization ellipse. Hannay-Majorana construction defines $\beta = \arctan|\bar{\mathbf{b}}|/|\bar{\mathbf{a}}|$. Geometrically, it corresponds to the angle between z-axis and $\mathbf{p}_{1,2}$, where $\mathbf{p}_{1,2}$ are points of Hannay-Majorana representation, as shown in Figure. 6.4. For a unit sphere, $\bar{\mathbf{a}}, \bar{\mathbf{b}}$ are along the major and minor axes of the polarization ellipse, while $\bar{\mathbf{s}}$ is along the spin direction.

Furthermore, $\beta = |\mathbf{S}| = 2|\mathbf{A}||\mathbf{B}|$, where $\mathbf{A}$ and $\mathbf{B}$ are real vectors representing semi-major and semi-minor axes of the normalized polarization ellipse. This is directly related to the geometrical phase through the solid angle enclosed on the sphere, as demonstrated in [138]. In the 2D case, we see this definition gives

$$u_{1,2z} = \mathcal{S}_3 = S_z, \tag{6.6}$$

where $u_{1,2z}$ refers to the z-component of $\mathbf{u}_{1,2}$, and $\mathcal{S}_3$ is the third Stokes parameter, corresponding to the z component of the Stokes vector. This normalization

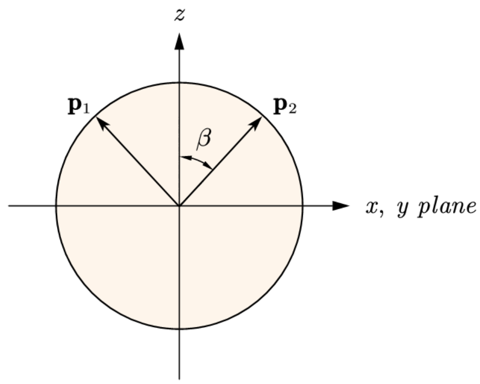

Figure 6.4: Geometrical meaning of β. $\mathbf{p}_1$, $\mathbf{p}_2$ are vectors for the Hannay-Majorana representation.

guarantees the height (or z-component) of the representation points on the two spheres are the same. This is where the name "Poincarana" comes from. It is not difficult to see that representation points of the Poincarana and the Majorana sphere will merge for circular and linear polarizations. A summary of the properties of these representations will be given in Figure. 6.6 in the next section.

6.4 Two-Sphere Method

When considering paraxial beams, four parameters are used for the complex x and y values. These are well described by the Stokes parameters, which are components of the Stokes vector that resides on the Poincaré sphere. The Poincarana sphere, on the other hand, is a sphere in real space and is capable of describing a 3D polarization. One may take a reasonable guess and seek the possibility of using the Poincarana sphere as the proper sphere for describing a 3D field vector. This, however, would not be sufficient.

If we consider representing a single 3D polarization ellipse with two points on the Poincarana sphere, the information of it would be clear, as the two points on the Poincarana sphere give information about ellipticity and orientation through their separation and bisector, respectively. However, for a structured light beam, each point on the beam's cross-section has its own polarization ellipse, all oriented in different directions. Recording such information on a single Poincarana sphere would be messy, as the information of ellipticities and orientations are all mixed up.

The intrinsic reason for this is that an S^2 sphere has only 2 dimensions, which allows it to record the information of only two complex vectors. To overcome this limitation, we hereby introduce a second sphere, which we call a spin direction sphere. With this additional sphere we have enough dimensions to record a distribution of polarizations for non-paraxial structured light beams.

This approach is inspired by the fact that a 3D polarization can degenerate in two ways: if we fix the orientation of the spin, 3D polarizations become the familiar 2D polarizations, which can be described by the Poincaré sphere. Conversely, if we consider a field composed of polarization ellipses that all have same ellipticity but differ in orientation, we can use one sphere to record all the spin directions and one number (or the seperation of foci on the sphere for any of the ellipses) for the ellipticity. Thus, the information of a general 3D polarization distribution can be represented by two S^2 spheres. We already presented the Poincaré sphere, here, we present the schematic plot of the spin-direction sphere in Figure. 6.5.

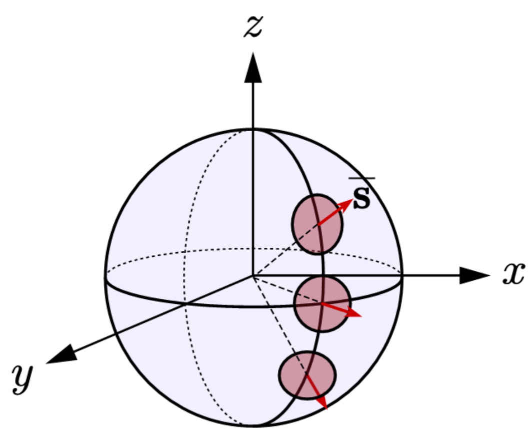

Figure 6.5: A schematic diagram of the spin-direction sphere, where each point of the sphere is associated with a circular polarization and its spin direction is represented by an red arrow locally perpendicular to the surface of the sphere.

We now possess a comprehensive understanding of the construction of the Poincaré sphere, the Poincarana sphere, and the spin direction sphere. Their relationships are summarized in Figure. 6.6, where we have represented their connections with the relevant quantities.

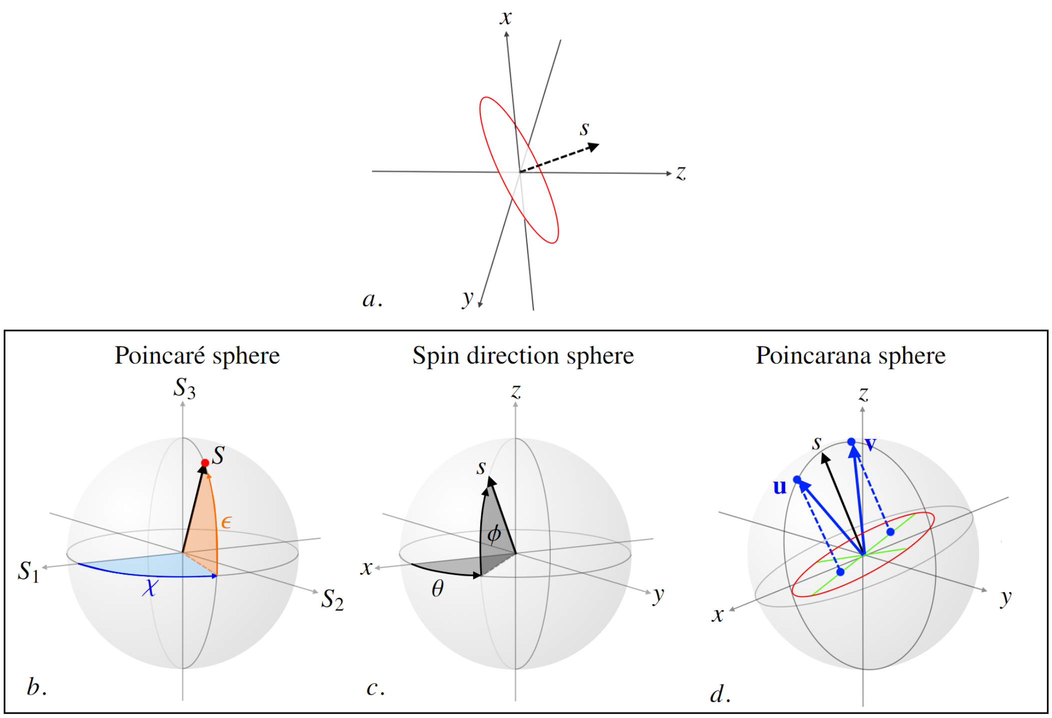

Figure 6.6: A plot of the 3D polarization ellipse and the spin vector **s** (a), the Poincaré sphere (b), the spin direction sphere (c), and the Poincarana sphere (d). The Poincaré sphere has the components of the Stokes vector as its axes. The spin direction sphere is a sphere represents the space where the spin vector **s** resides. Finaaly, the Poincarana sphere is a sphere in real space, where a 3D Polarization ellipse lies in a plane passing through its centre.

6.4.1 General Algorithm of the Two Sphere Method

Based on the mathematical construction from the previous section, we now introduce our algorithm for separating the information of spin direction and ellipticity. First, we establish a standard reference direction; let us choose z-axis without loss of generality. For an $\mathbf{E}$ field in the form of Eq. (6.2), we can determine the global phase using Eq. (6.3), which we write again here as

$$\Phi = \frac{1}{2}\mathrm{Arg}(\mathbf{E}\cdot\mathbf{E}). \tag{6.7}$$

Next, we calculate the field amplitude $|\mathbf{E}|$. Using the phase and amplitude, we obtain the normalized field vector, expressed as $\mathbf{e} = \mathbf{E}/|\mathbf{E}| = \mathbf{a} + \mathrm{i}\mathbf{b}$. We then apply Eq. (6.4) to determine the normalized spin density vector $\mathbf{s}$.

The spin density vector gives us the information of spin direction for each field point, with which we can plot our spin-direction sphere.

Now we turn to the Poincarana sphere for representing polarization information. To isolate polarization information, we locally erase the spin direction for each field point by rotating $\mathbf{s}$ to $\pm\mathbf{z}$. The choice of plus or minus $\mathbf{z}$ is determined by the handedness of the polarization ellipse, i.e., the hemisphere on which $\mathbf{s}$ resides. Spin vectors corresponding to right-handed polarization ellipses lie on the northern hemisphere and are therefore rotated to $+\mathbf{z}$, while those for left-handed polarization ellipses lie on the southern hemisphere and are rotated to $-\mathbf{z}$.

We now take the plus case as an example to demonstrate how this rotation works, noting that the minus case follows a similar process.

To rotate the spin vector of right-handed polarizations, we first define a third unit vector, $\mathbf{n}$, which is perpendicular to both $\mathbf{s}$ and $\mathbf{z}$. Next, we determine the angle θ between $\mathbf{s}$ and $\mathbf{z}$. Using this information, we can construct a 3D rotational matrix, that allows us to rotate $\mathbf{s}$ to align with $\mathbf{z}$ by applying a rotation of angle θ about the axis defined by $\mathbf{n}$. The detailed calculations are presented in the following.

The expression of $\mathbf{s}$ can be easily determined once the electric field is expressed, as shown in Eq. (6.4). Thus, we express every related quantity in terms of the components of $\mathbf{s}$. First, we calculate $\mathbf{n}$, which is the rotational axis, as

$$\mathbf{n}_+ = \mathbf{s}\times\mathbf{z} = (s_y, -s_x, 0)^T\,. \tag{6.8}$$

The general 3D rotational matrix has the form

$$R = \begin{bmatrix} \cos\theta + n_x^2(1-\cos\theta) & n_x n_y(1-\cos\theta) - n_z\sin\theta & n_x n_z(1-\cos\theta) + n_y\sin\theta \\ n_y n_x(1-\cos\theta) + n_z\sin\theta & \cos\theta + n_y^2(1-\cos\theta) & n_y n_z(1-\cos\theta) - n_x\sin\theta \\ n_z n_x(1-\cos\theta) - n_y\sin\theta & n_z n_y(1-\cos\theta) + n_x\sin\theta & \cos\theta + n_z^2(1-\cos\theta) \end{bmatrix}. \tag{6.9}$$

From it we construct our 3D rotational matrix with respect to $\mathbf{n}_+$ which we rotate around

$$R_+ = \begin{bmatrix} \cos\theta + s_y^2(1-\cos\theta) & -s_y s_x(1-\cos\theta) & -s_x \sin\theta \\ -s_x s_y(1-\cos\theta) & \cos\theta + s_x^2(1-\cos\theta) & -s_y \sin\theta \\ s_x \sin\theta & s_y \sin\theta & \cos\theta \end{bmatrix}. \quad (6.10)$$

Similarly, the rotational axis for the minus case would be

$$\mathbf{n}_- = \mathbf{s} \times (-\mathbf{z}) = (-s_y, s_x, 0)^T, \quad (6.11)$$

and the relevant rotational matrix

$$R_- = \begin{bmatrix} \cos\theta + s_y^2(1-\cos\theta) & -s_y s_x(1-\cos\theta) & s_x \sin\theta \\ -s_x s_y(1-\cos\theta) & \cos\theta + s_x^2(1-\cos\theta) & s_y \sin\theta \\ -s_x \sin\theta & -s_y \sin\theta & \cos\theta \end{bmatrix}. \quad (6.12)$$

Eq. (6.10) and Eq. (6.12) define the rotational matrices constructed to rotate $\mathbf{s}$ to $\pm\mathbf{z}$. Since the representation points of $\mathbf{u}_{1,2}$ and $\mathbf{s}$ must undergo rigid rotation, we apply the same 3D rotational matrix to $\mathbf{u}_{1,2}$. By performing the appropriate rotational operation at each field point, we obtain a distribution of points corresponding to a series of re-oriented ellipses.

An equivalent statement of this is that we "flatten" the polarization surface onto a plane. In doing so, we are able to represent the polarization information by a second sphere, analogous to how we represent 2D polarization on the Poincaré sphere.

One important point to note is that when describing the polarization distribution information, we are not necessarily limited to the Poincaré sphere. The Poincarana sphere may even offer some advantages over the Poincaré sphere, as we will discuss in the next subsection.

6.4.2 A Comparison of the Poincaré Sphere and the Poincarana Sphere

As discussed in previous chapters, the mathematical relations between 2D polarizations and the Poincaré sphere have already been established, so we will not repeat them here. While the Poincarana sphere is not sufficient for representing a 3D polarization distribution, it can still serve as a powerful tool for describing 2D polarization distributions. In this subsection, I will use the familiar paraxial skyrmion as an example to explain the similarities it shares with the Poincaré sphere, as well as the unique features it provides that are lacking in Poincaré sphere representations.

The mapping between 2D polarization ellipses and the Poincarana sphere is straightforward, with their foci mapped onto the sphere along z-direction (Figure. 6.6 (d)). We observe that the separation between the foci increases as the ellipticity decreases, eventually leading to linear polarizations, where the two foci coincide with the two endpoints, located on the equator of the sphere. Conversely, as the ellipticity increases, we reach a circle with a single focus at the center, corresponding to a point at the North Pole.

The normalization of the Poincarana sphere guarantees Eq. (6.6), meaning that for a 2D polarization, its representation points on both the Poincaré sphere and the Poincarana sphere have the same latitude (or height), as illustrated by the examples of linear and circular polarizations discussed earlier.

Now, if we consider an $n = 1$ skyrmion pattern, one might naively assume that an $n = 1$ skyrmion will cover the Poincarana sphere twice, since each polarization is represented by 2 points, and thus the total number of points would be twice that of the Poincaré sphere. However, this is not the case. f we examine a latitudinal circle on the Poincaré sphere, we see that half of the circle corresponds to a phase change of $\pi/2$, as the antipodal points represent orthogonal polarization states. On the Poincarana sphere, however, a $\pi/2$ phase change corresponds to only one-quarter of a latitudinal circle. This difference comes from the fact that the orientation angles of polarization ellipses are doubled in Poincaré sphere. Therefore, a $n = 1$ skyrmion should also cover the Poincarana sphere only once.

A simulation illustrating how an $n = 1$ skyrmion covers the Poincaré sphere is shown in Figure 6.7. The south pole is not covered because the points in the simulation cannot reach infinity. This figure tells us that in the paraxial case, the Poincarana representation contains the same information as the Poincaré sphere.

One advantage of the Poincarana sphere over the Poincaré Sphere is its ability to generalize the definition of 2D skyrmions. As described by Nagaosa and Tokura in [35], there are different types of magnetic skyrmions, which are distinguished based on their magnetization vector (or, in our optical context, the Stokes vector) in spherical coordinates.The polar angle of this vector determines the helicity. In our construction, this is equivalent to stating that the phase difference between the LG_0^n and LG_0^0 terms can be written as $\Phi(\rho, z) = \ell_d\phi + \theta(\rho, z)$, where ℓ_d corresponds to the winding number, or skyrmion number, and $\theta(\rho, z)$ determines the skyrmion type.

For magnetic skyrmions, a phase change of $\pi/2$ would switch a Bloch skyrmion to a Néel skyrmion. However, in the case of a paraxial 2D skyrmion field, such a phase change results only in rotations within the skyrmion pattern. This can be easily verified through simulation, and it has been discussed in the literature, such as in [127].Therefore, for 2D optical skyrmions, we do not distinguish between Néel and Bloch types.

That said, creating an optical Bloch skyrmion is still possible. An example has

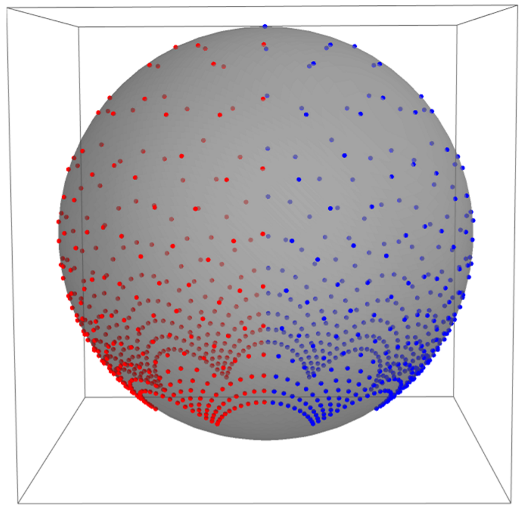

Figure 6.7: Poincarana sphere for n=1 paraxial skyrmion, where red and blue points represent $\mathbf{u}_1$ and $\mathbf{u}_2$ for all points in the polarization distribution.

been given in [106], where a Bloch C-skyrmion was created by strong focusing of an $n = 2$ skyrmion using an aplanatic system, which we had explained in subsection 2.6.2. We will discuss this construction further in the following section and use it as an application of the two-sphere method. For now, we focus on the Bloch C-skyrmion created in this process.

The Bloch C-skyrmion can actually be linked to the other degenerate case of general 3D polarization, as it matches the description of a field composed of polarization ellipses that orient differently but share the same ellipticity. This construction lies beyond the paraxial regime and cannot be described by the Poincaré sphere. However, the Poincarana sphere still allows us to represent and define the skyrmion number as the coverage of the Poincarana sphere.

6.5 Focused n=2 Paraxial skyrmion Field

Now, we turn to the focusing of a paraxial skyrmion as an example of the application of the two-sphere method. First, we construct an $n = 2$ skyrmion by superposing LG beams:

$$|\psi\rangle = \frac{1}{\sqrt{2}} \left(\mathrm{LG}_0^0 \, |0\rangle + \mathrm{LG}_0^2 \, |1\rangle \right), \tag{6.13}$$

where we take $|0\rangle = |L\rangle$ and $|1\rangle = |R\rangle$. Here, we follow the Richards & Wolf model [41, 39] to derive the field after strong focusing.

We first calculate the far-field which enters the focusing system, for y- and x-polarization, respectively

$$\begin{aligned}
\mathbf{E}^{y}_{\infty}(\theta,\phi) = &\left[\mathbf{E}_{\text{inc}}(\theta,\phi)\cdot\begin{pmatrix}-\sin\phi\\ \cos\phi\\ 0\end{pmatrix}\right]\begin{pmatrix}-\sin\phi\\ \cos\phi\\ 0\end{pmatrix}\sqrt{\frac{n_1}{n_2}}(\cos\theta)^{1/2}+\\
&\left[\mathbf{E}_{\text{inc}}(\theta,\phi)\cdot\begin{pmatrix}\cos\phi\\ \sin\phi\\ 0\end{pmatrix}\right]\begin{pmatrix}\cos\phi\cos\theta\\ \sin\phi\cos\theta\\ -\sin\theta\end{pmatrix}\sqrt{\frac{n_1}{n_2}}(\cos\theta)^{1/2}\\
=&\left[E_{\text{inc}}(\theta,\phi)\cdot\mathbf{n_y}\cdot\begin{pmatrix}-\sin\phi\\ \cos\phi\\ 0\end{pmatrix}\right]\begin{pmatrix}-\sin\phi\\ \cos\phi\\ 0\end{pmatrix}\sqrt{\frac{n_1}{n_2}}(\cos\theta)^{1/2}+\\
&\left[E_{\text{inc}}(\theta,\phi)\cdot\mathbf{n_y}\cdot\begin{pmatrix}\cos\phi\\ \sin\phi\\ 0\end{pmatrix}\right]\begin{pmatrix}\cos\phi\cos\theta\\ \sin\phi\cos\theta\\ -\sin\theta\end{pmatrix}\sqrt{\frac{n_1}{n_2}}(\cos\theta)^{1/2}\\
=&E_{\text{inc}}(\theta,\phi)\left[\begin{pmatrix}-\sin\phi\cos\phi\\ \cos^2\phi\\ 0\end{pmatrix}+\begin{pmatrix}\sin\phi\cos\phi\cos\theta\\ \sin^2\phi\cos\theta\\ -\sin\phi\sin\theta\end{pmatrix}\right]\sqrt{\frac{n_1}{n_2}}(\cos\theta)^{1/2}\\
=&E_{\text{inc}}(\theta,\phi)\frac{1}{2}\begin{pmatrix}(\cos\theta-1)\sin 2\phi\\ (1+\cos\theta)+(1-\cos\theta)\cos(2\phi)\\ -2\sin\phi\sin\theta\end{pmatrix}\sqrt{\frac{n_1}{n_2}}(\cos\theta)^{1/2},
\end{aligned}\tag{6.14}$$

similarly we have

$$\mathbf{E}^{x}_{\infty}(\theta,\phi) = E_{\text{inc}}(\theta,\phi)\frac{1}{2}\begin{bmatrix}(1+\cos\theta)-(1-\cos\theta)\cos(2\phi)\\ -(1-\cos\theta)\sin(2\phi)\\ -2\cos\phi\sin\theta\end{bmatrix}\sqrt{\frac{n_1}{n_2}}(\cos\theta)^{1/2}.\tag{6.15}$$

The reason we use x- and y-polarization here is the same as in chapter 3, we want to make use of the previous result we get for the Hermite-Gaussian beams, so as to save some calculation work. One can of course start directly with l- and r-polarization. Now, we decompose the LG beams into HG beams, using their generating function from the Gaussian beam, we have

$$\text{LG}_0^2 = \text{HG}_{20} + 2i\text{HG}_{11} - \text{HG}_{02}.\tag{6.16}$$

We then derive the incident beam expression for higher order HG beams from the lowest-order mode, using Eq. (2.20) we find

$$\begin{aligned} E_{\mathrm{inc}}(\theta,\phi) &= 2E_0\left(\frac{2y^2-w_0^2}{w_0^2}\right)e^{-\left(x^2+y^2\right)/w_0^2} \\ &= 2E_0\left(\frac{2f^2\sin^2\theta\sin^2\phi-w_0^2}{w_0^2}\right)e^{-f^2\sin^2\theta/w_0^2}\quad(\mathrm{HG}_{02})\,, \end{aligned} \tag{6.17}$$

$$\begin{aligned} E_{\mathrm{inc}}(\theta,\phi) &= 4E_0\frac{xy}{w_0^2}e^{-\left(x^2+y^2\right)/w_0^2} \\ &= 4E_0\frac{f^2\sin^2\theta\sin\phi\cos\phi}{w_0^2}e^{-f^2\sin^2\theta/w_0^2}\quad(\mathrm{HG}_{11})\,, \end{aligned} \tag{6.18}$$

$$\begin{aligned} E_{\mathrm{inc}}(\theta,\phi) &= 2E_0\left(\frac{2x^2-w_0^2}{w_0^2}\right)e^{-\left(x^2+y^2\right)/w_0^2} \\ &= 2E_0\left(\frac{2f^2\sin^2\theta\cos^2\phi-w_0^2}{w_0^2}\right)e^{-f^2\sin^2\theta/w_0^2}\quad(\mathrm{HG}_{20})\,, \end{aligned} \tag{6.19}$$

where the relevant mode is indicated in the bracket, and we have used the relation of the far field as $x = f\sin\theta\cos\phi$ and $y = f\sin\theta\sin\phi$, as given in Eq. (2.50). We then combine the decomposed HG modes to obtain the desired LG_0^2 mode, and substitute the incident beam into Eq. (6.14) to calculate the focused beam, as we show in the following.

We follow chapter 3 for all definitions of parameters. We define $x = f\sin\theta\cos\phi$ and $y = f\sin\theta\sin\phi$, where (x, y, z) represents a point on the reference sphere of the aplanatic system, f is the focal length, and (θ, ϕ) are spherical angles (see subsection 2.6.2, Figure. 2.7). We then define $f_w(\theta) = e^{-\left(x^2+y^2\right)/w_0^2}$ as an apodization function, previously mentioned in 3.4.1. From Eq. (6.16) to Eq. (6.19) we can calculate

$$\begin{aligned} \mathrm{LG}_0^2 &= \mathrm{HG}_{20} + 2i\mathrm{HG}_{11} - \mathrm{HG}_{02} \\ &= \frac{2E_0}{w_0^2}\left[\left(2x^2-w_0^2\right)+4ixy-\left(2y^2-w_0^2\right)\right]f_w(\theta) \\ &= \frac{4E_0}{w_0^2}f_w(\theta)\left[x^2-y^2+2ixy\right] \\ &= \frac{4E_0}{w_0^2}f_w(\theta)\left[\cos 2\phi + i\sin 2\phi\right] \\ &= \frac{4E_0}{w_0^2}f_w(\theta)e^{i2\phi}. \end{aligned} \tag{6.20}$$

From this we modify the trigonometrical integration relations to get

$$\int_0^{2\pi} e^{in\phi}\mathrm{e}^{\mathrm{i}x\cos(\phi-\varphi)}\mathrm{d}\phi = 2\pi\left(\mathrm{i}^n\right)J_n(x)e^{in\varphi}. \tag{6.21}$$

We now calculate the coefficient matrix for LG_0^2. To do this, we send the incident paraxial beam, given by Eq. (6.20), through the aplanatic system. This is to say we plug Eq. (6.20) as E_{inc} into Eq. (6.15) and Eq. (6.14) to get the far field for x- and y-polarized beam, respectively. As

$$\mathrm{LG}_0^2\mathbf{e}_x = -\mathrm{i}kf^3\mathrm{e}^{-\mathrm{i}kf}\frac{4E_0}{w_0^2}\sqrt{\frac{n_1}{n_2}}\frac{1}{2}\int_0^{\theta_{\max}} f_w(\theta)\sin^3\theta\cos^{1/2}\theta\mathrm{d}\theta\times \begin{pmatrix} -(1+\cos\theta)J_2(k\rho\sin\theta)e^{2i\varphi} - (1-\cos\theta)\frac{1}{2}J_4(k\rho\sin\theta)e^{4i\varphi} - (1-\cos\theta)\frac{1}{2}J_0(k\rho\sin\theta) \\ (1-\cos\theta)\frac{1}{2}\mathrm{i}J_4(k\rho\sin\theta)e^{4i\varphi} - (1-\cos\theta)\frac{1}{2}\mathrm{i}J_0(k\rho\sin\theta) \\ -\mathrm{i}\sin\theta\left[J_1(k\rho\sin\theta)e^{i\varphi} - J_3(k\rho\sin\theta)e^{3i\varphi}\right] \end{pmatrix}, \tag{6.22}$$

$$\mathrm{LG}_0^2\mathbf{e}_y = -\mathrm{i}kf^3\mathrm{e}^{-\mathrm{i}kf}\frac{4E_0}{w_0^2}\sqrt{\frac{n_1}{n_2}}\frac{1}{2}\int_0^{\theta_{\max}} f_w(\theta)\sin^3\theta\cos^{1/2}\theta\mathrm{d}\theta\times \begin{pmatrix} (1-\cos\theta)\frac{1}{2}\mathrm{i}J_4(k\rho\sin\theta)e^{4i\varphi} - (1-\cos\theta)\frac{1}{2}\mathrm{i}J_0(k\rho\sin\theta) \\ c-(1+\cos\theta)J_2(k\rho\sin\theta)e^{2i\varphi} + (1-\cos\theta)\frac{1}{2}J_4(k\rho\sin\theta)e^{4i\varphi} + (1-\cos\theta)\frac{1}{2}J_0(k\rho\sin\theta) \\ \sin\theta\left[J_1(k\rho\sin\theta)e^{i\varphi} + J_3(k\rho\sin\theta)e^{3i\varphi}\right] \end{pmatrix}. \tag{6.23}$$

Before we write out the coefficient matrix, we can perform the dϕ integral to simplify the expression. We define a few integral abbreviations in the similar fashion as in chapter 3, to which we define 3 indices: the first index indicates whether the term inside the integral is $(1+\cos\theta)$, $(1-\cos\theta)$, or just 1, and it takes the value of 1, 0, 3, respectively. The second index is the order number of $\sin\theta$. The third index is the order of the (first kind) Bessel functions. We write out the integral abbreviations we are going to use explicitly:

$$\begin{aligned} I_{132} &= \int_0^{\theta_{\max}} f_w(\theta)(\cos\theta)^{1/2}\sin^3\theta(1+\cos\theta)J_2(k\rho\sin\theta)\mathrm{e}^{\mathrm{i}kz\cos\theta}\mathrm{d}\theta, \\ I_{030} &= \int_0^{\theta_{\max}} f_w(\theta)(\cos\theta)^{1/2}\sin^3\theta(1-\cos\theta)J_0(k\rho\sin\theta)\mathrm{e}^{\mathrm{i}kz\cos\theta}\mathrm{d}\theta, \\ I_{341} &= \int_0^{\theta_{\max}} f_w(\theta)(\cos\theta)^{1/2}\sin^4\theta J_1(k\rho\sin\theta)\mathrm{e}^{\mathrm{i}kz\cos\theta}\mathrm{d}\theta. \end{aligned} \tag{6.24}$$

Some other integral abbreviations appear in the following calculation were given in chapter 3 in Eq. (3.18). We will not write them out explicitly as they would cancel each other out eventually. With these we are able to calculate our coefficient matrix as

$$\mathrm{LG}_0^2 = -\mathrm{i}kf^3\mathrm{e}^{-\mathrm{i}kf}\frac{2E_0}{w_0^2}\sqrt{\frac{n_1}{n_2}} \begin{bmatrix} -I_{132}e^{2i\varphi} - \frac{1}{2}I_{034}e^{4i\varphi} - \frac{1}{2}I_{030} & \frac{1}{2}\mathrm{i}I_{034}e^{4i\varphi} - \frac{1}{2}I_{030} \\ \frac{1}{2}\mathrm{i}I_{034}e^{4i\varphi} - \frac{1}{2}\mathrm{i}I_{030} & -I_{132}e^{2i\varphi} + \frac{1}{2}I_{034}e^{2i\varphi} + \frac{1}{2}I_{030} \\ -\mathrm{i}I_{341}e^{i\varphi} + \mathrm{i}I_{343}e^{3i\varphi} & I_{341}e^{i\varphi} + I_{343}e^{3i\varphi} \end{bmatrix}, \tag{6.25}$$

hence we get $\mathrm{LG}_0^2\mathbf{e}_R$ from Eq. (6.25) as

$$\mathrm{LG}_0^2\mathbf{e}_R = 2kf^3\mathrm{e}^{-\mathrm{i}kf}\frac{E_0}{w_0^2}\sqrt{\frac{n_1}{n_2}}\begin{pmatrix} \mathrm{i}I_{132}e^{2i\varphi}+\mathrm{i}I_{030} \\ I_{132}e^{2i\varphi}-\mathrm{I}_{030} \\ -2I_{341}e^{i\varphi} \end{pmatrix}. \tag{6.26}$$

From previous results we have the coefficient matrix for LG_0^0 as

$$\mathrm{LG}_0^0 = -\frac{\mathrm{i}kf}{2}\sqrt{\frac{n_1}{n_2}}E_0\mathrm{e}^{-\mathrm{i}kf}\begin{bmatrix} I_{110}+I_{012}\cos(2\varphi) & I_{012}\sin(2\varphi) \\ I_{012}\sin(2\varphi) & I_{110}-I_{012}\cos(2\varphi) \\ -2iI_{321}\cos\varphi & -2iI_{321}\sin\varphi \end{bmatrix}, \tag{6.27}$$

hence we have

$$\begin{aligned}\mathrm{LG}_0^0\mathbf{e}_L &= -\frac{\mathrm{i}kf}{2}\sqrt{\frac{n_1}{n_2}}E_0\mathrm{e}^{-\mathrm{i}kf}\begin{bmatrix} I_{110}+I_{012}\cos(2\varphi) & I_{012}\sin(2\varphi) \\ I_{012}\sin(2\varphi) & I_{110}-I_{012}\cos(2\varphi) \\ -2iI_{321}\cos\varphi & -2iI_{321}\sin\varphi \end{bmatrix}\begin{bmatrix} 1 \\ i \end{bmatrix} \\ &= -\frac{\mathrm{i}kf}{2}\sqrt{\frac{n_1}{n_2}}E_0\mathrm{e}^{-\mathrm{i}kf}\begin{bmatrix} I_{110}+I_{012}\cos(2\varphi)+iI_{012}\sin(2\varphi) \\ I_{012}\sin(2\varphi)+i\left(I_{110}-I_{012}\cos(2\varphi)\right) \\ -2iI_{321}\cos\varphi+2I_{321}\sin\varphi \end{bmatrix}.\end{aligned} \tag{6.28}$$

We can construct the strongly focused n=2 skyrmion by adding Eq. (6.26) and Eq. (6.28). Once we have the expression for the n=2 skyrmion field, calculating the spin direction vector at each point becomes straightforward. Using Mathematica simulations, we get the point distribution on the spin direction sphere, as shown in Figure 6.8.

The Poincarana sphere, however, is a bit trickier to get. First, we need to determine the handedness of a certain field point, which will tell us whether it corresponds to the plus or minus case. We then apply the appropriate rotational matrix for that point, as described in subsection 6.4.1. Since both the Poincaré sphere and the Poincarana sphere are suitable for describing the polarization distribution, we plot both of them, as shown in Figure 6.9.

In this figure, we can see the polarization distribution after the skyrmion field has been focused. There are more right-handed polarizations than left-handed ones, and the symmetry of the field is preserved. Additionally, we clearly observe the corresponding relations between the parameters in the two spheres, as discussed in subsection 6.4.2: the height of the representation points on both spheres is the same, and the polar angle ϕ in the Poincaré sphere is twice of the polar angle in the Poincarana sphere.

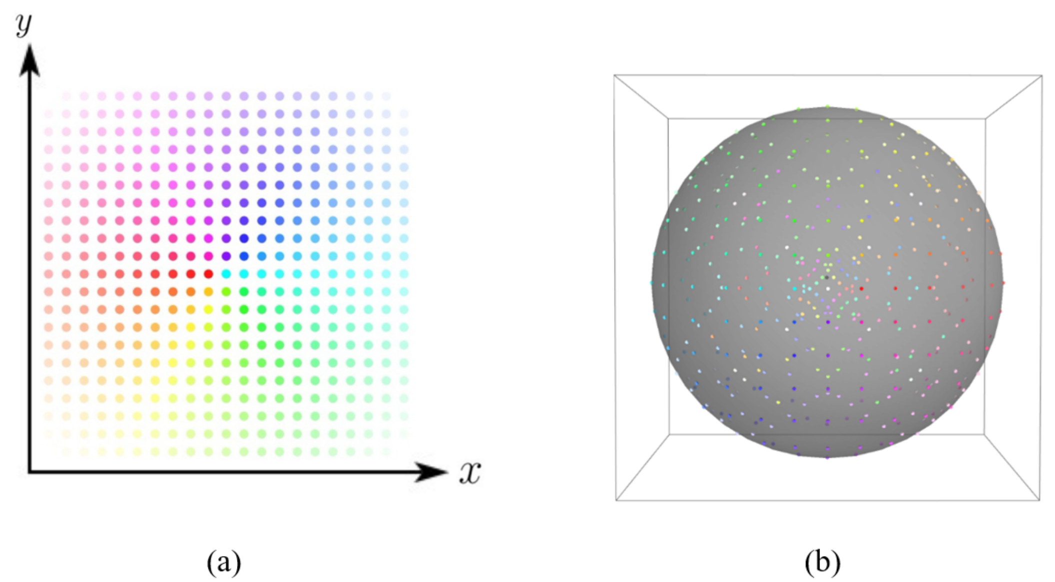

Figure 6.8: Spin direction sphere simulated for the strongly focused $n = 2$ skyrmion beam. (a) The colourmap used for the focal plane, where each position in the focal plane is denoted by a distinct colour. (b) The spin direction sphere, where the dots on the sphere record the polarization direction of corresponding points in the focal plane. Note that the white dot (on the centre of the front) represents z-direction, while the black dot (on the centre of the back) represents $-z$-direction.

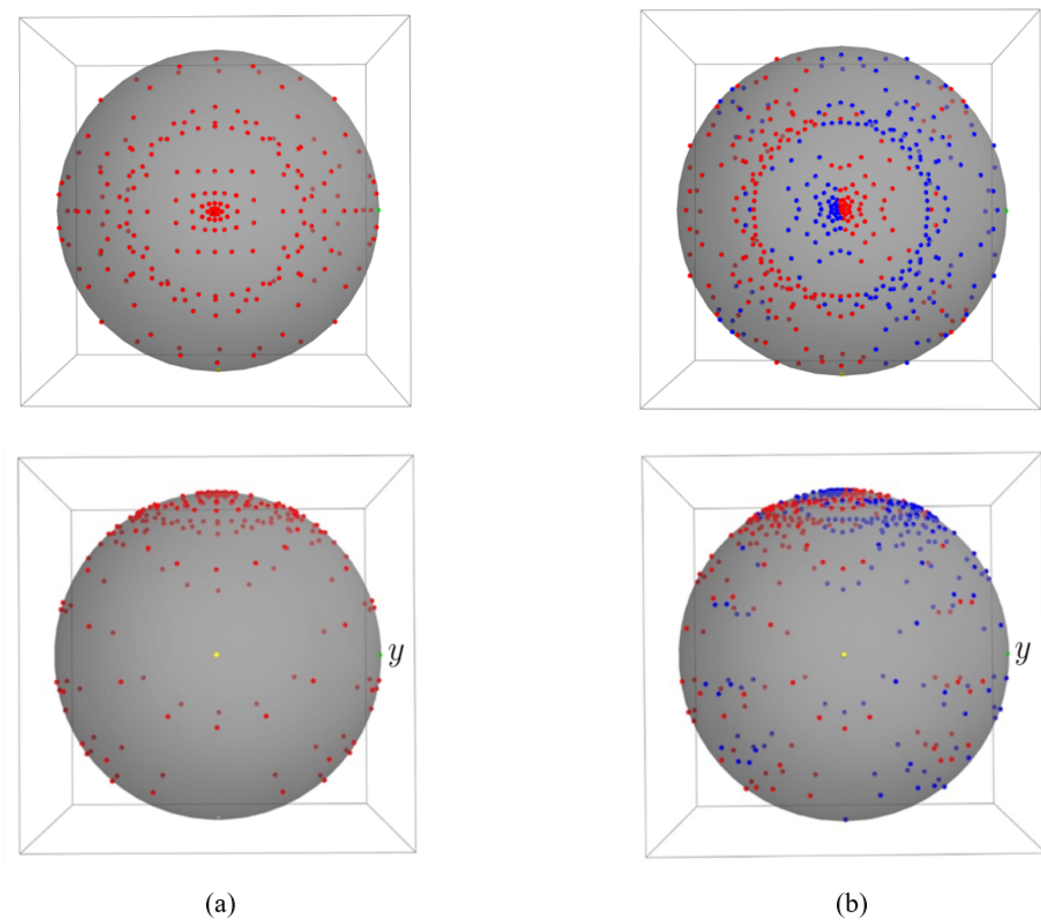

Figure 6.9: A plot of the Poincaré sphere (a) and the Poincarana sphere (b), where the blue and red dots on the Poincarana sphere correspond to the left and right foci of the polarization ellipses projected onto the sphere. The top row shows the top view of the two spheres, clearly illustrating that the symmetry of the field is preserved after focusing. The bottom row presents the side views, where the yellow dot represents the x-direction, and the green dot represents the y-direction.

6.6 Conclusion

In this chapter, we introduced a novel approach to describing the polarization distribution of a general 3D field. We first highlighted the challenges of representing 3D polarization distributions with existing models, then briefly introduced the Majorana/Poincarana representation and compared it with the familiar Poincaré sphere representation. We pointed out the equivalence and links between the two constructions, as well as the key differences between them. Each of these representations has its advantages and limitations.

We then explained the general concept of our two-sphere method and outlined the algorithm. We concluded with the specific case of a focused $n = 2$ skyrmion beam. We used the Richards-Wolf method to derive the expression for the strongly focused beam and demonstrated how our two-sphere method can be employed to describe the polarization distribution. The spherical symmetry observed in the simulation results validated the approach. Additionally, we compared our results with those in [106], where a complex field method was used to calculate a strongly focused $n = 2$ skyrmion. Through careful parameter design, they achieved a Bloch C-skyrmion.

Finally, we compared the Poincaré sphere representation with the Poincarana sphere representation for this example, which clearly illustrated the relationships between the two representations.

Chapter 7

Summary and conclusions

In this thesis, we investigated various topics related to structured light, with a focus on the strong focusing of light, which exhibits new properties that do not exist in the paraxial case. We also concentrated on one particular type of beam with topological properties: the skyrmion beams. We presented the paraxial skyrmion model, which exists in a magnetic field, and introduced the transition of this concept to paraxial optics. Based on this, we identified a topological method for calculating the skyrmion numbers. Additionally, we developed a generalization of the concept of skyrmions, both geometrically and mathematically. We then studied a strongly focused skyrmion using the two-sphere method we developed.

In chapter 2, we introduced the background theory of structured light and the strong focusing system. We discussed the concept of structured light, which can be described in terms of its amplitude, phase, and polarization. We introduced the concept of paraxial beams, including their angular spectrum representation, as well as the fundamental and higher-order modes. The concept of Gouy phase is emphasized, and the concept of polarization is highlighted, including various ways of describing this property.

We then introduced the strong focusing system, based on the Richards-Wolf model, which is used for theoretical calculations throughout this thesis. We explained the approximations made in this model and the geometrical relations it employs.

In chapter 3, we investigated the Faraday effect for both paraxial and strongly focused radially polarized beams. We explained our motivation for transitioning from the paraxial case to the strongly focused case and provided calculation details for the strongly focused radially polarized field. Our findings indicate that, for structured light, the magneto-optical interaction reveals a more intricate pattern termed a secondary Faraday effect, stemming from similar mechanism. This secondary effect is amplified in strong focusing systems, making it comparable to the linear Faraday effect. The simulation results are presented alongside some preliminary experimental results, which verified our theoretical predictions. We also outlined a possible future direction for the problem: a complete theoretical study of the Voigt effect and the Faraday effect as a whole for oblique incidence. We present our solution for the eigenmodes of this problem.

In chapter 4 We introduced skyrmion beams, a class of structured light beams with topological features which triggers considerable research interest. Skyrmionic structures can be found in paraxial light beams with a continuously varying polarization distribution and can be characterized by the skyrmion number. In addition to the existing methods of calculating skyrmion numbers, we proposed a new topological approach for calculating skyrmion numbers. We also introduced the concept of skyrmion field lines, which are lines of constant polarization.

In chapter 5, we proposed the concept of consistent and mixed-up base measurements and explained both geometrically and mathematically how this can be understood. We proved that a skyrmion field remains unchanged under mixed-up base measurements. We demonstrated the topological equivalence between skyrmions and bimerons, as well as numerous other topological equivalents, by generalizing the parameters. We pointed out that the definition of singularities can be generalized with respect to the projections we made. We demonstrated experimentally that the new topological method provides significantly improved measurements of the skyrmion number, and the flexibility of using mixed-up base measurements allows even better results due to the avoidance of the low-intensity area. Additionally, the measurement is stable against increasing noise ratios.

In chapter 6, we introduced the concept of the Majorana sphere, a representation of spinors applied to optics by Hannay, as a tool to describe 3D polarized beams. The Majorana sphere was later modified into the Poincaré sphere, which combines the features of both the Majorana sphere and the Poincaré sphere. We pointed out the connections and equivalence between the Poincaré and Majorana representations and proposed a two-sphere method to comprehensively describe general 3D polarization fields. We illustrated the concept with an $n = 2$ paraxial skyrmion, focused by the Richards-Wolf system. There are future works that can be done on this topic, such as the proper definition of the skyrmion number after focusing to characterize the non-paraxial field, which may be linked to the overall coverage of both spheres. Additionally, a potential generalization of the skyrmion field lines to higher dimensions is possible.

Bibliography

[1] I. al-Haytham, *The Optics of Ibn Al-Haytham: Books I-III: On Direct Vision*. London: The Warburg Institute, 1990. Translated and with commentary by A. I. Sabra.

[2] I. Newton, *Opticks: Or, A Treatise of the Reflections, Refractions, Inflections and Colours of Light*. Dover Publications, 1704.

[3] E. Hecht, *Optics*. Pearson Education, 5th ed., 2017.

[4] A. Forbes, M. de Oliveira, and M. R. Dennis, "Structured light," *Nature Photonics*, vol. 15, p. 253–262, Apr 2021.

[5] B. Kahr and K. Claborn, "The lives of malus and his bicentennial law," *ChemPhysChem*, vol. 9, pp. 43–58, 2008.

[6] M. Born, E. Wolf, and A. B. Bhatia, *Principles of Optics*. Cambridge University Press, 2019.

[7] H. Rubinsztein-Dunlop, A. Forbes, *et al.*, "Roadmap on structured light," *Journal of Optics*, vol. 19, p. 013001, 2016.

[8] G. Lazarev, A. Hermerschmidt, S. Krüger, and S. Osten, *LCOS Spatial Light Modulators: Trends and Applications*. Wiley, 2012.

[9] Y.-X. Ren, M. Li, H. Kun, *et al.*, "Experimental generation of Laguerre-Gaussian beam using digital micromirror device," *Applied Optics*, vol. 49, p. 1838, 2016.

[10] L. Allen, M. W. Beijersbergen, R. J. C. Spreeuw, and J. P. Woerdman, "Orbital angular momentum of light and the transformation of laguerre-gaussian laser modes," *Phys. Rev. A*, vol. 45, pp. 8185–8189, Jun 1992.

[11] J. Wang and Y. Liang, "Generation and detection of structured light: A review," *Frontiers in Physics*, vol. 9, p. 688284, May 2021.

[12] L. Zhu, A. Wang, and J. Wang, "Free-space data-carrying bendable light communications," *Scientific Reports*, vol. 9, p. 14969, Oct 2019.

[13] J. Liu, I. Nape, Q. Wang, A. Vallés, J. Wang, and A. Forbes, "Multi-dimensional entanglement transport through single-mode fiber," *Science Advances*, vol. 6, p. eaay0837, Jan 2020.

[14] Y. Kozawa, D. Matsunaga, and S. Sato, "Superresolution imaging via super-oscillation focusing of a radially polarized beam," *Optica*, vol. 5, p. 86–86, Jan 2018.

[15] R. Bingham, J. T. Mendonça, and P. K. Shukla, "Plasma based charged-particle accelerators," *Plasma Physics and Controlled Fusion*, vol. 46, p. R1–R23, Nov 2003.

[16] L. Malmqvist and H. M. Hertz, "Second-harmonic generation in optically trapped nonlinear particles with pulsed lasers," *Applied optics*, vol. 34, p. 3392–3392, Jun 1995.

[17] F. Théberge, W. Liu, P. T. Simard, A. Becker, and S. L. Chin, "Plasma density inside a femtosecond laser filament in air: Strong dependence on external focusing," *Physical Review E*, vol. 74, p. 036406, Sep 2006.

[18] M. Faraday, "Experimental researches in electricity.," *Proceedings of the Royal Society of London*, vol. 3, p. 91–93, Jan 1830.

[19] N. Nersessian, *Faraday to Einstein: Constructing Meaning in Scientific Theories.* Springer Science & Business Media, Dec 2012.

[20] T. Skyrme, "A non-linear field theory," *Proceedings of the Royal Society of London. Series A. Mathematical and Physical Sciences*, vol. 260, p. 127–138, Feb 1961.

[21] A. Fert, N. Reyren, and V. Cros, "Magnetic skyrmions: advances in physics and potential applications," *Nature Reviews Materials*, vol. 2, p. 17031, Jun 2017.

[22] S. Gao, F. C. Speirits, F. Castellucci, S. Franke-Arnold, S. M. Barnett, and J. B. Götte, "Paraxial skyrmionic beams," *Physical review A*, vol. 102, p. 053513, Nov 2020.

[23] S. Tsesses, E. Ostrovsky, K. Cohen, B. Gjonaj, N. H. Lindner, and G. Bartal, "Optical skyrmion lattice in evanescent electromagnetic fields," *Science*, vol. 361, pp. 993–996, Sept. 2018.

[24] R. Aitchison, "Tony Skyrme and the origins of skyrmions," *arXiv (Cornell University)*, Dec 2019.

[25] P. Sutcliffe, "Skyrmions, instantons and holography," *Journal of High Energy Physics*, vol. 2010, no. 8, p. Article 019, 2010.

[26] U. Al Khawaja and H. Stoof, "Skyrmions in a ferromagnetic Bose–Einstein condensate," *Nature*, vol. 411, p. 918–920, 2001.

[27] C. D. Parmee, M. R. Dennis, and J. Ruostekoski, "Optical excitations of skyrmions, knotted solitons, and defects in atoms," *Communications Physics*, vol. 5, p. Article 54, 2022.

[28] M. Rho and I. Zahed, *The Multifaceted Skyrmion*. World Scientific, June 2015.

[29] A. N. Bogdanov and C. Panagopoulos, "Physical foundations and basic properties of magnetic skyrmions," *Nature Reviews Physics*, vol. 2, pp. 492–498, July 2020.

[30] Y. Tokura and N. Kanazawa, "Magnetic skyrmion materials," *Chemical Reviews*, vol. 121, no. 5, pp. 2857–2897, 2021. PMID: 33164494.

[31] C. B. et al., "The 2020 skyrmionics roadmap," *Journal of Physics D: Applied Physics*, vol. 53, no. 36, p. 363001, 2020.

[32] S. Donati, L. Dominici, G. Dagvadorj, D. Ballarini, M. D. Giorgi, A. Bramati, G. Gigli, Y. G. Rubo, M. H. Szymańska, and D. Sanvitto, "Twist of generalized skyrmions and spin vortices in a polariton superfluid," *Proceedings of the National Academy of Sciences*, vol. 113, pp. 14926–14931, Dec. 2016.

[33] L. Du, A. Yang, A. V. Zayats, and X. Yuan, "Deep-subwavelength features of photonic skyrmions in a confined electromagnetic field with orbital angular momentum," *Nature Physics*, vol. 15, p. 650–654, Apr 2019.

[34] S. Gao, *Skyrmionic beams and quantum matched filtering*. PhD thesis, University of Glasgow, 2021.

[35] N. Nagaosa and Y. Tokura, "Topological properties and dynamics of magnetic skyrmions," *Nature Nanotechnology*, vol. 8, no. 12, pp. 899–911, 2013.

[36] G. Finocchio, F. Büttner, R. Tomasello, M. Carpentieri, and M. Kläui, "Magnetic skyrmions: from fundamental to applications," *Journal of Physics D*, vol. 49, p. 423001–423001, Sep 2016.

[37] Z. Ye, S. M. Barnett, S. Franke-Arnold, J. B. Götte, A. McWilliam, F. C. Speirits, and C. M. Cisowski, "Theory of paraxial optical skyrmions," *Proceedings of the Royal Society A: Mathematical, Physical and Engineering Sciences*, vol. 480, no. 2297, p. 20240109, 2024.

[38] M. A. Alonso, "Geometric descriptions for the polarization of nonparaxial light: a tutorial," *Adv. Opt. Photon.*, vol. 15, pp. 176–235, Mar 2023.

[39] L. Novotny and B. Hecht, *Principles of nano-optics.* Cambridge University Press, 2012.

[40] J. Mertz, *Introduction to Optical Microscopy.* Cambridge: Cambridge University Press, 2nd ed., 2019.

[41] B. Richards and E. Wolf, "Electromagnetic diffraction in optical systems. II. structure of the image field in an aplanatic system," *Proc. R. Soc. Lond. A*, vol. 253, pp. 358–79, 1959.

[42] G. Sarton, *Ancient Science Through the Golden Age of Greece.* New York : Norton, 1993.

[43] O. V. Angelsky, A. Y. Bekshaev, S. G. Hanson, C. Y. Zenkova, I. I. Mokhun, and J. Zheng, "Structured light: Ideas and concepts," *Frontiers in Physics*, vol. 8, p. 114, 2020.

[44] A. Ashkin, "Optical trapping and manipulation of neutral particles using lasers," *Proceedings of the National Academy of Sciences of the United States of America*, vol. 94, no. 10, pp. 4853–4860, 1997.

[45] O. V. Angelsky, S. G. Hanson, C. Y. Zenkova, M. P. Gorsky, and N. V. Gorodyns'ka, "On polarization metrology (estimation) of the degree of coherence of optical waves," *Optics Express*, vol. 17, no. 19, pp. 15623–15634, 2009.

[46] Y. Xu, J. Sun, W. Walasik, and N. M. Litchinitser, "Probing metamaterials with structured light," *Opt. Express*, vol. 24, pp. 26249–26254, Nov 2016.

[47] D. H. Goldstein, *Polarized light.* CRC Press, 2016.

[48] R. Grella, "Fresnel propagation and diffraction and paraxial wave equation," *Journal of Optics*, vol. 13, p. 367–374, 1982.

[49] A. E. Siegman, *Lasers.* University Science Books, 1986.

[50] H. Crew, C. Huygens, T. Young, A. J. Fresnel, and F. Arago, *The Wave Theory of Light: Memoirs by Huygens, Young and Fresnel.* New York, Cincinnati: American Book Company, 1900.

[51] L. Andrews and R. Phillips, *Laser Beam Propagation Through Random Media*, ch. 4. Scopus Export, 09 2005.

[52] J. W. Goodman, *Introduction to fourier optics.* McGraw-Hill, 1968.

[53] E. J. Galvez, "Gaussian beams in the optics course," *American Journal of Physics*, vol. 74, p. 355–361, 2006.

[54] E. Zauderer, "Complex argument Hermite–Gaussian and Laguerre–Gaussian beams," *Journal of the Optical Society of America A*, vol. 3, p. 465, 1986.

[55] C. Cisowski, J. B. Götte, and S. Franke-Arnold, "Colloquium: Geometric phases of light: Insights from fiber bundle theory," *Rev. Mod. Phys.*, vol. 94, p. 031001, Jul 2022.

[56] G. Nienhuis and L. Allen, "Paraxial wave optics and harmonic oscillators," *Phys. Rev. A*, vol. 48, pp. 656–665, Jul 1993.

[57] G. H. dos Santos, D. C. Salles, M. G. Damaceno, B. T. Menezes, C. Corso, M. Martinelli, P. H. S. Ribeiro, and R. M. de Araújo, "Decomposing spatial mode superpositions with a triangular optical cavity," *Phys. Rev. Appl.*, vol. 16, p. 034008, Sep 2021.

[58] C. Liu, "Vortex beam and its application in optical tweezers," *Journal of Physics: Conference Series*, vol. 1549, p. 032012, 2020.

[59] D. Palacios, D. Rozas, and G. A. Swartzlander, "Observed scattering into a dark optical vortex core," *Phys. Rev. Lett.*, vol. 88, p. 103902, Feb 2002.

[60] J. F. Nye, *Natural focusing and fine structure of light: Caustics and wave dislocations.* Institute of Physics, 1999.

[61] W. N. Plick and M. Krenn, "Physical meaning of the radial index of laguerre-gauss beams," *Conference on Lasers and Electro-Optics*, 2017.

[62] E. Wolf and J. C. Dainty, *Progress in Optics.* Newnes, 1976.

[63] R. W. Boyd, "Intuitive explanation of the phase anomaly of focused light beams," *Journal of the Optical Society of America*, vol. 70, p. 877, July 1980.

[64] S. Feng and H. G. Winful, "Physical origin of the gouy phase shift," *Optics Letters*, vol. 26, p. 485, Apr 2001.

[65] J. D. Jackson, *Classical electrodynamics.* New York: J. Wiley, 1975.

[66] D. Singh, *Fundamentals of Optics.* PHI Learning Pvt. Ltd., 2nd ed., 2015.

[67] G. R. Fowles, *Introduction to Modern Optics.* Dover Books on Physics, Dover Publications, reprint ed., 1989. Dover classics of science and mathematics.

[68] E. Collett, *Field guide to polarization Edward Collett.* SPIE Press, 2012.

[69] D. S. Kliger, J. W. Lewis, and C. E. Randall, "Chapter 5 - the Jones calculus, Mueller calculus, and Poincaré sphere revisited," in *Polarized Light in Optics and Spectroscopy*, pp. 103–152, Boston: Academic Press, 1990.

[70] C. Gillispie, *Dictionary of scientific biography*, vol. 13. Charles Scribner's Sons, 1976.

[71] C. Brosseau, *Fundamentals of Polarized Light.* Wiley-Interscience, Oct 1998.

[72] E. Collett, *Field Guide to Polarization.* SPIE, 2005.

[73] R. C. Jones, "A new calculus for the treatment of optical systemsi description and discussion of the calculus," *Journal of the Optical Society of America*, vol. 31, p. 488, Jul 1941.

[74] W. H. McMaster, "Matrix representation of polarization," *Reviews of Modern Physics*, vol. 33, p. 8–28, Jan 1961.

[75] H. Poincaré, *Théorie mathématique de la lumière II.: Nouvelles études sur la diffraction. Théorie de la dispersion de Helmholtz. Leçons professées pendant le premier semestre 1891-1892.* Paris: G. Carré, 1892.

[76] S. Barnett, *Quantum Information.* Oxford Master Series in Physics, OUP Oxford, 2009.

[77] S. Kawata and V. M. Shalaev, eds., *Tip Enhancement.* Elsevier, 1st ed., 2006.

[78] M. Celebrano, P. Kukura, A. Renn, and V. Sandoghdar, "Single-molecule imaging by optical absorption," *Nature Photonics*, vol. 5, p. 95–98, Jan 2011.

[79] A. V. Kharitonov and S. S. Kharintsev, "Strong focusing higher-order laser modes: transverse and longitudinal optical fields," *Journal of Physics: Conference Series*, vol. 613, p. 012010, May 2015.

[80] R. Paschotta, "Near field and far field." RP Photonics Encyclopedia, 2019.

[81] L. Mandel and E. Wolf, *Optical coherence and quantum optics*. Cambridge University Press, 1995.

[82] A. Ashkin, J. M. Dziedzic, J. E. Bjorkholm, and S. Chu, "Observation of a single-beam gradient force optical trap for dielectric particles," *Optics Letters*, vol. 11, p. 288, May 1986.

[83] T. A. Nieminen, G. Knöner, N. R. Heckenberg, and H. Rubinsztein-Dunlop, "Physics of optical tweezers," in *Laser Manipulation of Cells and Tissues*, vol. 82 of *Methods in Cell Biology*, pp. 207–236, Academic Press, 2007.

[84] V. N. Mahajan, *Aberration Theory Made Simple, Second Edition*. SPIE ebooks, second ed., Aug 2011.

[85] T. Amemiya, A. Ishikawa, T. Kanazawa, *et al.*, "Permeability-controlled optical modulator with tri-gate metamaterial: control of permeability on inp-based photonic integration platform," *Scientific Reports*, vol. 5, p. 8985, 2015.

[86] J. Zak, E. R. Moog, C. Liu, and S. D. Bader, "Fundamental magneto-optics," *Journal of Applied Physics*, vol. 68, pp. 4203–4207, 10 1990.

[87] J. Zak, E. Moog, C. Liu, and S. Bader, "Universal approach to magneto-optics," *Journal of Magnetism and Magnetic Materials*, vol. 89, pp. 107–123, 1990.

[88] L. D. Barron, *Molecular Light Scattering and Optical Activity*. Cambridge: Cambridge University Press, 2nd ed., 2004.

[89] M. Freiser, "Magneto-optical effects," *IEEE Transactions on Magnetics*, vol. 4, pp. 152–161, 1968.

[90] N. O. Urs, B. Mozooni, P. Mazalski, M. Kustov, P. Hayes, S. Deldar, E. Quandt, and J. McCord, "Advanced magneto-optical microscopy: Imaging from picoseconds to centimeters - imaging spin waves and temperature distributions (invited)," *AIP Advances*, vol. 6, no. 5, p. 055605, 2016.

[91] M. E. Yousif, "The Faraday effect explained," *IOSR Journal of Applied Physics*, vol. 9, no. 5, pp. 74–84, 2017.

[92] P. N. Argyres, "Theory of the Faraday and Kerr effects in ferromagnetics," *Physical Review*, vol. 97, p. 334–345, Jan 1955.

[93] D. Budker, D. F. Kimball, S. M. Rochester, and V. V. Yashchuk, "Resonant nonlinear magneto-optical effects in atoms," *Reviews of Modern Physics*, vol. 74, no. 4, pp. 1153–1201, 2002.

[94] P. Yeh, *Optical Waves in Layered Media.* John Wiley & Sons, 2nd ed., 2005.

[95] C. Jooss and V. Born, "Determination of electric field distributions in superconductors via magneto-optical imaging and the Faraday law," *Phys. Rev. B*, vol. 73, p. 094508, 2006.

[96] S. S. Birla *et al.*, "Magneto-optical effects and their applications," *Journal of Applied Physics*, vol. 125, p. 120901, 2019.

[97] A. G. Ardakani and Z. Zare, "Strong Faraday rotation in a topological insulator single layer using dielectric multilayered structures," *J. Opt. Soc. Am. B*, vol. 38, pp. 2562–2569, 2021.

[98] J. Y. Chin, T. Steinle, T. Wehlus, D. Dregely, T. Weiss, V. I. Belotelov, B. Stritzker, and H. Giessen, "Nonreciprocal plasmonics enables giant enhancement of thin-film Faraday rotation," *Nature Communications*, vol. 4, p. 1599, 2013.

[99] P. Genevet, F. Capasso, F. Aieta, M. Khorasaninejad, and R. C. Devlin, "Recent advances in planar optics: from plasmonic to dielectric metasurfaces," *Optica*, vol. 4, pp. 139–152, 2017.

[100] K. S. Youngworth and T. G. Brown, "Focusing of high numerical aperture cylindrical-vector beams," *Optics Express*, vol. 7, p. 77, Jul 2000.

[101] Q. Zhan, "Cylindrical vector beams: from mathematical concepts to applications," *Adv. Opt. Photon.*, vol. 1, pp. 1–57, 2009.

[102] K. Y. Bliokh, F. J. Rodríguez-Fortuño, F. Nori, and A. V. Zayats, "Spin–orbit interactions of light," *Nature Photonics*, vol. 9, pp. 796–808, 2015.

[103] K. A. Forbes, D. Green, and G. A. Jones, "Relevance of longitudinal fields of paraxial optical vortices," *Journal of Optics*, vol. 23, p. 075401, May 2021.

[104] X. Pang and T. D. Visser, "Manifestation of the gouy phase in strongly focused, radially polarized beams," *Opt. Express*, vol. 21, pp. 8331–8341, 2013.

[105] S. Pelchat-Voyer and M. Piché, "Clarifications on the gouy phase of radially polarized laser beams," *J. Opt. Soc. Am. A*, vol. 37, pp. 1496–1504, 2020.

[106] R. Gutiérrez-Cuevas and E. Pisanty, "Optical Polarization Skyrmionic Fields in free space," *Journal of Optics*, vol. 23, p. 024004, 2021.

[107] T. Bauer, P. Banzer, E. Karimi, S. Orlov, A. Rubano, L. Marrucci, E. Santamato, R. W. Boyd, and G. Leuchs, "Observation of optical polarization möbius strips," *Science*, vol. 347, no. 6225, pp. 964–966, 2015.

[108] A. Yariv and P. Yeh, *Optical waves in crystals : propagation and control of laser radiation.* New York: Wiley, 2003.

[109] V. Aita, M. Shevchenko, F. J. Rodríguez-Fortuño, and A. V. Zayats, "Propagation of focused scalar and vector vortex beams in anisotropic media: A semianalytical approach," *Phys. Rev. B*, vol. 109, p. 125433, Mar 2024.

[110] S. L. Sondhi, A. Karlhede, S. A. Kivelson, and E. H. Rezayi, "Skyrmions and the crossover from the integer to fractional quantum Hall effect at small Zeeman energies," *Physical Review B*, vol. 47, p. 16419–16426, Jun 1993.

[111] I. Raičević, D. Popović, C. Panagopoulos, L. Benfatto, M. B. Silva Neto, E. S. Choi, and T. Sasagawa, "Skyrmions in a doped antiferromagnet," *Phys. Rev. Lett.*, vol. 106, p. 227206, Jun 2011.

[112] M. Finazzi, M. Savoini, A. R. Khorsand, A. Tsukamoto, A. Itoh, L. Duò, A. Kirilyuk, T. Rasing, and M. Ezawa, "Laser-induced magnetic nanostructures with tunable topological properties," *Phys. Rev. Lett.*, vol. 110, p. 177205, Apr 2013.

[113] W. Koshibae, Y. Kaneko, J. Iwasaki, M. Kawasaki, Y. Tokura, and N. Nagaosa, "Memory functions of magnetic skyrmions," *Japanese Journal of Applied Physics*, vol. 54, p. 053001, Apr 2015.

[114] D. Vollhardt, P. Wölfle, and R. B. Hallock, "The superfluid phases of helium 3," *Physics Today*, vol. 44, p. 60–61, Aug 1991.

[115] D. R. Tilley, *Superfluidity And Superconductivity.* Routledge, 2018.

[116] S. Seki, X. Z. Yu, S. Ishiwata, and Y. Tokura, "Observation of skyrmions in a multiferroic material," *Science*, vol. 336, p. 198–201, Apr 2012.

[117] Y. Ishikawa, K. Tajima, D. Bloch, and M. Roth, “Helical spin structure in manganese silicide mnsi,” *Solid State Communications*, vol. 19, p. 525–528, Jul 1976.

[118] I. Nape, K. Singh, A. Klug, W. Buono, C. Rosales-Guzman, A. McWilliam, S. Franke-Arnold, A. Kritzinger, P. Forbes, A. Dudley, and A. Forbes, “Revealing the invariance of vectorial structured light in complex media,” *Nature Photonics*, vol. 16, p. 538–546, Jun 2022.

[119] C. Rosales-Guzmán, B. Ndagano, and A. Forbes, “A review of complex vector light fields and their applications,” *Journal of Optics*, vol. 20, no. 12, p. 123001, 2018.

[120] A. McWilliam, C. M. Cisowski, Z. Ye, F. C. Speirits, J. B. Götte, S. M. Barnett, and S. Franke-Arnold, “Topological Approach of Characterizing Optical Skyrmions and Multi-skyrmions,” *Laser & Photonics Reviews*, vol. 17, p. 2200155, 2023.

[121] N. D. Mermin and T.-L. Ho, “Circulation and Angular Momentum in the A Phase of Superfluid Helium-3,” *Physical Review Letters*, vol. 36, pp. 594–597, 1976.

[122] S. M. Barnett, F. Speirits, and J. Goette, “On lines of constant polarisation in structured light beams,” *Europhysics letters*, vol. 143, p. 35002–35002, Jul 2023.

[123] J. F. Nye, “Lines of circular polarization in electromagnetic wave fields,” *Proceedings of the Royal Society of London. Series A, Mathematical and physical sciences*, vol. 389, p. 279–290, Oct 1983.

[124] M. V. Berry and M. R. Dennis, “Polarization singularities in isotropic random vector waves,” *Royal Society*, vol. 457, p. 141–155, Jan 2001.

[125] Y. Shen, “Topological bimeronic beams,” *Optics Letters*, vol. 46, pp. 3737–3740, 2021.

[126] M. J. Padgett and J. Schroers, Courtial, “Poincaré-sphere equivalent for light beams containing orbital angular momentum,” *Optics Letters*, vol. 24, no. 7, 1999.

[127] C. Cisowski, P. Mazalski, Y. Shen, O. D. Oe, T. Franke-Arnold, and S. M. Barnett, “Building paraxial optical skyrmions using rational maps,” *Advanced Photonics Research*, vol. 2022, no. 350, 2023.

[128] Z. Ye, J. B. Götte, and C. M. Cisowski, "An atlas of optical skyrmions: charting topologically equivalent field configurations," *Journal of Optics*, vol. 27, p. 042502, 2025.

[129] C. J. Houghton, N. S. Manton, and P. M. Sutcliffe, "Rational maps, monopoles and skyrmions," *Nuclear Physics B*, vol. 510, pp. 507–537, Jan. 1998.

[130] R. A. Battye and P. M. Sutcliffe, "Skyrmions, fullerenes and rational maps," *Reviews in Mathematical Physics*, vol. 14, pp. 29–85, Jan. 2002.

[131] P. J. Ackerman, T. Boyle, and I. I. Smalyukh, "Squirming motion of baby skyrmions in nematic fluids," *Nature Communications*, vol. 8, no. 673, 2017. https://doi.org/10.1038/s41467-017-00673-z.

[132] T. Weidig, "The baby skyrme models and their multi-skyrmions," *Nonlinearity*, vol. 12, no. 6, p. 1489, 1999. https://doi.org/10.1088/0951-7715/12/6/303.

[133] P. A. M. Dirac, "Quantised singularities in the electromagnetic field,," *Proceedings of the Royal Society of London. Series A, Containing Papers of a Mathematical and Physical Character*, vol. 133, no. 821, pp. 60–72, 1931.

[134] Y. Shen, E. C. Martínez, and C. Rosales-Guzmán, "Generation of optical skyrmions with tunable topological textures," *ACS Photonics*, vol. 9, p. 296–303, Jan. 2022.

[135] R. Simon and N. Mukunda, "Minimal three-component SU(2) gadget for polarization optics," *Physics Letters A*, vol. 143, no. 4, pp. 165–169, 1990.

[136] S. Gao, F. C. Speirits, F. Castellucci, S. Franke-Arnold, S. M. Barnett, and J. B. Götte, "Paraxial skyrmionic beams," *Phys. Rev. A*, vol. 102, p. 053513, Nov 2020.

[137] J. Hannay, "The Majorana representation of polarization, and the berry phase of light," *Journal of Modern Optics*, vol. 45, p. 1001–1008, 1998.

[138] K. Y. Bliokh, M. A. Alonso, and M. R. Dennis, "Geometric phases in 2D and 3D polarized fields: geometrical, dynamical, and topological aspects," *Reports on Progress in Physics*, vol. 82, no. 12, p. 122401, 2019.

[139] S. Shabbir, *Majorana Representation in Quantum Optics*. PhD thesis, KTH Royal Institute of Technology, Stockholm, Sweden, 2017.

[140] J. Fu, J. Knolle, and N. B. Perkins, "Three types of representation of spin in terms of majorana fermions and an alternative solution of the kitaev honeycomb model," *Phys. Rev. B*, vol. 97, p. 115142, Mar 2018.

[141] N. Sūgakkai, *Encyclopedic Dictionary of Mathematics, Vol. 1.* MIT Press, illustrated, reprint ed., 1993.

[142] S. Kumar Pal, Ruchi, and P. Senthilkumaran, "C-point and v-point singularity lattice formation and index sign conversion methods," *Optics Communications*, vol. 393, pp. 156–168, 2017.

[143] M. V. Berry, "Paraxial beams of spinning light," in *Proceedings of SPIE, International Conference on Singular Optics*, vol. 3487, pp. 12–22, 1998.